論文 / 著書情報
Article / Book Information

題目(和文)	
Title(English)	Study of carrier behavior in organic-inorganic hybrid perovskite thin Films by using spectroscopic measurements
著者(和文)	Lei Lei Yin Win
Author(English)	Lei Lei Yin Win
出典(和文)	学位:博士(工学), 学位授与機関:東京工業大学, 報告番号:甲第11342号, 授与年月日:2019年12月31日, 学位の種別:課程博士, 審査員:間中 孝彰,中川 茂樹,山田 明,宮島 晋介,飯野 裕明,Shyam Sudhir Pandey
Citation(English)	Degree:Doctor (Engineering), Conferring organization: Tokyo Institute of Technology, Report number:甲第11342号, Conferred date:2019/12/31, Degree Type:Course doctor, Examiner:,,,,,
学位種別(和文)	博士論文
Type(English)	Doctoral Thesis

Study of Carrier Behavior in Organic-Inorganic Hybrid Perovskite Thin Films by Using Spectroscopic Measurements

Department of Electrical and Electronic Engineering

Lei Lei Yin Win

Study of Carrier Behavior in Organic-Inorganic Hybrid Perovskite Thin Films by Using Spectroscopic Measurements

A Doctoral Dissertation Presented by

Lei Lei Yin Win

Supervisor: Prof. Takaaki Manaka

Department of Electrical and Electronic Engineering,

School of Engineering,

Tokyo Institute of Technology

November, 2019

Preface

Organic-inorganic hybrid perovskites are increasing technological interest not only for photovoltaic applications but also for optoelectronic devices. Despite the considerable improvement in the power conversion efficiency, the investigation of its fundamental transport properties and the dominant factors of unclear behaviors such as hysteresis and ion migration, so on are still questionable. Visualization of the fundamental transport properties may lead to answers to these questions, which motivate us to do this research. Here, I studied the transport characteristics by direct observation of carrier motion base on spectroscopic measurements. I found that the correlation between the time of flight and transient photoluminescence (PL) imaging offers direct evidence of transport mechanisms such as hole transport phenomena and migration of intrinsic ions. Moreover, directly probed by the time-resolved microscopic optical second-harmonic generation (TRM-SHG) technique, we successfully detected the transient electric field migration. Then, the carrier mobility and trapped charge density can be quantitatively estimated based on the transient electric field distribution along the channel. I believe that direct observation of carrier transport from the electrode would be essential for further understanding of the carrier behavior in perovskite devices.

Table of Contents

Preface

Chapter 1 Overview

Chapter 2 Experimental methods and theoretical background

Chapter 3 Carrier behavior in hybrid organic inorganic perovskite materials ($CH_3NH_3PbI_3$) for electrical measurement

Chapter 4 Direct observation of carrier transport by photoluminescence imaging

Chapter 5 Carrier visualization of organic-inorganic hybrid perovskite thin films by using time-resolved microscopic second-harmonic generation (TRM-SHG)

Chapter 6 General Conclusion and Prospects

Acknowledgements

List of Publications and Conference Presentations

Chapter 1

Overview

1.1 Introduction

Nowadays, the world's energy consumption from exhaustive fossil fuels is about 85 %, and it makes concern on health and natural environment and global energy demand will also be two times by 2050 [1]. Facing with the world's increasing consumption of energy and environmental crisis in have driven the rapid development of sustainable energy. Among those, solar energy has attracted increasingly more attention from all countries due to its abundance, low cost, and environmental friendliness [2, 3].

Photovoltaic solar cells can directly convert the energy of sunlight into electrical energy based on the photovoltaic and thus, it has been counted as a very bright energy generation source. There are two different types of solar cell technologies, including traditional photovoltaic solar cells and emerging photovoltaic solar cells. The first group contain the most studied and popular photovoltaic materials such as crystalline silicon, amorphous silicon, post silicon solar cells groups (CdTe, CIGS, CuGaSe) and these technologies are completely developed and successfully commercialized but there is little room for high energy process, further improvement and high cost [4-6].

Thus why the low-cost simple fabrication process, flexible solar cells groups are emerging, and they are called emerging photovoltaic solar cells. That means technologies, which are still undergoing research to reach commercialization and including organic solar cells, quantum dots solar cells, dye-sensitized solar cells and most recently perovskite solar cells [7]. Among those, perovskite solar cells (PSCs) have risen as the hottest next-generation photovoltaic technology in one decade and are predicted to be one of the most serious challengers for the silicon-based solar cell market.

As the perovskite-based solar cell technology becomes more and more developing, the power conversion efficiency has increased rapidly, from 3.8% in 2009 to 25.2% in 2019 [8-10]. The rapid development in efficiency of perovskite solar cells has been gained by continuous improvement in device structure and architecture, fabrication methods and trying of mixed halide perovskite for enhanced electrical properties [9-12].

Despite the rapid developments of the efficiencies of perovskite photovoltaic solar cells, there are still remain in understanding the unclear carrier behaviors such as significant current voltage hysteresis [13], dominant of ion migration [14], trapping and detrapping effects [15], and ferroelectric behavior [16] etc. Some of those unclear behaviors can be addressed based on the fundamental transport properties such as carrier injection, carrier transport, and the nature of photogenerated species. In this sense, the target of intense research is to investigate the fundamental transport properties of the organic-inorganic hybrid perovskites by using spectroscopic methods. Direct observation of carrier transport from the electrode would be essential for further understanding of the carrier behavior in perovskite devices [17-19].

Even though perovskite materials is popular in photovoltaic community, the device structure for this study should be taken into field-effect transistor (FET) structure because we can clearly see the transport properties from the top of the FET structure between two electrode rather than solar cell structure. Moreover, FET structure provide a flexible platform to study the carrier transport mechanism of semiconductor devices.

This chapter will briefly introduce an overview of perovskites within the field of photovoltaics, the literature on history, and development of perovskite materials. Then several observations from the fundamental knowledge of these materials and their applications beyond photovoltaics reported by researchers are discussed, as well as some challenges. Finally, the motivation for this research and the structure of the dissertation are proposed.

1.2 Perovskites

The name perovskite comes from the name of the Russian Mineralogist L. A. Perovski who was first discovered the calcium carbonate $CaTiO_3$, a common mineral in the 19th century. After his discovery, the definition of perovskite has changed into the materials that have ABX_3 molecular structure, where A is for cation, B is also for cation and X represents an anion. The monovalent organic cation A and divalent metal cation B occupies the corner position whereas halide counter ion X is at the face center of pseudocubic unit cell. The other alternative viewpoint for its structure is that it can be assumed as a corner linked BX_6 in an octahedral geometry with cation A at the interstitial position. Figure 1.1 depicts the crystal structure of the perovskite material. The chemical structure of perovskite used in perovskite solar cells is $CH_3NH_3PbX_3$ (X=Cl, Br, I or their mixture) [20]. The most widely researched photovoltaic perovskite is synthesized from a combination of methylammonium iodide (CH_3NH_3I) and lead iodide (PbI_2), which produces in methylammonium lead triiodide ($CH_3NH_3PbI_3$).

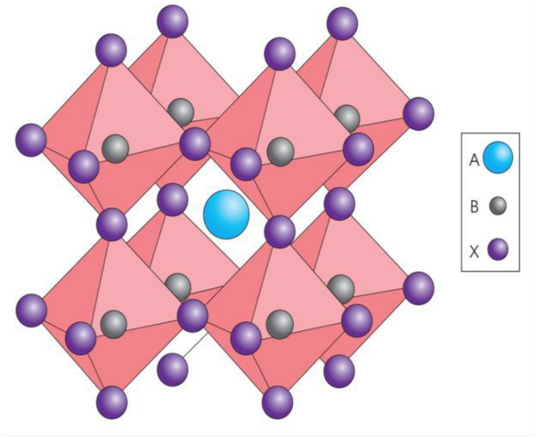

Figure 1.1: Crystal structure of basic perovskite ABX_3 [20].

1.3 History and development of perovskite solar cells

Even though the investigation of structural and physical properties of perovskite was first reported by Weber in 1978 [21, 22], German scientist David Mitzi firstly used organic-inorganic halide perovskite materials to research the optoelectronic properties [23]. Because of superior carrier mobility, initial research for the application of organic light-emitting diode (OLED) and thin film transistor (TFT) are focused for tin II based halide perovskite in 1990s. [24-26]

In 2009, Miyasaka's research team from Toin University of Yokohama applied $NH_3CH_3PbI_3$ and $CH_3NH_3PbBr_3$ as organic-inorganic visible light sensitizers on TiO_2 in a dye-sensitized solar cell and yielded power conversion efficiencies of 3.8% and 3.1% respectively [8]. However, at that time the perovskite has not been received much attention because of poor efficiency.

An improved efficiency of the lead-based hybrid perovskite sensitized PV cell was reported by Nam-Gyu Park et al. in 2011 as 6.5 % [27]. In 2012, Gratzel from

Swiss Federal Institute of Technology optimized the device parameter of dye sensitized solar cells to enhance the efficiency to 7.28 % [28].

In the same year, Snaith and his research team from University of Oxford implemented perovskite-based meso-superstructured solar cell (MSSC) (where Spiro-OMeTAD was used as hole transport material to replace the liquid ones to increased the stability of the device) and they demonstrated that the efficiencies of 10 % were achieved [9]. A rapid evolution development for both planer and mesostructured perovskite photovoltaic devices was emerged after 2013 as well as by improving the fabrication process [29, 30].

In 2013, Liu et al. further boosted the efficiency to 15.4 % via architecturing the planner solar cell by dual-source thermal evaporation method [31]. Since then, scientists have launched a series of battles using a range of novel deposition technique for higher PCE. In August 2014, Yang’s team optimized the energy level of each layer of the solar cells by using planer structure for suppressing the carrier recombination and increased the PCE to 19.3 % [32]. Then in order to achieve more stability, Seok and co-workers developed solvent engineering and carried out for higher efficiency by adding the compositional engineering method. After that, they incorporated $MAPbBr_3$ to $FaPbI_3$ to become stabilization of the phase of FAPbI3 and PCE of 20.1 % was reported [33-36].

In December 2015, the researchers from EPFL goaled a novel certified record PCE of 21 %. However, in 2016, the record was overwritten by the researchers from KRICT and UNIST as 22.1 % PCE. Improving the efficiency lead to 23.7% at 2018 and at 2018, June, Oxford photovoltaics’ perovskite silicon tandem solar cell has achieved 27% conversion efficiency and it exceed the efficiency of single junction silicon solar cell as illustrated in Fig 1.2. [9, 37-38]

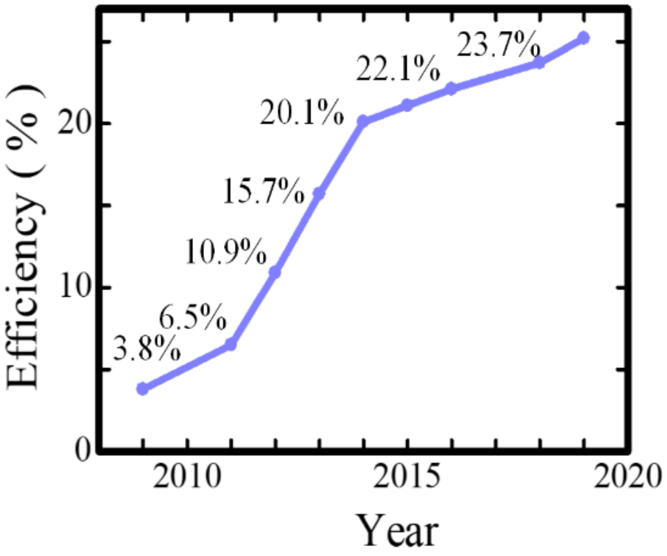

Figure 1.2: Rapid PCE evolution of perovskite solar cells from 2009 to 2019 [NREL Survey] [9]

However, the investigation of its fundamental transport properties and the dominant factors of unclear behaviors such as hysteresis and ion migration, so on are still questionable. Visualization of the fundamental transport properties may lead to answers to these questions which motivate us to do this research.

1.4 Fundamental characteristics of perovskite materials

Organometal halide perovskite ABX_3 possesses diversity in composition, structure, and properties. The structural probability and crystallographic stability can be determined by a Goldschmidt’s tolerance factor t, and it is defined as the ratio of the distance A-X to B-X in an idealized solid sphere model;

$$t = \frac{(R_A + R_X)}{\sqrt{2(R_B + R_X)}} \qquad (1.1)$$

Where R_A, R_B and R_X are the ionic radii of the corresponding ions. A tolerance factor of 1.0, indicates an ideal cubic perovskite crystal structure without lattice distortions [20]. However, if the values for the tolerance factor are between 0.89 and 1.0, perovskites can predominantly form as cubic crystal structure. If t less than 0.89, the less symmetric tetragonal or orthorhombic crystal structures may be obtained [39]. According to the effective ionic radii of typical perovskite $CH_3NH_3PbX_3$ listed in Table 1.1, the tolerance factors of $CH_3NH_3PbI_3$ and $CH_3NH_3PbBr_3$ can be calculated as 0.91 and 0.93 respectively i.e. cubic crystal structure can be predominantly formed [40]. Moreover, the crystal structures and transition temperatures for typical perovskites are summarized in Table 1.2. According to the data described in Table 1.2, $CH_3NH_3PbI_3$ maintains a tetragonal structure between 162 K and 330 K. When the temperature decreases, the tetragonal phase can be transformed to the orthorhombic structure.

Table 1.1: Effective ionic radii of CH3NH3PbX3(X=Cl, Br, I) [41, 42, 43]

Cation A	Effective ion radius (Ȧ)	Cation B	Effective ion radius (Ȧ)	Anion X	Effective ion radius (Ȧ)
Methylammonium $[CH_3NH_3]^+$	2.17	Pb^{2+}	1.19	Cl-	1.81
				Br-	1.96
				I-	2.2

Table 1.2: Crystal structures and transition temperatures of $CH_3NH_3PbX_3$ (X=Cl, Br, I) [44-47]

Perovskite	Temperature	Crystal system	Space group	Lattice parameters
$CH_3NH_3PbI_3$	< 161K	Orthorhombic	Pnma	a= 8.84 Å, b= 12.6Å, c= 8.56 Å,
	162-330K	Tetragonal	I4/mcm	a= 6.391 Å , c= 12.685Å
	>330K	Cubic	Pm3m	a= 6.391 Å
$CH_3NH_3PbBr_3$	< 154K	Orthorhombic	$Pna2_1$	a= 7.98 Å, b= 8.58 Å, c= 11.85 Å,
	155-149K	Tetragonal	I4/mcm	a= 5.894 Å , c= 5.861Å
	>236K	Cubic	Pm3m	a= 5.93 Å
$CH_3NH_3PbCl_3$	< 172K	Orthorhombic	$P222_1$	a= 5.67 Å, b= 5.63 Å, c= 11.18 Å,
	172-177K	Tetragonal	P4/mmm	a= 5.656 Å, c= 5.63 Å
	>178K	Cubic	Pm3m	a= 5.67 Å

1.5 Optoelectronic properties of perovskite materials

Perovskite materials have unique optical and electrical properties, which make it as a promising photovoltaic material. To understand the transport properties and device degradation mechanisms, we need to know the fundamental electrical and optical properties of the film.

1.5.1 Absorption coefficient

One of the superior properties of the organic-inorganic perovskite materials is its very high absorption coefficient with the sharp onset of the absorption edge. They possess excellent characteristics of harvesting light and serve as a very capable hole-transporting medium as it has the properties of transporting the hole generated [48]. In the reference [49], the absorption coefficient ($\sim10^5$- 10^6) cm^{-1} was reported by Xiang's group. That means about 100 nm to 1 μm of perovskite film is enough to absorb most of the incident photons efficiently. Due to its high absorption coefficient, the amount of light absorbed by the solar cell is also increased, which primarily increases the amount of charge carriers generated due to the light incident i.e., photogeneration rate is increased. Therefore, the loss of energy can also be reduced and also the collection of charge carriers can be increased at the respective electrodes [50].

1.5.2 Diffusion length

A lot of research groups have already reported that perovskite materials possess very high carrier diffusion length and high collection efficiency i.e. they have high carrier mobility and carrier lifetime.[51,53] The diffusion length can vary on the temperature measured due to the changes of recombination mechanisms [54]. Reported diffusion length is the order of micro-meters [51, 52, 54].

1.5.3 Dielectric constants and exciton binding energy

The dielectric constant has a significant impact on solar cell performance. The energy required to dissociate the excitions (the pairs of holes and electrons generated by light absorptions) is called exciton binding energy. The excition binding energy can be calculated as follows.

$$E_b = \frac{e^4 \mu_{eff}}{8{\varepsilon_r}^2{\varepsilon_0}^2 h^2}\frac{1}{n^2} \tag{1.2}$$

where μ_{eff} $(m_h^* m_e^*/(m_h^* + m_e^*))$ is the effective reduced mass of the excitons and n is the quantum number (N=1). According to the Eq. 1.2, higher relative dielectric constants ε_r and smaller effective masses m_h^*, m_e^* may cause the lower exciton binding energies. For the $MAPbI_3$, the dielectric constant and the exciton binding energy were reported to be about 6.5 [55] and 50 meV [56], respectively.

1.5.4 Charge carrier mobility

One of the most essential features in the semiconductor device is the charge transport in the active materials. Following the prominent results of hybrid perovskite photovoltaic, theoretical and experimental studies have been conducted to investigate the charge transport characteristics. Based on the ab initio calculation, large hole and electron motilities of lead-based perovskite were respectively predicted up to 1500-3100 $\mathrm{cm^2V^{-1}s^{-1}}$ and 800-1500 $\mathrm{cm^2V^{-1}s^{-1}}$ with a carrier concentration of 10^{16} to 10^{19} $\mathrm{cm^{-3}}$[57]. For the spin-coated thin film of tin-based hybrid perovskite $(C_6H_5C_2H_4NH_3)_2SnI_4$, the field-effect motilities of 1×10^{-3} $\mathrm{cm^2V^{-1}s^{-1}}$ with an I_{on}/I_{off} ratio above 10^4 was reported [58-60]. By using transient THz spectroscopy, high carrier mobility for the solution-processed material was determined as $8\ \mathrm{cm^2V^{-1}s^{-1}}$ [61]. Chin et al. investigated the intrinsic charge transport parameters of

$CH_3NH_3PbI_3$ by fabricating high-quality hybrid perovskite FETs. This group observed that the screening effects associated with the ionic transport could be effectively eliminated by lowering the measurement temperature and reported as the electron and hole mobility as $7.2 \times 10^{-2}\ \mathrm{cm^2V^{-1}s^{-1}}$ and $2.1 \times 10^{-2}\ \mathrm{cm^2V^{-1}s^{-1}}$ at 78 K [62]. The basic electrical properties such as carrier type, concentration, and mobility in perovskite were also demonstrated to be significantly influenced by their synthesis methods [63, 64]. We can see a wide range of carrier mobility values even if the same measurement methods are used. For example, for same single crystal $MAPbI_3$, a large range from hole mobility of $2.5\ \mathrm{cm^2V^{-1}s^{-1}}$[65] to electron-hole sum mobility of $600\ \mathrm{cm^2V^{-1}s^{-1}}$[66], that is probably due to not only experimental but also measuring condition. Therefore, the carrier transport properties in the organic-inorganic halide perovskites are strongly influenced by the fabrication process, morphology, defects, grain boundaries, and environmental effects [66].

1.6 Deposition methods

One of the key attractions of halide perovskites is the simplicity of their preparation, and they can be fabricated by two strategies, precipitation from solution and deposition from the vapor phase. Two-step process in both solution and vapor phases have been investigated. The simplest method is precipitation from solution; the precursor PbI_2 and MAI are dissolved in one solution (DMSO or DMF) and evaporation of the solvent by heating after spin coating yields perovskite crystals. However, forming homogenous and pinhole-free films has still challenged [67]. During spin-coating, adding toluene or chloroform to the spin-coated film has offered improvement in film morphology [68-71].

To explore better control for morphology and crystallinity, two-step solution process was developed and gained higher efficiency [72]. In this approach, first PbI_2 and DMF solution are spin-coated onto a substrate, and then annealed, following by spin-coated repeatedly with an alcoholic solution of CH_3NH_3I to convert the lead halide film into perovskites [72-73]. Moreover, vapor-phase methods have also been used to produce hybrid perovskites. Directly co-evaporate the two PbI_2 and CH_3NH_3I in a vacuum deposition chamber yields highly uniform films with brilliant photovoltaic qualities [74]. For two-step vapor deposition method, PbI_2 is deposited from solution and then convert to the perovskites by exposure to CH_3NH_3I vapor [75]. In this study, we used a simple solution deposition method one-step and two-step. The detailed procedure for fabrication will be explained in Section 2.2.

1.7 Applications beyond photovoltaics

As discussed above, organometal halide perovskites offer a combination of the advantages of relatively high carrier mobility of inorganic semiconductor and low temperature and solution-based processability of organic semiconductor. Moreover, their great enticing potential such as high absorption coefficient, tunability of their optoelectronic properties, relatively high diffusion length and radiative carrier lifetime extend their application into not only photovoltaic field but also numerous optoelectronic applications. Here a broad range of halide perovskite-related applications, such as light emitting diodes (LEDs) [76, 77] , lasers [78, 79], phtotodetectors [80] , memory devices, and more.

1.8 Challenges

Although astounding progress has been made in a short period of time for the efficiency of perovskite photovoltaic solar cells, there are still remaining significant challenges for reducing toxicity (Pb-containing), take care of instability (degradation on exposure to moisture) and for unexpected behaviors (J-V hysteresis). In the following, I will give a short overview of the challenges.

1.8.1 Toxicity

While as significantly improved the efficiency, toxicity issue of lead halide perovskite is still a serious problem for commercial use. Even though it is implemented only small quantities in solar cells, there is a potential risk of harms on humans and environments [81]. Therefore, new researches are emerging for replacing the lead with other elements. Up to now, not only tin-based perovskites but also other elements such as germanium, copper, antimony, or bismuth are already showing promising properties as listed at Table 1.3 with references [82, 83]. However, it is still big challenge to replace lead with other elements which new non-toxic, earth abundance, and environmentally absorbers.

Table 1.3: Optical bandgap and power conversion efficiencies (PCEs) of lead-free perovskite absorber materials for photovoltaic application [84-88]

Perovskite	Bandgap (eV)	PCE (%)
$CH_3NH_3SnI_3$	1.23	6.4

$CH_3NH_3GeI_3$	2.0	0.20
$(CH_3(CH_2)_3NH_3)_2CuBr_4$	1.76	0.63
$Rb_3Sb_2I_9$	2.1	0.66
$Cs_3Bi_2I_9$	2.2	1.09

1.8.2 Stability

Stability is the most challenging issue to maintain a stable power output under a standard working condition for being practical applications. As we all know, most hybrid organic-inorganic perovskites suffer instability under ambient condition. At present, even though the degradation mechanisms are not clearly understood, illumination, humidity, and high temperature have been demonstrated for long term device stability of perovskite materials [89-91].

When exposed to high humidity, $CH_3NH_3PbI_3$ easily decompose to the dissolved hydraulic acid and volatile methylamine, because the weak hydrogen bonding between organic and inorganic is strongly affected by the high polarity of the water molecule. However, the insoluble PbI_2 remains as follows [89, 92].

$$CH_3NH_3PbI_3 \longrightarrow PbI_2 + CH_3NH_2 \uparrow + HI \uparrow$$

Moreover, Pistor et al. reported that hybrid perovskites thermally decomposed when annealing at 200 °C even in a vacuum while standard annealing at 100-150 °C enhanced the crystallinity [93]. The reason for decomposition of PbI_2 is probably due to weak hydrogen bonding from $CH_3NH_3^+$ and PbI_6. Therefore, FA^+ and inorganic Cs^+ have been introduced to be more stable [94].

Regarding for the better stability, $(C_6H_5CH_2NH_3)_2(FA)_8Pb_9I_{28}$ quasi-2D perovskite film are being addressed by Dai and co-workers [95], and they also proposed 3D perovskite to improve the stability against moisture through the use of surface passivation [96-98]. Encapsulation techniques using glass sealing or laminate plastic films play an important role to improve device stability and accelerate to the practical applications [99].

There are many strategies to enhance the stability issues in terms of changing the structural effects [100], inserting hole and electron transporting layers [101, 102] and device encapsulation [99]. However, the instability issue still remains to overcome for commercialization.

1.8.3 J-V hysteresis (Unusual behaviors)

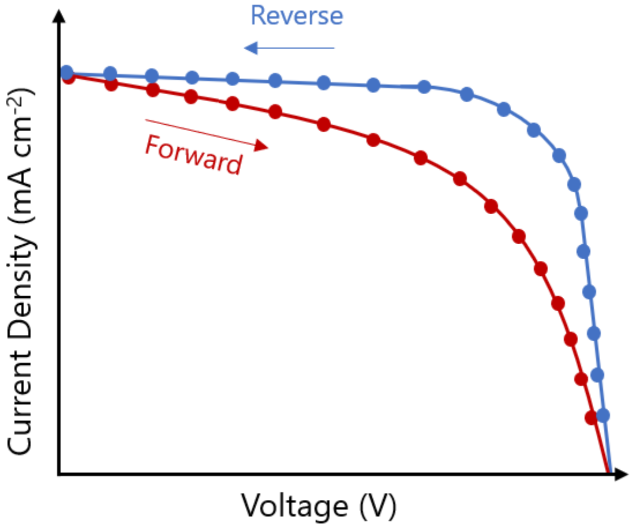

Figure 1.3: Current-voltage hysteresis encountered in perovskite solar cells.

Another major obstacle issue is the photocurrent hysteresis in J-V measurement for measurement of power conversion efficiency. Hysteresis can be defined as the shape and magnitude of the measured current are varied significantly with different scan direction (from reverse to forward bias or vice-vasa) as shown in Fig. 1.3 and scan rate that hinders the accurate device efficiency. Under great success, the impacting factors for hysteresis are still under investigation, but these are commonly attributes to the unusual behaviors of perovskite materials. In 2014, Snaith et al. firstly reported the possible origins of hysteresis phenomenon such as 1) slow polarization cause by ferroelectric property, 2) trapping and detrapping of charges due to surface defects, 3) ion migration. So far, the mechanisms of the hysteresis have been investigated.

1.8.3.1 Ferroelectric effects

Ferroelectricity is one possibility for the origin of J-V hysteresis. Ferroelectric can occur in organic metal halide perovskites at the room temperature because it adopts a tetragonal structure between 162 K and 330 K as listed in Table 1.2. A ferroelectric material has spontaneous electric polarization, which can be reversed by the external electric field. The flip of the dipoles induced the polarization of photogenerated charges and contributed to the photocurrents hysteresis. Based on density functional theory (DFT), electronic polarization of $MAPbI_3$ was predicted to be 38 $\mu C/cm^2$ by Frost and co-workers [103]. For experimental evidence, Wei et al. strongly attributed the ferroelectricity of $MAPbI_2Cl$ by electrical field polarization loop [104, 105]. After that, Kutes et al. successfully studied the mechanism of ferroelectric domains in $MAPbI_3$ by piezo response force microscopy (PFM) [106]. However, Zhen Fan et al. reported $MAPbI_3$ was not ferroelectric at room temperature; however, it was possible to induce and experimentally observe apparent ferroelectric behavior through the proposed ways [107, 105]. Thus, the existence of the ferroelectricity in perovskite is still conflicting from the theoretical and experimental studies.

1.8.3.2 Trapping and detrapping effects

The dynamic electric field and charge injection modulated charge trapping and detrapping process are one possible mechanism for photocurrent hysteresis [108]. At initial reverse scanning (open to short circuit), the surface traps have already been filled by the injected charges for positive bias voltage. Thus, the photo-generated charges can be possible large photocurrent with high efficiency. Inversely, when the initial forward scanning (short to open circuit), the traps are depleted by reverse bias, and low photocurrent is observed because the photogenerated charges will be captured by these traps. Therefore, if the amount of trap state on the layer can be reduced, we can avoid the photocurrent hysteresis caused by traps. Qi Wang et al. demonstrated that hysteresis could be reduced by adopting the fullerene layer on the top of perovskites due to the reduction of the traps [109].

1.8.3.3. Ion migration

Ion migration in perovskites could give the I-V hysteresis. In $MAPbI_3$ perovskite, both MA^+ and I^- are migrating. At 2015, Edmands et al. that claimed the evidence of ion migration [110]. Perovskites are known as both semiconductors and ionic conductor due to the combined nature of carrier flow and ion flow. According to the Table 1.3, the evaluation of activation energy for ionic migration pointed to iodide vacancies as the easiest mobile species [111]. Eames et al. also confirmed that mobile species (mostly iodide vacancies) migrate under the influence of electric field and pile up near the interfaces that caused the screening the applied electric field then affects for the hysteresis. The diffusion constant of I^- ions as 10^{-9} cm^2/s was estimated [111]. Nevertheless, the reported diffusion constants and conductivities of ion in $MAPbI_3$ thin films vary in a wide range.

Table 1.3: Activation Energy of each ion vacancies [111]

Ion vacancies	Activation energy (eV)
I^-	0.08
MA^+	0.46
Pb^{2+}	0.80

1.9 Motivation and objectives of the present study

As we all know, organic-inorganic perovskites are arising as a new generation of low-cost active materials for solar cells with efficiency from 3.5% to over 25% within only ten years. They promise both the superior carrier mobility of inorganic semiconductors and the processability of organic semiconductors, combining with efficient characteristics such as easy of processing, available solution processing, and cost-effectiveness as described before. However, the unusual carrier behavior is still under ambiguities as described as subsection 1.8.3. To be clear for these anomalous behaviors, we need to study the fundamental transport properties such as charge injection, carrier accumulation and transport mechanism. Therefore, to visualize the carrier transport for independent evaluation of the fundamental transport properties of these type of materials is our main motivation for this study. Because we have a unique technique to visualize carrier transport and polarization structure from top of the FET device on the basis of electric field induced second harmonic generation (EFISHG). On the other hand, EFISHG is a powerful nonlinear optical approach, and it is applicable to characterizing the carrier behavior in organic electronic device because the charge is also a source of an electric field. The optical method can not only provide the information about electric field distribution but also its time-resolved evolution, which makes it a powerful tool for directly probing the carrier behavior of the organic materials [112].

However, the perovskite materials show the multi-photon excited fluorescence, and it may sometimes interfere with the weak SHG signal during the EFISHG measurement. Therefore, comprehensive investigation on the fundamental properties of perovskite material properties has been conducted by Photoluminescence (PL) imaging method also.

The reason for why we choose the FET instead of solar cell structure is that we can clearly see the carrier behavior between two electrode on the top of the FET devices, rather than solar cell structure. Moreover, FETs provide a flexible platform to study the carrier transport mechanism of semiconductor devices, as explained in section 1.1.

The primary focus of this dissertation is the study the fundamental carrier transport characteristics of organic-inorganic hybrid perovskites by using spectroscopic measurements, such as EFISHG and PL technique. In addition, we conducted the FET measurements and time of flight (TOF) methods to observe the electrical characteristics more clearly for our fabricated film. If we know the electrical and optical properties of perovskite, we can improve the devices not only solar cells but also other optical devices of these materials. Therefore our future prospect is to approach for the developments of the perovskite community based on the EFISHG and PL techniques. Figure 1.4 shows the structure of the dissertation.

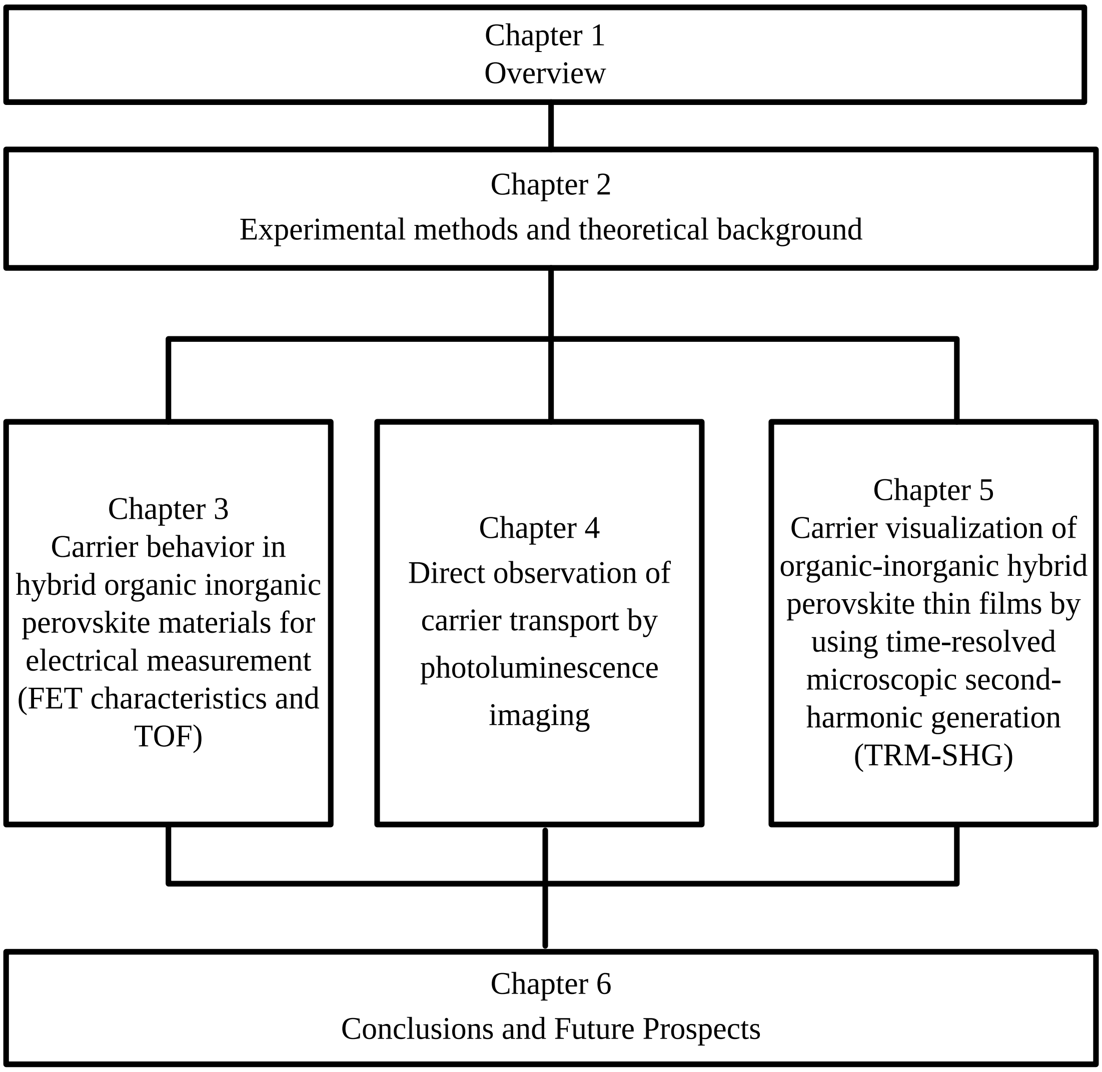

Figure 1.4: Flow chart of the arrangement of this dissertation

In chapter 1, a general introduction of perovskite hybrid solar cells, including working mechanism and development is given out. The required background knowledge and state of the current literature is given in detail in chapter 1, which provides a general introduction to photovoltaics of perovskites. Moreover, deposition methods and a wide range of applications of perovskite are briefly introduced. Under great success, some challenges are stated in section 1.8. Finally, the motivation and the objectives of the present study are illustrated.

Chapter 2 describes the experimental methods and theoretical models for measurements. Firstly, device fabrication and characterization techniques are described. Then, the principle and experimental methods of relevant analysis used for this study, such as FET measurements, conventional TOF, and lateral TOF, EFISHG, and PL have been described. Besides, for charge carrier transport, transmission line approximation, and interface charge propagation model are briefly introduced. So far, chapter 3, 4, and 5 describe the observations, the experimental results, and conclusions for related experiment methods.

In chapter 3, I conducted the FET measurement and lateral TOF experiments for electrical characteristics. The results and observations of FET measurement and lateral TOF methods will be concluded at the end of the chapter. As the same procedure, for chapter 4, the carrier visualization of perovskite material for PL method, followed by analyzing the origin of PL mechanism are discussed. Then detailed experiment, results, and conclusion are discussed. Then in chapter 5, we have studied the TRM-SHG method to observe the direct electric field distribution through the channel. Interestingly, we can discuss not only the carrier mobility and carrier behavior, but we can also estimate the trapped charged from the peak of the SHG profile.

Finally, in chapter 6, I will summarize the general conclusion based on the detailed conclusion in the previous chapters and followed by an outlook for future perspectives.

Bibliography

[1] International Energy Agency. World Energy Outlook Special Report: Energy and Air Pollution (OECD/IEA, 2016).

[2] World Energy Council. World Energy Scenarios (World Energy Council, 2013).

[3] M. K. Nazeeruddin, “In retrospect: twenty-five years of low-cost solar cells,” Nature 538 (7626), 463 – 464, 2016.

[4] J. Dore, D. Ong, S. Varlamov, R. Egan and M. A. Green, “Progress in laser-crystallized thin-film polycrystalline silicon solar cells: intermediate layers, light trapping, and metallization,” IEEE J Photovolt. 4(1), 33–39, 2013.

[5] P.H.D. Lu, D. Lin, X. Wang, A. Lennon and S. Wenham, “Laser doping through anodic aluminium oxide silicon solar cell,” Sol. Energy Mater. Sol. Cells 145, 349–357, 2016.

[6] R .Venkatasubramanian, M.L. Timmons, P.R. Sharps and J.A. Hutchby, “18.2% (am1.5) efficient gas solar cell on optical-grade polycrystalline Ge substrate In: Photovoltaic Specialists Conference, 1993,” Conference Record of the Twenty Third IEEE, 691–695, 1996.

[7] H. J. Snaith, “Perovskites: the emergence of a new era for low-cost, high-efficiency solar cells,” J. Phys. Chem. Lett. 4, 21, 3623–3630, 2013.

[8] A. Kojima, K. Teshima, Y. Shirai and T. Miyasaka, “Organometal halide perovskites as visible-light sensitizers for photovoltaic cells,” J. Am. Chem. Soc. 131, 17, 6050–6051, 2009.

[9] http://www.nrel.gov/ncpv/images/efficiency_chart.jpg NREL efficiency chart.

[10] H. S. Kim, C. R. Lee, J.H. Im, K. B. Lee and T. Moehl, “Lead iodide perovskite sensitized all-solid-state submicron thin film mesoscopic solar cell with efficiency exceeding 9%,” Sci. Rep. 2, 591, 2012.

[11] N. J. Jeon, J. H. Noh, Y. C. Kim, W. S. Yang , S. Ryu and S. I. Seok SI, “Solvent engineering for high-performance inorganic-organic hybrid perovskite solar cells,” Nat. Mater. 13, 9, 897, 2014.

[12] M.A. Green, A. Ho-Baillie and H. J. Snaith, “The emergence of perovskite solar cells,” Nat. Photonics 8, 7, 506–514, 2014.

[13] J. M. Frost, K. T. Butler, and A. Walsh, "Molecular ferroelectric contributions to anomalous hysteresis in hybrid perovskite solar cells," Apl. Materials 2, 8, 081506, 2014.

[14] H. J. Snaith, A. Abate, J. M. Ball, G. E. Eperon, T. Leijtens, N. K. Noel, S. D. Stranks, J. T. Wang, K. Wojciechowski, and W. Zhang, "Anomalous hysteresis in perovskite solar cells," J. Phys. Chem. Lett. 5, 9, 1511-1515, 2014.

[15] Y. Shao, Z. Xiao, C. Bi, Y. Yuan, and J. Huang, "Origin and elimination of photocurrent hysteresis by fullerene passivation in CH3NH3PbI3 planar heterojunction solar cells," Nat. commun. 5, 5784, 2014.

[16] E.L. Unger, E. T. Hoke, C. D. Bailie, W. H. Nguyen, A. R. Bowring, T. Heumüller, M. G. Christoforo, and M. D. McGehee, "Hysteresis and transient

behavior in current–voltage measurements of hybrid-perovskite absorber solar cells," Energ. Environ. Sci. 7, 11, 3690-3698, 2014.

[17] T. Manaka, E. Lim, R. Tamura, and M. Iwamoto. "Direct imaging of carrier motion in organic transistors by optical second-harmonic generation," Nat. photonics 1, 10, 581, 2007.

[18] T. Manaka, and M. Iwamoto, "Optical second-harmonic generation measurement for probing organic device operation," Light Sci. Appl. 5, 3, e16040, 2016.

[19] T. Manaka, E. Lim, R. Tamura, and M. Iwamoto. "Modulation in optical second harmonic generation signal from channel of pentacene field effect transistors during device operation," Appl. Phys. Lett. 87, 22, 222107, 2005.

[20] W. Travis, E. N. K. Glover, H. Bronstein, D. O. Scanlon, and R. G. Palgrave, "On the application of the tolerance factor to inorganic and hybrid halide perovskites: a revised system," Chem. Sci. 7, 7, 4548-4556, 2016.

[21] D. Weber, "CH3NH3PbX3, a Pb (II)-system with cubic perovskite structure," Z. Naturforsh B 33, 12, 1443-1445, 1978.

[22] D. Weber, "$CH_3NH_3SnBr_xl_3$ x (x= 0-3), a Sn (II)-System with Cubic Perovskite Structure," Z. Naturforsh, 33b, 862-865, 1978.

[23] D. B. Mitzi, C. A. Field, W.T.A Harrison and A. M. Guloy, Nature 369, 467, 1994.

[24] K Liang, D. B. Mitzi, M. T. Prikas, “Synthesis and characterization of organic–inorganic perovskite thin films prepared using a versatile two-step dipping technique,” Chem. Mater. 10, 403-411, 1998.

[25] J. H. Burroughes, D. D. C Bradley, A. R. Brown, R. N. Marks, K. Mackay, R. H. Friend, P. L. Burns, A. B. Holmes, “Light-emitting diodes based on conjugated polymers,” Nature 347, 539-541, 1990.

[26] C. R. Kagan, D. B. Mitzi, C. D. Dimitrakopoulos, “Organic-inorganic hybrid materials as semiconducting channels in thin-film field-effect transistors,” Science 286, 945-947, 1999.

[27] J. H. Im, C. R. Lee, J. W. Lee, S. W. Park, and N. G Park. “6.5% efficient perovskite quantum-dot-sensitized solar cell,” Nanoscale 3, (10), 4088-4093, 2011.

[28] L. Etgar, P. Gao P, Z. Xue, Q. Peng, A. K.Chandiran, B. Liu, M. K. Nazeeruddin and M . Grätzel, “Mesoscopic CH3NH3PbI3/TiO2 heterojunction solar cells,” J. Am. Chem. Soc. 134 (42) 17396-9, 2012.

[29] M. M. Lee, J. Teuscher, T. Miyasaka, T. N. Murakami, H. J. Snaith, “Efficient hybrid solar cells based on meso-superstructured organometal halide perovskites,” Science 338, 643-647, 2012.

[30] H. S. Kim, C. R. Lee, J. H. Im, K. B Lee, T. Moehl, A. Marchioro, S. J. Moon, R. H. Baker, J. H. Yum, J. E. Moser, M. Gratzel, N. G. Park, “Lead iodide perovskite sensitized all-solid-state submicron thin film mesoscopic solar cell with efficiency exceeding 9%,” Sci. Rep. 2, 591, 2012.

[31] J. Burschka, N. Pellet, S. J. Moon, R. H. Baker, P. Gao, M. K. Nazeeruddin, M. Gratzel, “Sequential deposition as a route to high-performance perovskite-sensitized solar cells,” Nature 499, 316-319, 2013.

[32] M. Liu, M. B. Johnston, H. J. Snaith, “Efficient planar heterojunction perovskite solar cells by vapour deposition,” Nature 501, 395-398, 2013.

[33] H. Zhou, Q. Chen, G. Li, S. Luo, T. B. Song, H. S. Duan, Z. Hong, J. You, Y. Liu, Y. Yang, “ Interface engineering of highly efficient perovskite solar cells,” Science 345, 542-546, 2014.

[34] N. J. Jeon, J. H. Noh, Y. C. Kim, W. S. Yang, S. Ryu, S. I. Seok, “Solvent engineering for high-performance inorganic–organic hybrid perovskite solar cells,” Nat. Mater. 13, 897-903, 2014.

[35] N. J. Jeon, J. H. Noh, W. S. Yang, Y. C. Kim, S. Ryu, J. Seo and S. I. Seok, “Compositional engineering of perovskite materials for high-performance solar cells. Nature 517, 7535, 476, 2015.

[36] H. Zhou, Q. Chen, G. Li, S. Luo, T. Song, H. S. Duan, Z. Hong, J. You, Y. Liu, Y. Yang, “Interface engineering of highly efficient perovskite solar cells,” Science 345, 542-546, 2014.

[37] M. A. Green, K. Emery, Y. Hishikawa, W. Warta and E. D. Dunlop “Solar cell efficiency tables (Version 45)” Prog. Photov, Res. Appl. 23, 1- 9, 2015.

[38] W. S. Yang, B. W. Park, E. H. Jung, N. J. Jeon, Y. C. Kim, D. U. Lee, S. S. Shin, J. Seo, E. K. Kim, J. H. Noh and S. I. Seok, “ Iodide management in formamidinium-lead-halide–based perovskite layers for efficient solar cells,” Science 356 , 2017.

[39] M. Johnsson, P. Lemmens, “Crystallography and chemistry of perovskies. In: Handbook of magnetism and advanced magnetic materials,” Wiley online library, 2007.

[40] S. F. Hoefler, G. Trimmel, and T. Rath, "Progress on lead-free metal halide perovskites for photovoltaic applications: a review," Monatshefte für Chemie-Chemical Monthly 148 (5) 795-826, 2017.

[41] G. Kieslich, S. Sun, and A. K. Cheetham, "Solid-state principles applied to organic–inorganic perovskites: new tricks for an old dog," Chem. Sci. 5 (12) 4712-4715, 2014.

[42] R. D. Shannon, "Revised effective ionic radii and systematic studies of interatomic distances in halides and chalcogenides," Acta crystallographica section A: crystal physics, diffraction, theoretical and general crystallography 32, (5), 751-767, 1976.

[43] B. Saparov, D. B. Mitzi. "Organic–inorganic perovskites: structural versatility for functional materials design," Chem. Rev. 116, (7) 4558-4596, 2016.

[44] T. Oku, "Crystal structures of CH3NH3PbI3 and related perovskite compounds used for solar cells," Solar Cells-New Approaches and Reviews 1, 2015.

[45] O. Knop, R. E. Roderick, M. A. White, T. S. Cameron, and M. J. M. V. Oort. "Alkylammonium lead halides. Part 2. CH3NH3PbX3 (X= Cl, Br, I) perovskites: cuboctahedral halide cages with isotropic cation reorientation," Can J Chem 68 (3) 412-422, 1990.

[46] D. B. Mitzi, “In Progress in Inorganic Chemistry,” (Ed: K. D. Karlin) John Wiley & Sons, Inc., Hoboken, NJ. 1–121, 2007.

[47] R. E. Wasylishen, K. Osvald and J. B. Macdonald, "Cation rotation in methylammonium lead halides," Solid State Commun. 56, (7), 581-582, 1985.

[48] T. L. Amu, “Performance Optimization of tin halide Perovskite solar cells via Numerical Simulation,” A Thesis presented to the Department of Theoretical Physics African University of Science and Technology, Abuja, 1-20, 2014.

[49] X. Ziang, L. Shifeng, Q. Laixiang, P. Shuping, W. Wei, Y. Yu, Y. Li et al. "Refractive index and extinction coefficient of CH3NH3PbI3 studied by spectroscopic ellipsometry," Opt. Mater. Express 5 (1) 29-43, 2015.

[50] A. M. Bagher, M. M. A. Vahid and M. Mohsen, “Types of solar cells and application,” American Journal of Optics and Photonics 3 (5), 94-113, 2015.

[51] Y. Zhao, A.M. Nardes, and K. Zhu, “Solid-state mesostructured perovskite CH3NH3PbI3 solar cells: charge transport, recombination, and diffusion length. J. Phys. Chem. Lett. 5 (3) 490-494, 2014.

[52] S. D. Stranks, G. E. Eperon, G. Grancini, C. Menelaou, M. J. P. Alcocer, T. Leijtens, L. M. Herz, A. Petrozza and H. J. Snaith, “Electron-hole diffusion lengths exceeding 1 micrometer in an organometal trihalide perovskite absorber,” Science 342 (6156) 341-344, 2013.

[53] C. L. O. Vorakiat, T. Salim, J. Kadro, M. T. Khuc, R. Haselsberger, L. Cheng, H. Xia, G. G. Gurzadyan, H. Su, et al., “Elucidating the role of disorder and free-carrier recombination kinetics in CH3NH3PbI3 perovskite films,” Nat. Commun. 6, 9703, 2015.

[54] C. C. Stoumpos, C.D. Malliakas, and M.G. Kanatzidis, “Semiconducting tin and lead iodide perovskites with organic cations: phase transitions, high mobilities, and near-infrared photoluminescent properties” Inorg. Chem. 52 (15) 9019-9038, 2013.

[55] M. Hirasawa, T. Ishihara, T. Goto, K. Uchida, and N. Miura. "Magnetoabsorption of the lowest exciton in perovskite-type compound (CH3NH3) PbI3," Physica B: Condensed Matter 201, 427-430, 1994.

[56] K. Tanaka, T. Takahashi, T. Ban, T. Kondo, K. Uchida, and N. Miura. “Comparative study on the excitons in lead-halide-based perovskite-type crystals CH3NH3PbBr3 CH3NH3PbI3,” Solid State Commun. 127, (9-10) 619-623, 2003.

[57] Y. He and G. Galli. “Perovskites for solar thermoelectric applications: A first principle study of CH3NH3AI3 (A= Pb and Sn),” Chem. Mater. 26 (18) 5394-5400, 2014.

[58] C. R. Kagan, D. B. Mitzi, and C. D. Dimitrakopoulos, “Organic-inorganic hybrid materials as semiconducting channels in thin-film field-effect transistors,” Science 286, 5441, 945-947, 1999.

[59] D. B. Mitzi, C. D. Dimitrakopoulos, and L. L. Kosbar. “Structurally tailored organic− inorganic perovskites: optical properties and solution-processed channel materials for thin-film transistors,” Chem. Mater. 13, (10) 3728-3740, 2001.

[60] D. B. Mitzi, C. D. Dimitrakopoulos, J. Rosner, D. R. Medeiros, Z. Xu, and C. Noyan, “Hybrid field-effect-transistor based on a low-temperature melt-processed channel layer,” Adv. Mater 14 (23)1772-1776, 2002.

[61] C. Wehrenfennig, G. E. Eperon, M. B. Johnston, H. J. Snaith, and L. M. Herz, “High charge carrier mobilities and lifetimes in organolead trihalide perovskites,” Adv. Mater. 26 (10) 1584-1589, 2014.

[62] X. Y. Chin, D. Cortecchia, J. Yin, A. Bruno, and C. Soci, “Lead iodide perovskite light-emitting field-effect transistor,” Nat. Commun. 6 , 7383, 2015.

[63] Q. Wang, Y. Shao, H. Xie, L. Lyu, X. Liu, Y. Gao, and J. Huang, “Qualifying composition dependent p and n self-doping in CH3NH3PbI3,” Appl. Phys. Lett. 105, (16), 163508, 2014.

[64] Y. Takahashi, R. Obara, Z. Z. Lin, Y. Takahashi, T. Naito, T. Inabe, S. Ishibashi, and K. Terakura, “Charge-transport in tin-iodide perovskite CH 3 NH 3 SnI 3: origin of high conductivity,” Dalton Trans. 40 (20) 5563-5568, 2011.

[65] D. A. V. Chavez, C. S. Ponseca, C. C. Stoumpos, A. Yartsev, M. G. Kanatzidis, V. Sundström, D. G. Cooke, “Intrinsic femtosecond charge generation dynamics in single crystal CH3NH3PbI3,” Energy Environ. Sci. 8, 3700−3707, 2015.

[66] Z. K. Tan, R. S. Moghaddam, M. L. Lai, P. Docampo, R. Higler, F. Deschler, M. Price, A. Sadhanala, L. M. Pazos, D. Crddgington, F. Hanusch, T. Bein, H. J. Snaith, and R. H. Friend, “ Bright light- emitting diodes based on organometal halide perovskite” Nat. Nanotech. 9, 687, 2014.

[67] T. C. Sum and N. Mathews, “Advancements in perovskite solar cells: photophysics behind the photovoltaics,” Energy Environ. Sci. 7, 2518 , 2014.

[68] J. H. Heo, D. H. Song, and S. H. Im “Planar CH3NH3PbBr3 hybrid solar cells with 10.4% power conversion efficiency, fabricated by controlled crystallization in the spin-coating process,” Adv. Mater. 26, 8179 , 2014.

[69] Z. Xiao, Q. Dong, C. Bi, Y. Shao, Y. Yuan, and J. Huang “Solvent annealing of perovskite-induced crystal growth for photovoltaic-device efficiency enhancement,” Adv. Mater. 26, 6503 , 2014.

[70] J. H. Im, I. H. Jang, N. Pellet, M. Grätzel, and N.-G. Park “Growth of CH3NH3PbI3 cuboids with controlled size for high-efficiency perovskite solar cells,” Nat. Nanotechnol. 9, 927 , 2014.

[71] G. E. Eperon, S. D. Stranks, C. Menelaou, M. B. Johnston, L. M. Herz, and H. J. Snaith “ Formamidinium lead trihalide: a broadly tunable perovskite for efficient planar heterojunction solar cells,” Energy Environ. Sci. 7, 982 , 2014.

[72] J. Burschka, N. Pellet, S. J. Moon, R. H. Baker, P. Gao, M. K. Nazeeruddin, and M. Grätzel “Sequential deposition as a route to highperformance perovskite-sensitized solar cells,” Nature 499, 316, 2013.

[73] P. Docampo, F. Hanusch, S. D. Stranks, M. Döblinger, J. M. Feckl, M. Ehrensperger, N. K. Minar, M. B. Johnston, H. J. Snaith, and T. Bein “Solution deposition-conversion for planar heterojunction mixed halide perovskite solar cells,” Adv. Energy Mater. 4, 1400355, 2014.

[74] M. Liu, M. B. Johnston, and H. J. Snaith “Efficient planar heterojunction perovskite solar cells by vapour deposition,” Nature 501, 395, 2013.

[75] Q. Chen, H. Zhou, Z. Hong, S. Luo, H. Duan, H. Wang, Y. Liu, G. Li, and Y. Yang “Planar heterojunction perovskite solar cells via vapor-assisted solution process,” J. Am. Chem. Soc. 136, 622 ,2014.

[76] Z. K. Tan, R. S. Moghaddam, M. L. Lai, P. Docampo, R. Higler, F. Deschler, M. Price et al. "Bright light-emitting diodes based on organometal halide perovskite," Nat. nanotechnol,” 687, 2014.

[77] Y. H. Kim, H. Cho, J. H. Heo, T. S. Kim, N. Myoung, C. L. Lee, S. H. Im and T. W. Lee, “Multicolored organic/inorganic hybrid perovskite light-emitting diodes,” Adv. Mater. 27 (7) 1248-1254, 2015.

[78] F. Deschler, P. Michael, S. Pathak, L. E. Klintberg, D. D. Jarausch, R. Higler, S. Hüttner et al. “High photoluminescence efficiency and optically pumped lasing in solution-processed mixed halide perovskite semiconductors,” J. Phys. Chem. Lett 5, (8)1421-1426, 2014.

[79] B. R. Sutherland, S. Hoogland, M. M. Adachi, C. T. Wong, and E. H. Sargent, “Conformal organohalide perovskites enable lasing on spherical resonators,” ACS nano 8 (10) 10947-10952, 2014.

[80] Q. Zhang, S. T. Ha, X. Liu, T. C. Sum, and Q. Xiong, “Room-temperature near-infrared high-Q perovskite whispering-gallery planar nanolasers,” Nano lett. 14, (10) 5995-6001, 2014.

[81] A. Babayigit, A. Ethirajan, M. Muller and B. Conings, “Toxicity of organometal halide perovskite solar cells,” Nat. mater. 15 (3) 247, 2016.

[82] F. Giustino and H. J. Snaith, “Toward lead-free perovskite solar cells,” ACS Energy Lett. 1, (6), 1233-1240, 2016.

[83] M. Zhang, M. Lyu, P. Chen, M. Hao, J. H. Yun, and L. Wang. "Recent advances in low-toxic lead-free metal halide perovskite materials for solar cell application,” Asia Pac. J. Chem. Eng. 11 (3), 392-398, 2016.

[84] N. K. Noel, S. D. Stranks, A. Abate, C. Wehrenfennig, S. Guarnera, A. A. Haghighirad, A. Sadhanala et al. “Lead-free organic–inorganic tin halide perovskites for photovoltaic applications,” Energ. Environ. Sci. 7 (9) 3061-3068, 2014.

[85] T. Krishnamoorthy, H. Ding, C. Yan, W. L. Leong, T. Baikie, Z. Zhang, M. Sherburne et al. “Lead-free germanium iodide perovskite materials for photovoltaic applications,” J. Mater. Chem. A 3, (47) 23829-23832, 2015.

[86] X. P. Cui, K. J. Jiang, J. H. Huang, Q. Q. Zhang, M. J. Su, L. M. Yang, Y. L. Song, and X. Q. Zhou, “Cupric bromide hybrid perovskite heterojunction solar cells,” Synth. Met, 209, 247-250, 2015.

[87] P. C. Harikesh, H. K. Mulmudi, B. Ghosh, T. W. Goh, Y. T. Teng, K. Thirumal, M. Lockrey et al. “Rb as an alternative cation for templating inorganic lead-free perovskites for solution processed photovoltaics,” Chem. Mater. 28 (20) 7496-7504, 2016.

[88] B. W. Park, B. Philippe, X. Zhang, H. Rensmo, G. Boschloo, and E. M. J. Johansson, “Bismuth based hybrid perovskites A3Bi2I9 (A: methylammonium or cesium) for solar cell application,” Adv. Mater. 27 (43) 6806-6813, 2015.

[89] B. Philippe, B. W. Park, R. Lindblad, J. Oscarsson, S. Ahmadi, E. M. J. Johansson, and H. Rensmo, “Chemical and electronic structure characterization of lead halide perovskites and stability behavior under different exposures a photoelectron spectroscopy investigation,” Chem. Mater. 27, (5), 1720-1731, 2015.

[90] N. Aristidou, S. M. Irene, T. Chotchuangchutchaval, M. Brown, L. Martinez, T. Rath, and S. A. Haque, “The role of oxygen in the degradation of methylammonium lead trihalide perovskite photoactive layers," Angew. Chem. Int. Ed. 54, (28) 8208-8212, 2015.

[91] R. K. Misra, S. Aharon, B. Li, D. Mogilyansky, I. V. Fisher, L. Etgar, and E. A. Katz, "Temperature and component dependent degradation of perovskite

photovoltaic materials under concentrated sunlight," J. Phys. Chem. Lett. 6 (3) 326-330, 2015.

[92] J. H. Noh, S. H. Im, J. H. Heo, T. N. Mandal and S. I. Seok, “Chemical management for colorful, efficient, and stable inorganic–organic hybrid nanostructured solar cells,” Nano Lett. 13, 1764, 2013.

[93] P. Pistor, J. Borchert, W. Fra, R. Csuk and R. Scheer, “Monitoring the phase formation of coevaporated lead halide perovskite thin films by in situ x-ray diffraction,” J. Phys. Chem. Lett. 5, 3308, 2014.

[94] J. W. Lee, D. H. Kim, H. S. Kim, S. W. Seo, S. M. Cho, and N. G. Park, “Formamidinium and cesium hybridization for photo and moisture stable perovskite solar cell,” Adv. Energy Mater 5 (20), 1501310, 2015.

[95] H. Zheng, G. Liu, L. Zhu, J. Ye, X. Zhang, A. Alsaedi, T. Hayat, X. Pan, and S. Dai, “The Effect of Hydrophobicity of Ammonium Salts on Stability of Quasi 2D Perovskite Materials in Moist Condition,” Adv. Energy Mater. 8 b (21), 1800051, 2018.

[96] T. Zhang, M. D. Ibrahim, G. Li, F. Xu, N. Guo, M. Grätzel, and Y Zhao, “Bication lead iodide 2D perovskite component to stabilize inorganic α-CsPbI3 perovskite phase for high-efficiency solar cells,” Sci. Adv. 3, (9) e1700841, 2017.

[97] S. Shao, J. Liu, G. Portale, H. H. Fang, G. R. Blake, H. Gert, T. Brink, L. J. A. Koster, and M. A. Loi, “Highly reproducible Sn-based hybrid perovskite solar cells with 9% efficiency,” Adv Energy Mater. 8 (4), 1702019, 2018.

[98] Z. Wang, Q. Lin, F. P. Chmiel, N. Sakai, L. M. Herz, and H. J. Snaith, “Efficient ambient air stable solar cells with 2D–3D heterostructured

butylammonium-caesium-formamidinium lead halide perovskites," Nat. Energy 2, (9) 17135, 2017.

[99] Z. Wang, D. P. McMeekin, N. Sakai, S. V. Reenen, K. Wojciechowski, J. B. Patel, M. B. Johnston, and H. J. Snaith, "Efficient and air stable mixed cation lead mixed halide perovskite solar cells with n-doped organic electron extraction layers," Adv. Mater. 29, (5) 1604186, 2017.

[100] Z. Li, X. Chuanxiao, Y. Ye, S. P. Harvey, D. H. Kim, J. A. Christians, M. Yang, P. Schulz, S. U. Nanayakkara, C. S. Jiang, J. M. Luther, J. J. Berry, M. C. Beard, M.M. A. Jassim and K. Zhu, "Extrinsic ion migration in perovskite solar cells," Energy Environ. Sci. 10 (5) 1234-1242, 2017.

[101] H. S. Kim, J. W. Lee, N. Yantara, P. P. Boix , S. A. Kulkarni, S. Mhaisalkar, M. Grätzel and N. G. Park, "High efficiency solid-state sensitized solar cell-based on submicrometer rutile TiO2 nanorod and CH3NH3PbI3 perovskite sensitizer," Nano lett. 13 (6), 2412-2417, 2013.

[102] S. S. Mali, H. Kim, J. V. Patil and C. K. Hong, "Bio-inspired carbon hole transporting layer derived from aloe vera plant for cost-effective fully printable mesoscopic carbon perovskite solar cells," ACS Appl. Mater. Interfaces 10 (37) 31280-31290, 2018.

[103] J. M. Frost, K. T. Butler, F. Brivio, C. H. Hendon, M. V. Schilfgaarde and A. Walsh "Atomistic origins of high-performance in hybrid halide perovskite solar cells," Nano lett. 14 (5), 2584-2590, 2014.

[104] C. C. Stoumpos, C. D. Malliakas, and M. G. Kanatzidis, "Semiconducting tin and lead iodide perovskites with organic cations: phase transitions, high mobilities,

and near-infrared photoluminescent properties," Inorg. Chem. 52 (15), 9019-9038, 2013.

[105] R. S. Sanchez, V. G. Pedro, J. W. Lee, N. G. Park, Y. S. Kang, L. M. Sero, and J. Bisquert, "Slow dynamic processes in lead halide perovskite solar cells. characteristic times and hysteresis," J. Phys. Chem. Lett. 5(13), 2357-2363, 2014.

[106] Y. Kutes, L. Ye, Y. Zhou, S. Pang, B. D. Huey and N. P. Padture, N.P, "Direct observation of ferroelectric domains in solution-processed CH3NH3PbI3 perovskite thin films," J. Phys. Chem. Lett. 5 (19) 3335-3339, 2014.

[107] Z. Xiao, Y. Yuan, Y. Shao, Q. Wang, Q. Dong, C. Bi, P. Sharma, A. Gruverman and J. Huang, "Giant switchable photovoltaic effect in organometal trihalide perovskite devices," Nat. Mater. 14 (2) 193, 2015.

[108] D. B. Strukov, G. S. Snider, D. R. Stewart and R. S. Williams, "The missing memristor found," Nature 453 (7191) 80, 2008.

[109] Q. Wang, Y. Shao, Q. Dong, Z. Xiao, Y. Yuan and J. Huang, "Large fill-factor bilayer iodine perovskite solar cells fabricated by a low-temperature solution-process," Energy Environ. Sci. 7 (7) 2359-2365, 2014.

[110] J. B. Edmands, G. E. Eperon, R. D. Johnson, H. J. Snaith, and P. G. Radaelli. "Non-ferroelectric nature of the conductance hysteresis in CH3NH3PbI3 perovskite-based photovoltaic devices," Appl. Phys. Lett. 106 (17) 173502, 2015.

[111] C. Eames, J. M. Frost, P. R. F. Barnes, B. C. O'Regan, A. Walsh and M. S. Islam, "Ionic transport in hybrid lead iodide perovskite solar cells," Nat. Commun. 6, 7497, 2015.

[112] T. Manaka, E. Lim, R. Tamura, and M. Iwamoto, “Direct imaging of carrier motion in organic transistors by optical second-harmonic generation,” Nat. Photonics 1, (10) 581, 2007.

Chapter 2

Experimental methods and theoretical background

2.1 Introduction

To study the fundamental carrier transport properties of lead-based perovskite materials $MAPbI_3$, we choose the directly probing the transient optical signal based on EFISHG and PL technique. Direct observation of carrier injection from the electrode and its transport would be essential for further understanding of the carrier behavior in the perovskite devices [1-3]. According to the many researches related with the lead based perovskite materials, to investigate fundamental carrier transport in organic inorganic hybrid perovskite from a fundamental scientific point of view is essential issue.

Here we employed several techniques to investigate the characteristics of carrier behaviors based on fundamental electrical properties and optical properties. In this chapter, I would like to briefly explain the theoretical background of experimental methods conducted in this study. For a fully understanding the carrier behavior, not only FET characteristics for steady-state but also transient process such as e-TOF, time-dependent PL image, TRMSHG are conducted.

As we all know, the perovskite materials show the multi-photon excited fluorescence, and it may interfere with the weak SHG signal during the SHG measurement. On the other hand, it is known that PL is quenched under the presence of charges owing to the exciton-polaron annihilation [4, 5]. These motivated us to study the carrier transport in the perovskite materials based the real-time transient PL imaging also.

Moreover, in our laboratory, we successfully developed a unique technique to visualize the electric field in the electronic devices on the basis of the electric field induced second harmonic generation (EFISHG) measurement for organic semiconductor [6-8]. Here we introduced this technique to discuss the injected charge and the local electric field in the perovskite-based devices, through visualization of the carrier transport and polarization structure in perovskite layer. In addition, to access the electrical properties such as charge carrier mobilities, the fundamental FET characteristics and the time-of-flight technique (TOF) are carried out. From the correlation between time-of-flight and transient photoluminescence (PL) imaging, hole transport phenomena and migration of ions can be successfully discriminated. With this chapter, the relevant principles and experimental approach of each method are discussed. Before the description of experimental methods and theoretical background, I would like to describe the device fabrication used in this study.

2.2 Device Fabrication

2.2.1 Substrates for sample preparation

For the substrates, we used two types for substrates for two different measurements. To find out the optical properties of the perovskite materials, surface cell structure with glass substrates were used, and FET structure with heavily p-doped Si substrates with a 500 nm thick oxide (SiO_2) were used for visualization of transient carrier transport. The side view of two kinds of devices is shown in Fig. 2.1 (a) and (b). The device were prepared as follows.

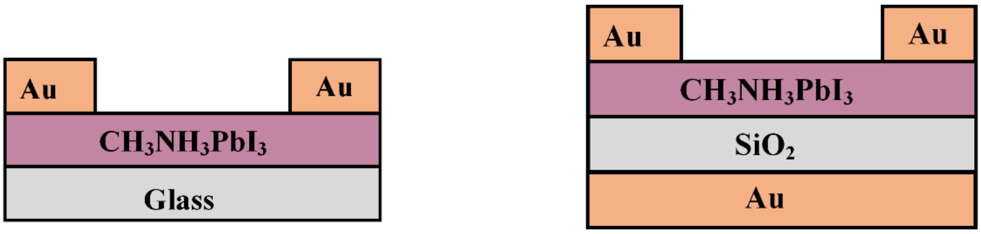

Figure 2.1: Perovskite structure (a) on the glass substrate and (b) silicon substrate

2.2.2 Perovskite thin film preparation

Firstly, glass substrates (1 cm x 1 cm) and silicon substrates (2 cm x 2 cm) were cleaned by ultrasonic cleaner in ethanol, acetone, and distilled water, successively for 30 min. After drying with N_2 blow, the substrates were further treated with oxygen plasma for 15 min to improve wetting of the surface to obtain homogeneous perovskite thin film. Firstly, the bottom gate electrode was deposited by thermal evaporation for top contact FET transistor. Perovskite thin film can be fabricated on many ways as described in section 1.5, among those perovskite films were deposited by using simple deposition method solution processing, the one-step and two-step simple spin coating process as described in this section.

2.2.3 One step solution deposition

For one-step preparation method, to obtain the $CH_3NH_3PbI_3$ precursor solution, CH_3NH_3I ammonium salt and lead halide PbI_2 were dissolved in 40 wt % of anhydrous N, N- dimethylformamide (DMF) and kept in strong stirring at 70 °C for 12 hours for totally dissolving. A small amount of 100 µl of solution was dropped on the substrate which was fixed on the spin-coater, and then the substrate was rotated with 3000 rpm for 60 s in order to spread the solution by centrifugal force to form a thin film. After 30 s from the spin coating starts, 100 µl anhydrous toluene was dropped onto the spinning film to control the crystallization of the film [9]. After spin coating, the fresh $CH_3NH_3PbI_3$ films were annealed using hot plate at 100 ^{o} C for 15 min in the glove box.

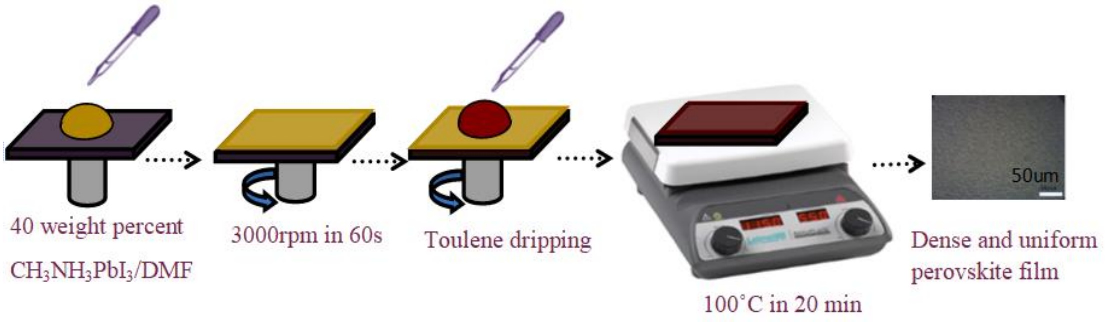

Figure 2.2: One-step spin coating process for perovskite thin film

The one-step solution process easily causes uncontrollable precipitation of perovskite and leads to large morphological variations [10]. In order to get better control for crystallinity and homogeneous morphology, which was better for transport quality, later, a two-step method was used.

2.2.4 Two-step solution deposition

For two-step solution deposition, PbI_2 film should be deposited first on the substrates, and then perovskite layer crystallizes by spin coating CH_3NH_3I solution. The detailed procedure for two-step solution method is following.

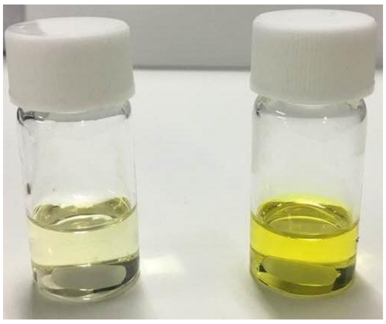

Figure 2.3: White solution for the MAI with 2-propanal and yellow for PbI_2 with DMF solution for two step spin coating.

Before the spin-coating procedure, PbI_2 was dissolved in anhydrous N, N-dimethylformamide (DMF) with a concentration of 600 mg/ml and ammonium salts (CH_3NH_3I) were dissolved in anhydrous 2-propanol with a concentration of 65 mg/ml. Both of the two solutions were kept in strong stirring at 70 °C for 12 hours.

For the two-step method, PbI_2 layer was first deposited on the cleaned SiO_2 substrate by spin-coating with 2000 rpm for 30 s to get a uniform film, followed by drying on the hot plate at 100 °C for 10 min. Then the methylammonium iodide (CH_3NH_3I) layer was deposited on dried PbI_2 film by spin-coating with 2000 rpm for 30 s. Annealing at 100 °C for 15 min was necessary to get perovskite crystal [11]. The color-changing from light yellow to dark brown indicates a perovskite film was completely generated

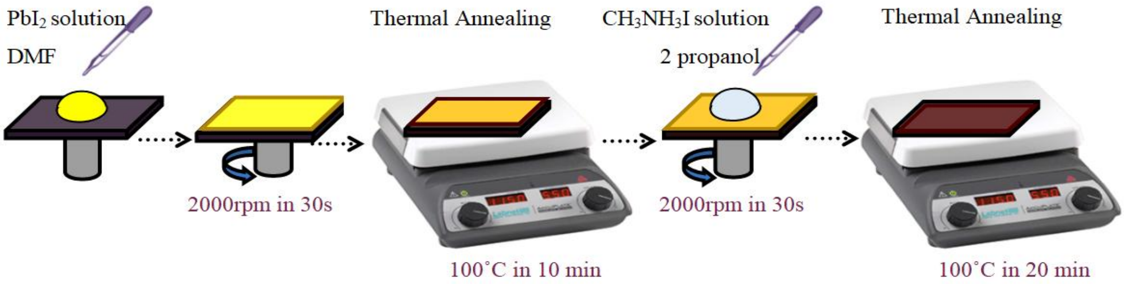

Figure 2.4: Two-step spin-coating process for perovskite thin film.

Finally, 100 nm thick gold were vacuum-deposited to form source and drain electrodes on the top of the perovskite layer through a shadow mask by thermal evaporation. For FET devices, the channel width (W) of all the devices was same about 3 mm, but the length (L) was 30 μm to 100 μm respectively. The fabricated perovskite substrates were kept in a desiccator at room temperature before measurement.

2.3 Characterization of the spin-coated thin film

Organo metal halide perovskite ($CH_3NH_3PbI_3$) is formed by the reaction of metal halides (PbI_2) and organic molecules (CH_3NH_3I).

$$PbI_2 + CH_3NH_3I \longrightarrow CH_3NH_3PbI_3 \tag{2.1}$$

After the first step, the color was yellow caused by PbI_2, with the absorption band edge around (530 nm). After the reaction with CH_3NH_3I the color changed to little brown then after small crystallization of perovskite following by annealing, it completely changed to dark brown, and the absorption edge moved to 780 nm (1.56 eV).

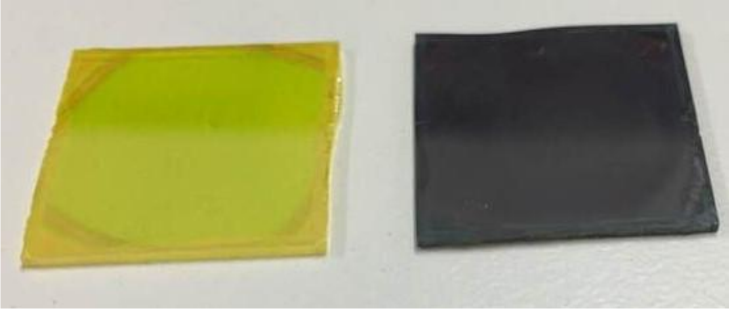

Figure 2.5: The PbI_2 and $MAPbI_2$ thin film morphology on the glass substrate.

2.3.1 Absorption spectroscopy measurement

The absorption spectrum is used to understand the absorbance process, the interaction between electromagnetic waves and materials. Absorbing light is a primary property of semiconductor material. In principle, we can get the bandgap and the molecular structure information from the absorption spectra. The measurement is based with Lambert-Beer Law.

$$A=\varepsilon lc, \tag{2.2}$$

which A is the absorbance, ε is the attenuation coefficient of the material, l is the distance of the light travels through the material and c is the concentration of the materials [12].

To measure the absorbance spectrum of the organic-inorganic hybrid halide pervoskite thin film, we prepared $CH_3NH_3PbI_3$ films on the glass substrate. After cleaning the glass substrate with acetone, distilled water successively in the ultrasonic bath for 30 min, then fabricated the perovskite thin film on the glass by one-step, two-step method. The sample absorbance property was characterized with reference of a clear glass substrate. The absorbance spectra of the perovskite films were measured with a UV/ VIS/ NIR spectrometer (JASCO, V-570).

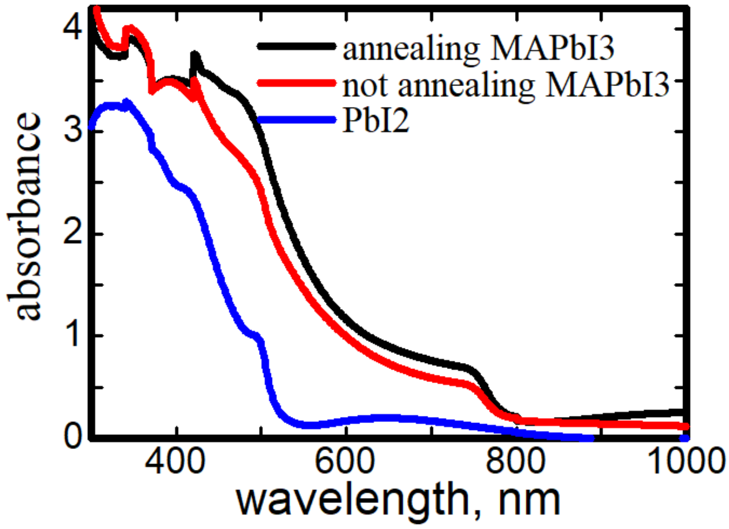

Figure 2.6: Absorbance spectrum for PbI_2 and $MAPbI_2$ film annealing and not annealing after reaction with MAI salt.

Figure 2.6 depicts the absorbance spectrum for the two-step solution process of PbI_2 and $MAPbI_2$ before and after annealing. According to the absorbance result, we found the same band edge for both cases of with and without annealing. It revealed that it could be possible the slow-growing process for perovskite crystal after taking the reaction with PbI_2 and MAI solution without annealing. However, all films used in this study were carried by 15 min annealing processes. The strong and broad absorption in the ultraviolet and visible light range of two-step fabricated film, revealed that this kind of perovskite layer was a good light absorber. The band edge of both solution processed for $CH_3NH_3PbI_3$ film indicated that the absorption edge was 780 nm. So we can conclude that the optical band gap of our fabricated $CH_3NH_3PbI_3$ films was 1.59 eV which was consistent with the other groups' results [13].

2.3.2 Photoluminescence spectroscopic spectrum

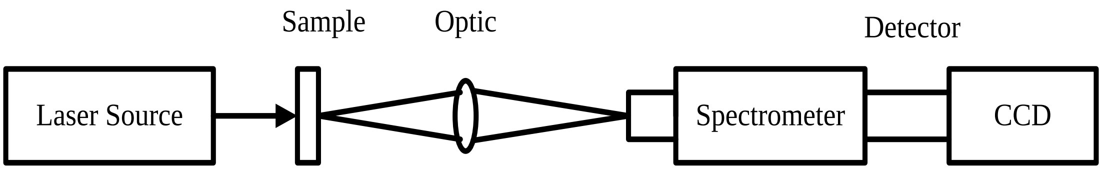

Figure 2.7: Schematic diagram of the photoluminescence setup [14].

The photoluminescence is a phenomenon to show the emission spectrum when the materials transit from high energy state to lower energy state emitting photons. The laser light is impinged by means of an optical system that allows focusing on the sample used in the study. When the electron-hole pair recombined between the excited state and the ground state after excited, photons would be emitted from the sample. The photoluminescence was collected by an appropriate optical configuration and acquired by the detection system [14].

In the photoluminescence spectroscopic experiment, the set-up is a custom-made system. In our laboratory Ti: Sapphire laser is used as the excitation source for the photoluminescence setup. The detection system is simple and composed of a grating spectrometer (SR-163 series, 600 g/mm grating) to cooled charge-coupled device (CCD) camera (Andor technology).

2.3.3 X- ray diffraction measurement

X-ray diffraction is a technique used for identifying the structure of a crystal, in which the crystal atoms cause a beam of incident X-rays to diffract into specific directions. By measuring the angles and intensities of these diffracted beams, a crystallographer can produce a three-dimensional picture of atoms within the crystal, determining the mean positions of the atoms, as well as their chemical bonds, their disorder and various other pieces of information [16]. With a steady X-ray source, diffraction can be determined by Bragg's law.

$$2\mathrm{d}\sin\theta = n\lambda. \tag{2.3}$$

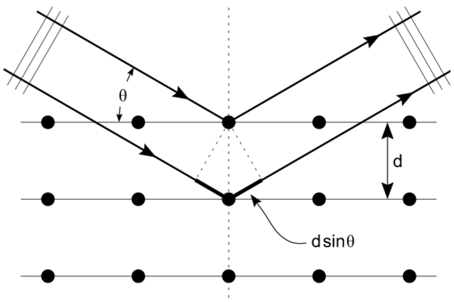

Figure 2.8: The X-ray diffraction scheme [15]

As the Figure 2.8 shows, d is the spacing between diffracting planes, θ is the incident angle, n is any integer, and λ is the wavelength of the beam. These specific directions appear as spots on the diffraction pattern called reflections. Thus, X-ray diffraction results from an electromagnetic wave impinging on a regular array of scatters (the repeating arrangement of atoms within the crystal). The organometal halide perovskite has an ABX_3 structure [16]. Figure 2.9 shows that in the center of crystal unit is an ammonium cation; the Pb cations locate around the organic group and form a cube structure; the halide anions are located between the Pb cations and form an octahedral with the Pb in the center [17, 18].

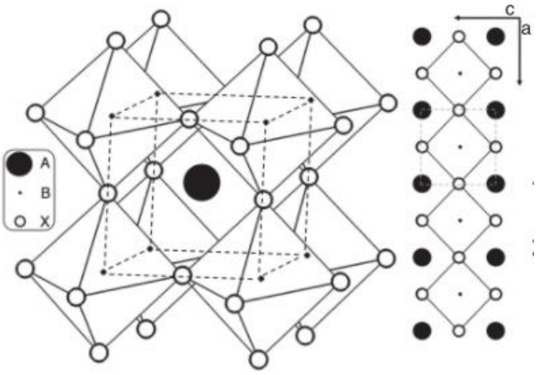

Figure 2.9: Left: Three-dimensional schematic representation of perovskite structure ABX_3 (A = CH_3NH_3 4 +, B = Pb 2+, and X = Cl, Br, I). Right: Two-dimensional schematic illustrating the perovskite unit cell [16].

From now on, the framework and methodologies used to obtain the electrical and optical parameters are described.

2.4 FET measurement

FET measurement is one of the standard technologies to characterize the mechanisms of charge injection and transport in organic semiconductors. The optimal performance of the field-effect transistors critically depends on the nature of charge injection from the source electrode followed by transport through the channel and collection at the drain. In the case where the injected charge dramatically changes the electric field configuration in the polymer (i.e., effectively screens the source-drain field), the transport becomes space-charge limited [19].

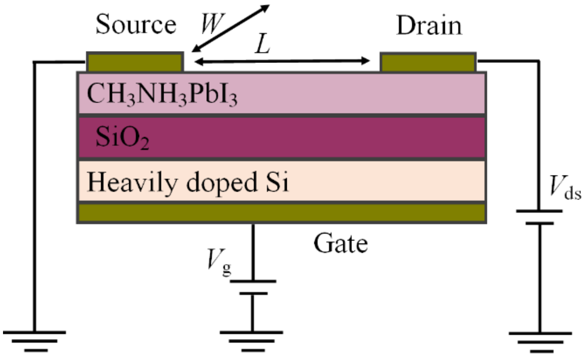

Figure 2.10: Schematic diagram of a FET measurement

A field-effect transistor requires the thin semiconducting layer, which is separated from gate electrode by insulating gate dielectric, source and drain electrodes these are in contact with semiconducting layer by channel width W and channel length L. For normal FET measurement, the potential difference between the source and the gate is usually called the gate voltage (V_g), while the potential difference between the source and drain is referred as source-drain voltage (V_d). The source electrode is normally grounded ($V_s = 0$).

Fig. 2.10 shows a schematic view of a transistor. By controlling the voltage on one electrode (the gate), charges can be induced at the interface between semiconductor layer and insulator. These charges are injected from the source electrode and collected across the conducting channel at the drain by applying a voltage between the drain and source electrode [21]. The needle probes were used to apply voltage and measure the current. The basic behaviors of the current-voltage characteristics can be derived as follows.

2.4.1 Current-Voltage characteristics of FETs

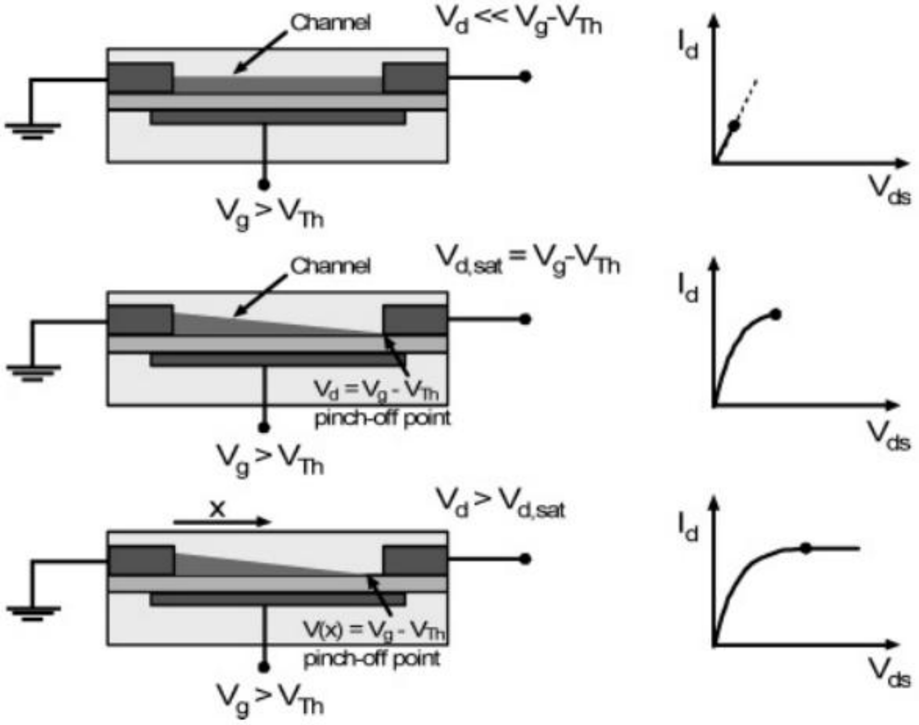

Figure 2.11: Illustraions of operation regimes of FET (a) linear regime; (b) start saturation regime at Pinch-off region; (c) saturation regime and corresponding current-voltage charrcteristics [21].

Figure 2.11 illustrates the basic operating regimes and associated current-voltage characteristic of a field-effect transistor. Firstly, let us assume for the metal-insulator-semiconductor) diode (MIS) structure, if there is no potential difference between the source and drain electrode, and only with a voltage V_g. For that case, a positive gate voltage will induce negative charges at the interface. For a negative gate voltage will induce positive charges at the interface. The number of accumulated charges is proportional to V_g and the capacitance C_i of the insulator. However, all induced charges cannot mobile if there are deep traps at the interface. Deep traps first have to be filled then induced accumulated charges can be mobile, that will contribute the transistor current.

For Fig. 2.11 (a) when no source-drain bias is applied, the charge carrier concentration in the channel is uniform. Until $V_{ds} << (V_g - V_{th})$ this is the linear regime and the current flowing through the channel is directly proportional to V_{ds} and V_{th} is known as the threshold voltage.

When the source-drain voltage is further increased, $V_{ds} = V_g - V_{th}$ is reached at which the channel is pinched off. As shown in Fig. 2.11 (b) that means a depletion region forms near to the drain electrode because the difference between the local channel potential V_x and the gate voltage is now below the V_{th}. A space-charge limited saturation current $I_{ds, sat}$ can start flow.

For further increasing the source-drain voltage will no substantially increase the current but leads to an expansion of the depletion region, as shown in Fig. 2.11 (c) and become slightly shortening the channel, the current saturates at a level $I_{ds\ sat}$.

For those cases, the transistors with short channel lengths require thin gate dielectrics, typically $L > 10d_{(dielectric)}$ to ensure that the field created by gate voltage determine the charge distribution with the channel and is not dominated by lateral field due to the source-drain voltage. Otherwise, a space-charge limited bulk current will prevent saturation, and the gate voltage will not determine the on or off state of the transistor satisfactory [21].

2.4.2 Carrier mobility by FET measurement

The current-voltage characteristics in different operating regimes for FETs can be described analytically assuming the gradual channel approximation. When the gate voltage is higher than the threshold voltage V_{th}, the induced charged Q_{mob} per unit area at the source contact are related to V_g as follows.

$$Q_{mob} = C_i \left(V_g - V_{th} \right), \tag{2.4}$$

where C_i is the capacitance per unit area of the gate dielectric. In Eq. (2.4) the induced charge density depends on the position along the channel, which is accounted for the following equation;

$$Q_{mob} = C_i \left(V_g - V_{th} - V(x) \right). \tag{2.5}$$

Neglecting diffusion, the source-drain current (I_d) induced by carriers is

$$I_d = W \mu Q_{mob} E_x, \tag{2.6}$$

where W is the channel width, μ is the charge mobility, and E_x is the electric field at x. By substituting $E_x = dV / dx$ and Eq. (2.5) into Eq. (2.6), we can obtain,

$$I_d dx = W\mu C_i \left(V_g - V_{th} - V(x)\right) dV. \tag{2.7}$$

The gradual channel expression for the drain current can be obtained by integration of the current increment from $x = 0$ to L, that is from $V_{(x)} = 0$ to V_{ds}, assuming that the mobility is independent of the carrier density and the gate voltage. The drain current is expressed as,

$$I_d = \frac{W}{L}\mu C_i \left[\left(\left(V_g - V_{th}\right) V_d - \frac{1}{2}{V_{ds}}^2\right)\right]. \tag{2.8}$$

In the linear regime with $V_{ds} << V_g$, this can be simplified to

$$I_d = \frac{W}{L}\mu_{linear}\, C_i\left[\left(V_g - V_{th}\right) V_{ds})\right]. \tag{2.9}$$

The drain current is directly proportional to V_g and the field-effect mobility in the linear regime (μ_{linear}) can be extracted from the gradient of I_d versus V_g at constant V_{ds}.

$$\mu_{linear} = \frac{\partial I_{ds}}{\partial V_g}\frac{L}{W C_i V_{ds}}\,. \tag{2.10}$$

For this equation, the channel is pinched off when $V_{ds} = V_g - V_{th}$. When the current saturates ($I_{d\ sat}$) Eq. (2.8) is no longer valid. For this saturation region, the saturation current can be obtained by substituting V_{ds} with $V_g - V_{th}$, yielding

$$I_d = \frac{W}{2L}\mu_{sat}\, C_i\left[\left(\left(V_g - V_{th}\right)^2\right)\right]. \tag{2.11}$$

In the saturation regime, the square root of the saturation current is directly proportional to the gate voltage. This equation assumes that the mobility is gate voltage-independent and the saturated mobility μ_{sat} can be extracted using

$$\mu_{sat}\left(V_g\right) = \frac{\partial I_{ds(sat)}}{\partial V_g}\frac{L}{W C_i}\frac{1}{(V_g - V_{th})}. \tag{2.12}$$

Another important parameter of FETs is on /off ratio, which is the ratio of the drain current in on-state at a particular gate voltage and drain current in the off-state (I_{on}/I_{off}). It determines the switching behavior of the transistor. The on-current depends on the mobility of the semiconductor and the capacitance of the gate dielectric. The magnitude of off-current is determined by gate leakage, especially for low-quality gate insulator and semiconductor layer, by the conduction pathways at the substrate interface [22-24].

2.5 Time-of-Flight (e-TOF)

2.5.1 Conventional TOF

Time of flight was described by Haynes and Shockeley [25] and Lawrence and Gibson [26]. TOF was mainly used to study the transport motilities of organic semiconductors and polymers [27-29]. The schematic diagram of TOF is illustrated in Fig. 2.12. A sample with thickness d is sandwiched between two planner metal electrodes. The top electrode should be semitransparent and non-injecting or blocking electrode for the carrier transported across the sample. When a pulsed laser beam was illuminated onto the carrier generating layer, through the transparent electrode. The photo carriers should be generated with a short flash of laser pulse absorbed in a thickness δ, with $\delta << d$. The light pulse duration t should be short, i.e., $t_{\text{pulse}} << t_{tr}$ (transit time) compared to the charge carrier transit time. The photo carriers drifted across the organic layer under the influence of the electric field between the two electrodes. The two electrodes are connected to an external circuit via a resistor with resistance R and the voltage source with potential V. This external resistor converts the time-dependent photocurrent into a voltage displayed by an oscilloscope [30].

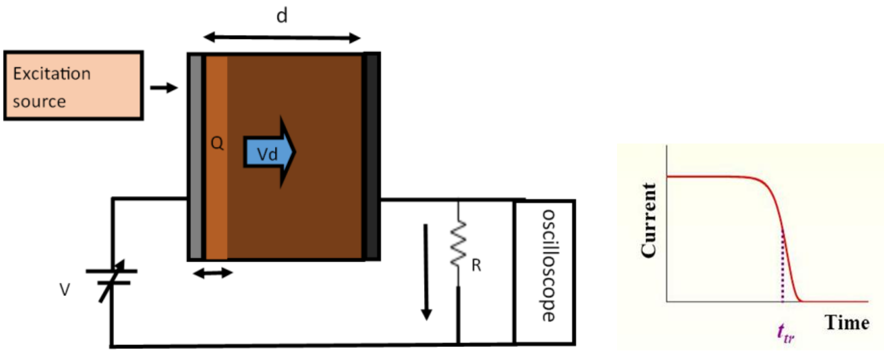

Figure 2.12: Schematics diagram of the conventional time of flight technique [30].

The time taken by the charge carriers to move across the organic layer was determined by monitoring the photocurrent flowing through the external circuit. This transient photocurrent is recorded with a high resolution digital oscilloscope. Drift carrier mobility can be estimated by the photoexcited carriers created at on electrode to reach the opposite electrode. With known applied electric field E and thickness d of the organic layers, the carrier mobility μ can be determined by the following equation. [30]

$$\mu = \frac{d^2}{V\, t_{tr}}\,. \tag{2.13}$$

By switching the polarity of the applied voltage source, one can selectively measure either hole or electron mobility [30].

There are three conditions for conventional TOF methods. The first condition for conventional TOF methods is the amount of charge generated should be small enough so that space charge effects do not change the internal field distribution significantly. This will be true as long as the injected charge Q satisfies, with the sample capacitance C.

$$Q << CV. \tag{2.14}$$

The second condition for conventional TOF is that the time constant of the circuit $t_{tr} = RC$ should be much smaller than the average drifting time of the charges.

$$t << t_{tr} \tag{2.15}$$

A small value of t_{tr} can be realized by choosing small R or C. To be small capacitance, the thickness is important. As capacitance is proportional to sample area and inversely proportional to sample thickness. Small capacitance can be realized with higher thickness and smaller cross section [29].

The third condition requires that the dielectric relaxation time $t_{relaxation}$ be long compared to the transit time to prevent the generated free charge carriers recombination before they reach the other side

$$t_{tr} << t_{relaxation} \tag{2.16}$$

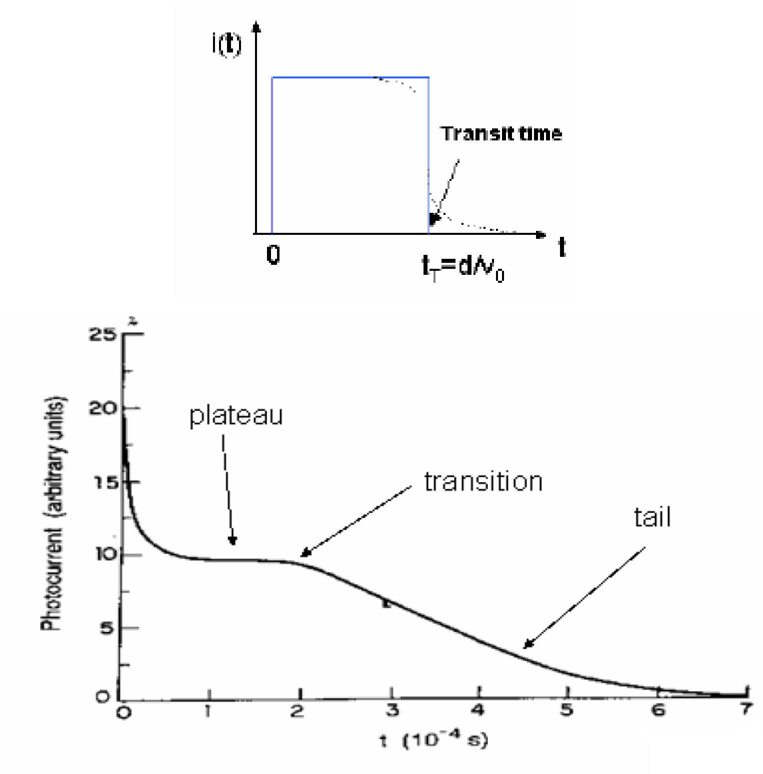

Figure 2.13: (top) Ideal photocurrent with tail due to circuit reaction time (bottom) measured photocurrent with long tail [31].

Regarding to the transit time, for an ideal case, when all charges propagate like a sheet, the photocurrent should display a rectangle shape if there is negletable circuit transit time as shown in Figure. However, if there is existence of traps, the measured tail can be longer than an exponential decay. Because traps act the localized state for carriers, when the trap density is not high, the majority of charges will drift along the plane. Figure 2.13 (b) is the measured photocurrent with plateau and tail of a real material [30]. The transit time can be estimated the intersection point of plateau and tailing edge.

For the time of flight, even though conventional time of flight has a long history and it is applicable for the vertical carrier transport. Here, lateral time of flight are introduced to directly investigate the lateral carrier transport in the FET [31].
From lateral TOF technique, lateral drift mobility has been estimated from the measured transient photocurrent.

2.5.2 Lateral TOF method

2.5.2.1 Experimental setup for lateral TOF

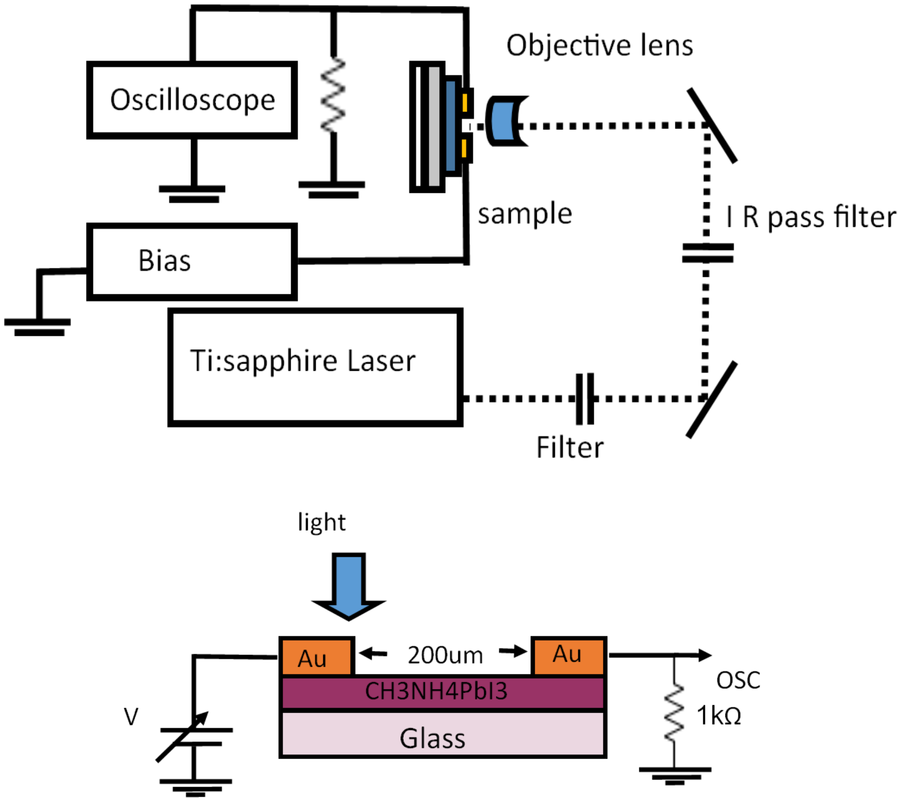

Figure 2.14: (upper) Schematic diagram of lateral TOF experimental setup (lower) lateral TOF electrical connection.

Fig. 2.14 shows the schematic of the lateral TOF measurement system. The measurement was carried out with Nd; YAG Minilite laser with the wavelength of 532 nm to produce charges in a thin layer at near one electrode with a pulse width of 10 ns. Under the electric field supplied by the external voltage source (keithley 2400), single sign of charges extract to near electrode, and the alternate sign of charges moves through the channel length. A digital oscilloscope (70 MHz) was used to measure the voltage change of the (1 kΩ, 10 kΩ) resistor in the circuit. The measurement was carried out under an electric field range of 10 kV/cm.

At normal, the photocurrent of the active layer displays a plateau and then decreases at the transit time. Measurement of the transient photocurrent *i(t)* display anomalous transport properties. The long tail of *i(t)* indicates dispersion of carrier transit times [31]. However, in the presence of strong trapping effects, the interpretation of experimental results becomes difficult.

2.6 Charge carrier accumulation models

For evaluation of the charge carrier accumulation and transport in the channel, the Maxwell-Wagner (MW) model and transmission line approximation model can be used. The MW model is a well-known mathematical model for charge accumulation on the interface related to the microscopic electrical properties of materials. [32] Transmission line approximation is related to signal propagation analysis based on equivalent circuits. Both models are available to explain the charge propagation in two and three electrodes represented by metal-insulator metal and FET structures. Here, I would like to conduct more detail in the transmission line approximation model.

2.6.1 Transmission line approximation model

The transmission line approximation can model the charge propagation across the channel for two electrodes system even though conductivity distribution changes with time. For the propagation of charges in the system of two electrodes was successfully modeled by the equivalent circuit with distributed parameters [33] where the accumulated charge propagated along the channel can be shown consisting of infinitely resistors and capacitors connected in series as a ladder as shown in Fig. 2.15.

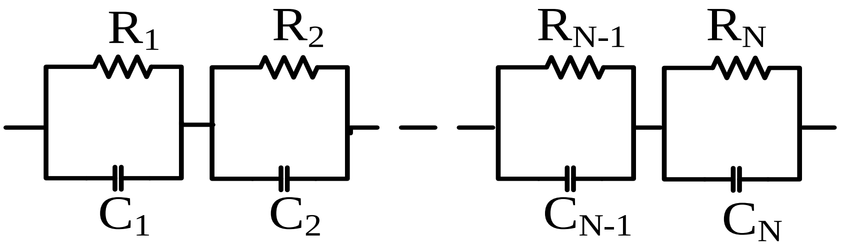

(a)

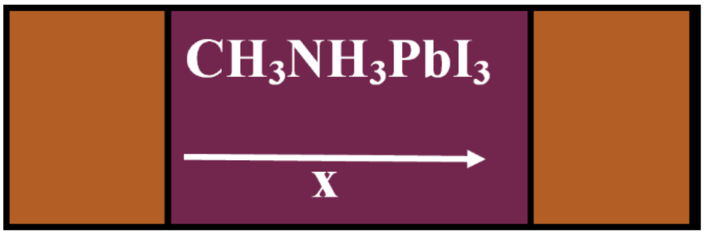

(b)

Figure 2.15: (a) MIM equivalent circuit with distribute parameters and (b) sketch of a perovskite MIM structure [33].

In this model the charge is propagating from one electrode to the opposite one situated in distance d through the infinitely resistor and charge carrier distribution is depicted by the capacitors C. It is assumed, no electric field inside metal electrode ($C_{\mathrm{metal}} = 0$) and metal resistance ($R_{\mathrm{metal}} = 0$). The distributed conductance σ can be estimated from the equation of differentiation of the current density with respect to E defined as

$$\sigma = \frac{\partial J}{\partial E}\,, \tag{2.16}$$

using e and n for the elementary charges and carrier density, the current density of carrier transport can be described as follows.

$$J = en\mu E \;\; = \frac{CV}{d}\mu\frac{V}{d}\,. \tag{2.17}$$

Here, it is assumed that there is no effect of space charge field and the electric field across the MIM structure is constant, $E = \frac{V}{d}$

Subsequently, the distributed resistance R is extracted from Eq. 2.17 as

$$R = \frac{d^2}{C\mu V}\,. \tag{2.18}$$

If a voltage pulse with an amplitude V is applied to the electrodes the transit time can be estimated by the relation $t_{\mathrm{tr}} = RC$ and therefore,

$$t_{tr} = \frac{d^2}{\mu V}\,. \tag{2.19}$$

Here the product of *RC* is the relaxation of the injected carrier with $R=\sum R_i$ and $C=\sum C_i$ and represents the carrier transport time across all *RC* segments illustrated as Fig. 2.15 (a).

2.6.2 Interface charge propagation model

The propagation of charges in the system of three electrodes was successfully modeled by the equivalent circuit with distributed parameters[33], where the accumulated charge propagated along the channel can be shown consisting of infinitely resistors and capacitors connected in series as a ladder, as shown in Fig. 2.16.

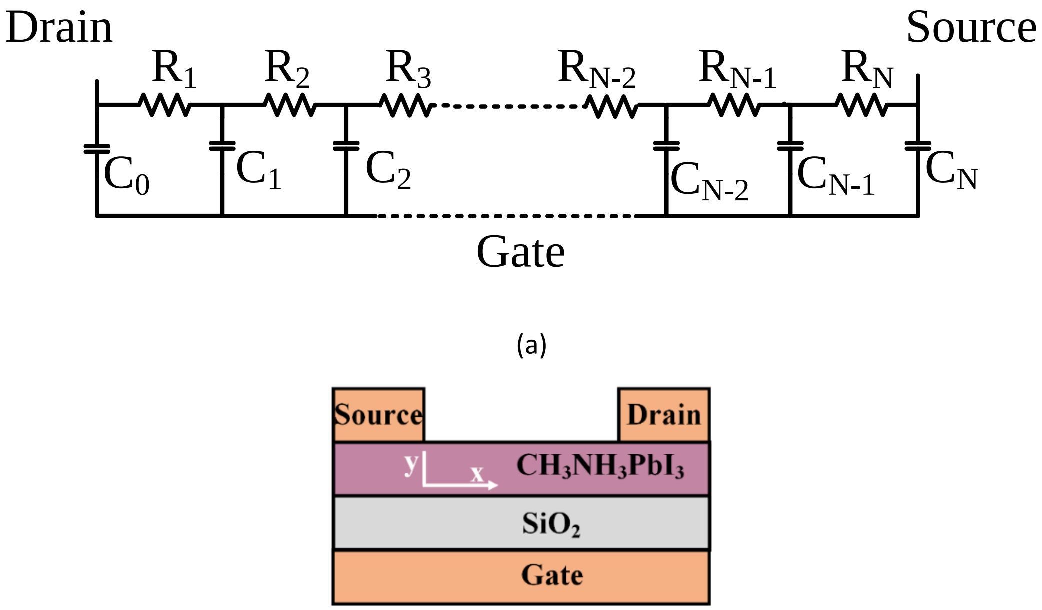

(a)

(b)

Figure 2.16: (a) FET equivalent circuit with distributing parameters and (b) sketch of a perovskite FET structure [33].

For interface charge propagation model, we have to assume charges are propagating through the channel at the interface and the driving force is cause by potential difference between the source and gate electrodes, the accumulated interface charge transit along the channel on charging the gate capacitor.

The accumulated charge can be calculated from the Eq. (2.20).

$$q_s(x) = C\partial V(x)dx. \tag{2.20}$$

The time for charge transport can be derived as a product of channel resistance R_{ch} and capacitance C_{ch} as follows.

$$t_r = R_{ch}C_{ch}. \tag{2.21}$$

The drain-source current I_{ds} can be expressed from the characteristic equation of FET structure as described in Eq. (2.8),

$$I_{ds} = C_g \frac{W}{L} \mu (V_{gs} - V_{th} - \frac{1}{2} V_{ds}) V_{ds} \; . \tag{2.22}$$

where C_{g} is the gate insulator capacitance per unit area, $\frac{W}{L}$ is the channel width/length and $V_{gs} - V_{th}$ is the applied gate-source voltage V_{gs}, reduced by the threshold voltage, V_{th}. Then for a linear approximation, R_{ch} (x) can be derived as follows.

$$R_{ch}(x) = \frac{V_{ds}}{I_{ds}} = \frac{x}{C_g W \mu (V_{gs} - V_{th} - \frac{1}{2} V_{ds})} \; . \tag{2.23}$$

For the channel capacitance,

$$C_{ch} = C_g LW. \tag{2.24}$$

where L and W represent channel area. The transit time can be evaluated as a product of Eq. (2.23) and Eq. (2.24) in the form as follows.

$$t_{tr} = \frac{1}{L} \int_0^L R_{ch} C_{ch} dx = \frac{1}{2} \frac{L^2}{\mu (V_{gs} - V_{th} - \frac{1}{2} V_{ds})} \; . \tag{2.25}$$

$$V = \mu E = \mu \frac{V_{ds}}{L} \; . \tag{2.26}$$

$$t_{tr} = \frac{1}{2\mu} \frac{L^2}{V}. \tag{2.27}$$

After calculation, we can see the carrier motion varies the square root transit time means that diffusion like carrier transport dominated the carrier transfer for both FET and MIM structure while as it differs by factor ½ only.

2.7 Spectroscopic methods

Any luminescence spectroscopic measurement consists of the same experimental setup as shown in Fig. 2.18. Light from the excitation source is direct to the sample using suitable optics. The generated light from the sample is collected again by suitable optics and recorded by a detector. If one is interested in the spectrum, the emitted light needs to be dispersed by placing a monochromator or spectrograph in front of detectors. If one is interested in lifetime of the emitting state, a light pulse is used to excite the sample, and the emitted light intensity is recorded as a function of time. Here we emphasized the visualization process, especially PL and EFISHG measurement, therefore, the emitted signal is captured by a cooled charge-coupled device (CCD) camera directly [34].

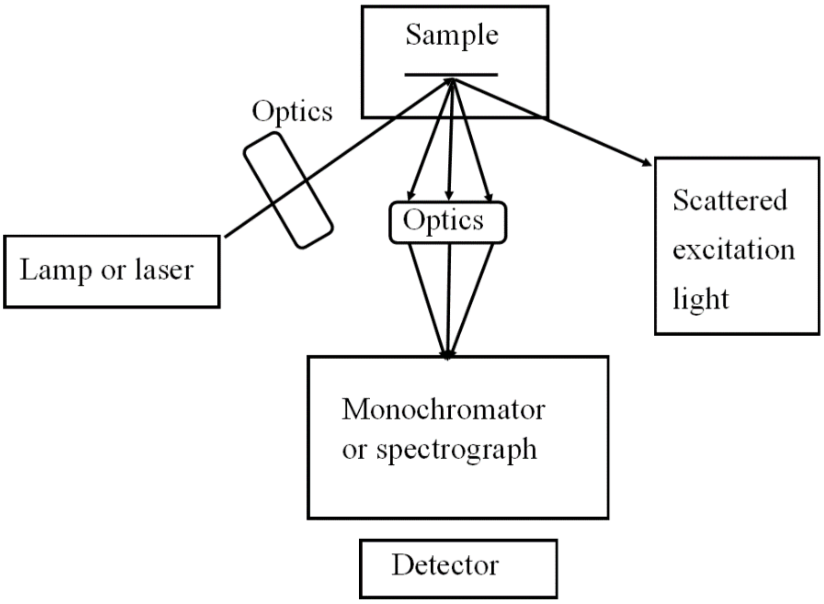

Figure 2.18: Experiment setup for spectroscopic methods [34]

2.7.1 PL quenching measurement

For organic fluorescent material, PL decay imaging method is a fast and easy way to study the carrier transport and charge separation. When light is irradiated, semiconducting materials absorb photons, electronic excitations occur, and then these excitations return to the ground state. Outcoming radiative relaxations is called photoluminescence. Photoluminescence (PL) which provides several pieces of information including bandgap and charge separation [34].

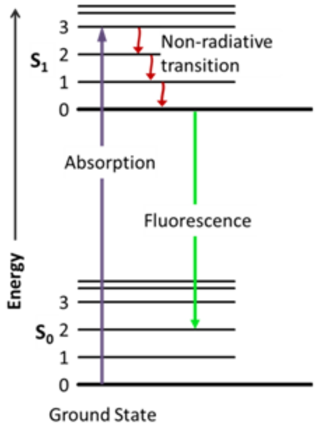

Figure 2.19: Photoluminescence phenomenon [34]

PL decay imaging is a method of visualizing carrier transport by utilizing attenuation of light emission intensity. For carrier visualization by PL decay image, consider about the molecule initially occupies at its ground state. After light is irradiated, it changes to excited state, and photoluminescence is generated. But according to the forester model, if there is charged ions inside of material, energy transfer takes place from ground state molecule to the charged molecule that cause the PL intensity decrease. That is PL quenching. PL intensity will be decreased compared to the isolated state due to charge separation by electron or hole injection. From the change in PL intensity, we can evaluate the mobility and effectiveness of charge separation, which is come from interface charged propagation model described as previous section.

2.7.2 Experimental set up of PL imaging measurement

Figure 2.20 shows the setting of the experiment in the fluorescence decay method. Blue LED light with a wavelength of 465 nm was used as the excitation source. A voltage of +100V and -100V was applied to the top electrode with respect to the gate electrode. When the voltage was applied, the carrier was injected and time-dependent fluorescence intensity by the injection of electrons and holes was recorded by CCD camera as shown in Fig. 2.20. For more details, see subsection 4.6.

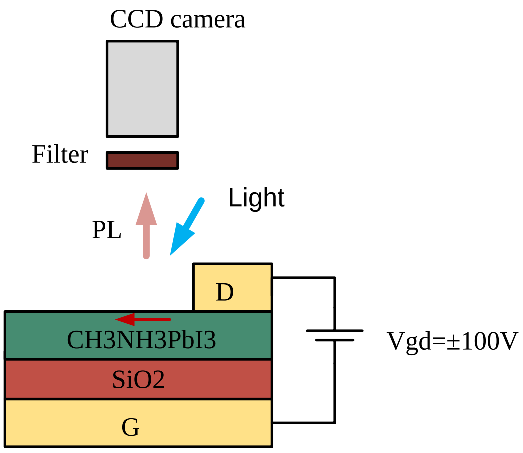

Figure 2.20: Experiment of PL decay imaging.

2.7.3 Electric field induced second harmonic generation (EFISHG)

SHG is one of the nonlinear optical phenomena. When the fundamental light irradiates the material, nonlinear polarization is induced, and the second harmonic light of the incident light is generated from the materials. If the molecule has inversion symmetry, SHG signal cannot come out. However, under the electric field, we can observe the SHG signal from the material with inversion symmetry and called EFISHG.

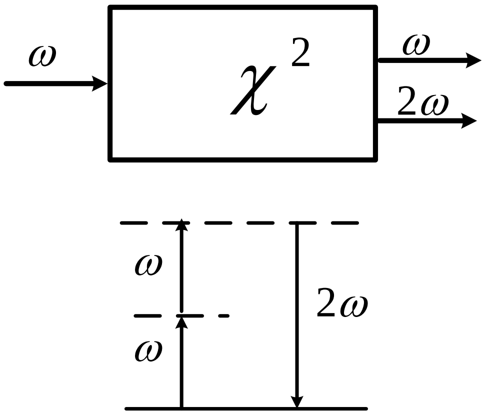

Figure 2.21: (top) geometry of second harmonic generation (bottom) Energy-level diagram for second-harmonic generation.

Figure 2.21 shows the schematic image of the SHG diagram from nonlinear optical media [35], when the fundamental light ω is incident to the nonlinear optical material, the transmitted light consists of not only the incident fundamental light ω but also frequency doubled light SHG (2ω) comes out under the presence of electric field. The applied electric field induces the effective polarization in materials, and the SHG intensity can be described as

$$I(2\omega) \propto \left|\overleftrightarrow{\chi}^{(3)}(2\omega; 0, \omega, \omega) \vdots \vec{E}(0)\vec{E}(\omega)\vec{E}(\omega)\right|.^2 \qquad (2.28)$$

Here $\overleftrightarrow{\chi}^{(3)}(2\omega; 0, \omega, \omega)$ is the 3rd order nonlinear susceptibility tensor of material and depends on ω, $\bar{E}(\omega)$ is the electric field of a pulsed laser. $\bar{E}(0)$ is a static electric field, which consists of an external electric field $\overline{E_{ext}}(0)$ and a space charge field $\overline{E_{sc}}(0)$ which is described as

$$\vec{E}(0) = \vec{E}_{\text{ext}} + \vec{E}_{\text{sc}} \ . \qquad (2.29)$$

Consequently, the SH light intensity is given as $I(2\omega) \propto \left|\vec{E}(0)\right|^2$. That is the SH light intensity $I(2\omega)$ is in proportion to the square of the static electric field $\bar{E}(0)$. According to the Gauss Law, the charge is the source of the electric field. As shown in Fig. 2.22, if we can get the information of the electric field by analyzing the SHG signal, we can directly observe the carrier from the CCD camera.

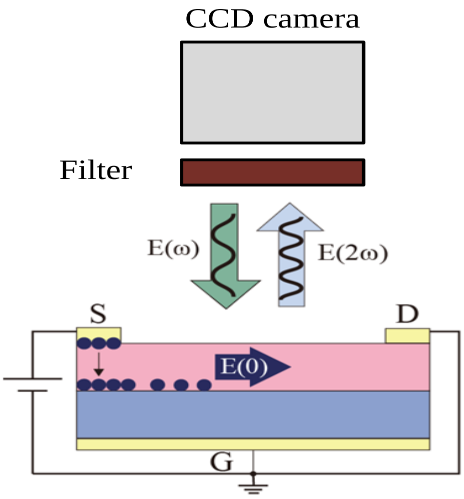

Figure 2.22: Visualization of carrier by EFISHG.

Ideally, SH signal can be detected for all of the materials if the source intensity is high enough when these materials are optically nonlinear. The advantages of nonlinear optical methods are 1) directly probing the device under operation in spatial resolution, 2) time-resolved ability in nanosecond range, 3) visualization of the carrier motion, 4) investigation for mobile charge and trapped charge and so on. Recently, SHG becomes a useful spectroscopic tool in the study, especially surface and interface of organic and inorganic semiconductor by probing [36] of the electric field in material. Here I would like to briefly explain two techniques for the EFISHG measurement, one is the observation of EFISHG spectrum and the other is visualization of EFISHG signal by using TRM-SHG. Both techniques has nearly the same experiment set up, but a little difference at the detector of the EFISHG signal only as mentioned above.

2.7.4 SHG spectrum from perovskite thin film

Selecting an appropriate wavelength is important to observe the SHG signal from perovskite effectively because the SHG intensity strongly depends on materials itself and fundamental wavelength used. Firstly, we had to find out the proper wavelength of the SHG measurement because the SHG intensity is resonantly enhanced at a specific wavelength and using of an appropriate wavelength makes it easy to visualize the carrier motion of the selected materials. According to the simple consideration of the resonant condition of the EFISHG process, the resonant enhancement will occur when the fundamental or the SH wavelength coincides with the band gap. To find out the appropriate wavelength, the SHG spectrum was measured from 1500 to 1600 nm.

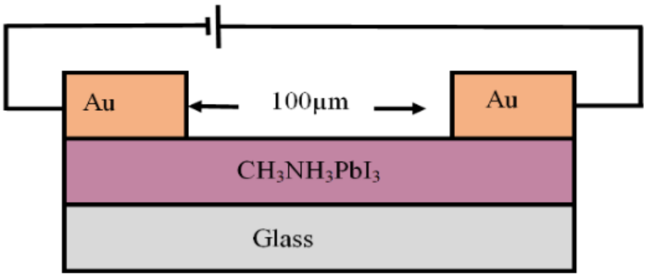

(a)

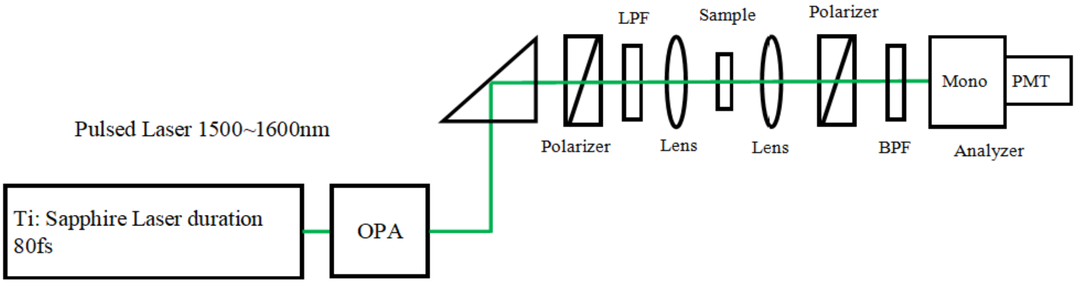

(b)

Figure 2.23: (a) Cross-sectional view of the sample (b) Experimental Setup of SHG intensity

Fig. 2.23 (a) shows the cross-sectional view of the perovskite sample device for the electrical connection and Fig. 2.23 (b) shows an optical setup for the microscopic SHG measurement. For that case, we made perovskite film on the glass with Au electrode. The SHG output was measured by a photomultiplier tube.

2.7.5 Time-resolved microscopic second harmonic generation (TRM-SHG)

TRM-SHG technique was successfully developed in our laboratory, and it had been used to investigate the surface potential of organic materials such as CuPc films [7] and applied to probe the electric field distribution and carrier injection into OFET [8,9]. As the name is time-resolved measurement, it is important to make sure for precisely controlling the delay time of the pulse voltage and laser pulse. The experimental setup is depicted in the following figures.

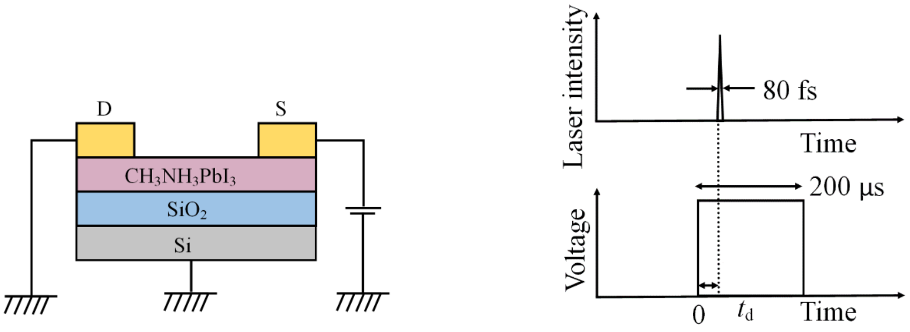

(a)

(b)

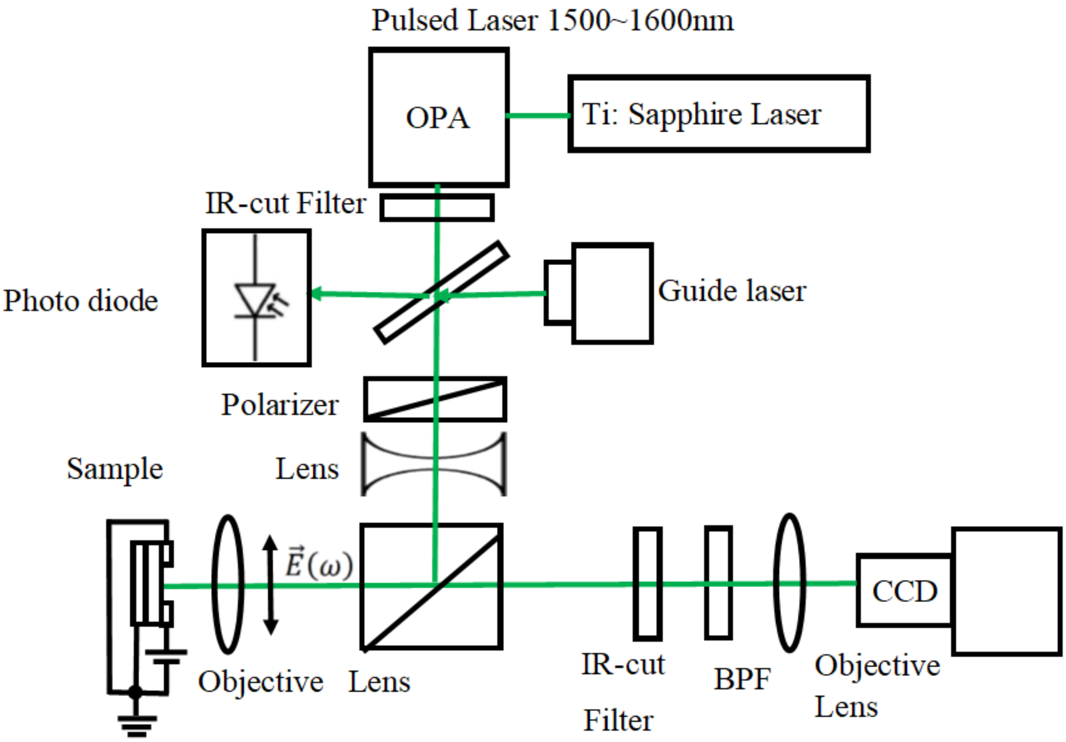

(c)

Figure 2.25: (a) Schematic diagram of the top contact FET device and electrical connection. (b) Timing chart of the voltage pulse applied to FET and the laser pulse. (c) Experimental set up for visualization of EFISHG.

Fig. 2.25 (a) represents the schematic image of the sample structure and electrical connection used in the TRM-SHG experiment. Fig. 2.25(b) illustrates the timing chart of the applied pulse voltage and incident laser light in the TRM-SHG measurement, where t_d is a delay time between the rising edge of the voltage and the laser pulse. By changing the delay time t_d, we can get the time evolution of the electric field distribution in the channel. The pulse voltage was applied to the source electrode, and the gate and drain electrodes were connected to ground, as shown in Fig. 2.25 (a). Fig. 2.25 (c) shows the experimental setup for the visualization of EFISHG. Ti: Sapphire laser was used as an incident light source. The pulse laser from an optical parametric amplifier (OPA) whose duration was about 80 fs, were focused on the channel region of the perovskite FET with normal incidence using the objective lens. The polarization of the fundamental light was chosen in the direction corresponding to the channel direction (source-drain direction), and SHG signal was captured by CCD camera. The pulse width, repetition rate, and amplitude applied to the FET were 200 μs, 1 kHz and 100 V, respectively. All measurements were performed in the ambient laboratory atmosphere. Fig. 2.26 depicts the photo of the experimental set up of TRM-SHG measurement.

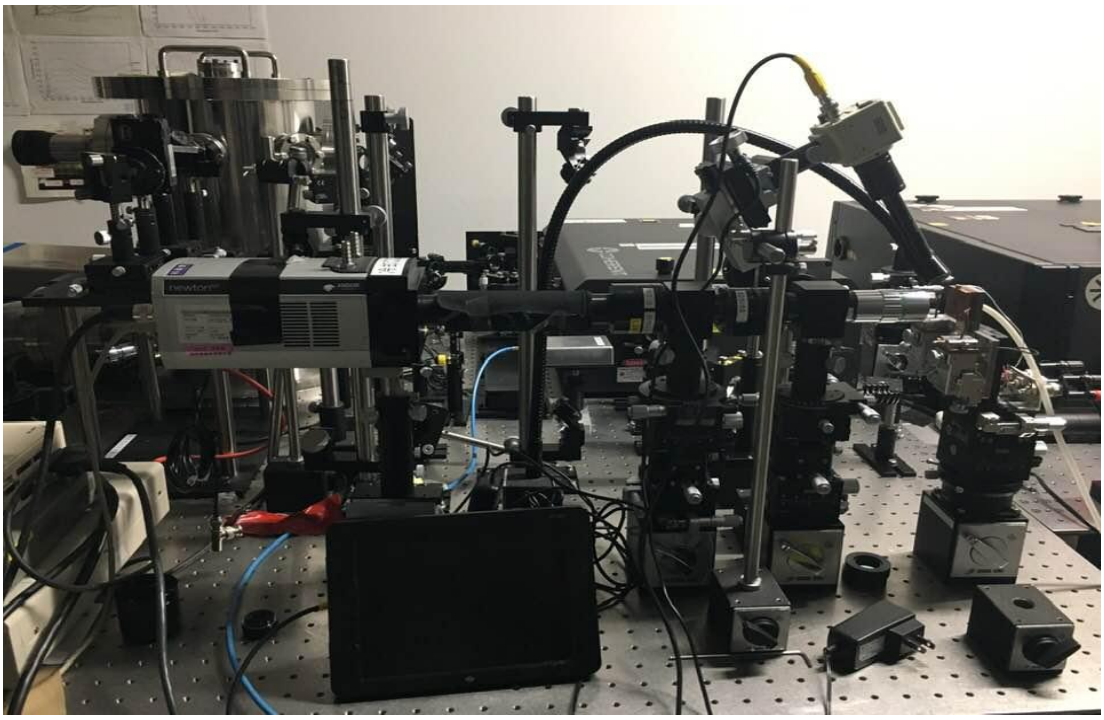

Figure 2.26: Photo of TRM-SHG experiment set up

2.8 Conclusion

Even though hybrid organic-inorganic halide perovskite materials are very popular in the photovoltaic world, there is a big gap for the understanding of the fundamental properties. Here, we conducted the transport characteristic and carrier behaviors in these materials by visualization of spectroscopic measurements such as FET, eTOF, EFISHG, and PL quenching measuring.

In this chapter, firstly, I presented the fabrication process and how to deposit for one-step and two-step perovskite thin film. Moreover, the basic principles of characterization techniques such as absorbance and photoluminescence measurement and XRD measurement were mentioned. For a full understanding of carrier behavior inside of perovskite materials, electrical and optical properties were emphasized for both steady-state and transient state. Then relevant experimental methods were explained with a focus on their basic principles and background theory. Before each description of measurement, the importance of each measurement methods to study the carrier behaviors were explained.

The basic principle of FET measurement and current-voltage characteristics are described. To investigate the steady-state electrical characteristics of the perovskite materials, we conducted conventional FET measurement because FET measurement is the basic and most widely used methods to characterize the current that flows through the device.

To study the transient characteristics and to evaluate the direct evidence of transport mechanism, lateral TOF measurement were used for these studies. Moreover, to extract the charge mobility from lateral TOF measurement, the charge propagation model along the channel and interface charge propagation model were briefly described for not only two electrode systems but also three-electrode systems.

For direct visualization of carrier behavior, we used novel spectroscopic techniques such as PL and TRM-SHG measurement. From, TRM-SHG technique we could directly observe the transient electric field. Based on the transient electric field migration, mobility and trapped charged density can be quantitatively estimated. In the following chapters, we will discuss the experimental results obtained from these measurements and propose new perspectives on the carrier behaviors of perovskite materials.

Bibliography

[1] T. Manaka, E. Lim, R. Tamura, and M. Iwamoto, “Direct imaging of carrier motion in organic transistors by optical second-harmonic generation,” Nat. photonics 1 (10) 581, 2007.

[2] T. Manaka and M. Iwamoto, “Optical second-harmonic generation measurement for probing organic device operation,” Light Sci. Appl. 5 (3) e16040, 2016.

[3] T. Manaka, E. Lim, R. Tamura, and M. Iwamoto, “Modulation in optical second harmonic generation signal from channel of pentacene field effect transistors during device operation,” Appl. Phys. Lett. 87 (22) 222107, 2005.

[4] S. Hayashi, K. Kaneto, and K. Yoshino, “Quenching of photoluminescence in poly (thiophene) films by electrochemical doping,” Solid State Commun. 61 (4) 249-251, 1987.

[5] P. Dyreklev, O. Inganäs, J. Paloheimo, and H. Stubb, “Photoluminescence quenching in a polymer thin-film field-effect luministor,” J. appl. phys. 71 (6) 2816-2820, 1992.

[6] T. Manaka, M. Nakao, D. Yamada, E. Lim, M. Iwamoto, “Optical second harmonic generation imaging for visualizing in-plane electric field distribution,” Opt. Express B 15964-15971, 2007.

[7] D. Yamada, T. Manaka, E. Lim, R. Tamura, M. Weis, M. Iwamoto, “Injected carrier distribution in a pentacene field effect transistor probed using optical second harmonic generation,” J. Appl. Phys. 104 (7) 074502, 2008

[8] M. Iwamoto, T. Manaka, M. Weis, D. Taguchi, “Probing and modeling of interfacial carrier motion in organic devices by optical second harmonic generation,” J. Vac. Sci. Technol. B. 28 (4) C5F12, 2010.

[9] N. J. Jeon, J. H. Noh, Y. C. Kim, W. S. Yang, S. Ryu, and S. I. Seok, “Solvent engineering for high-performance inorganic–organic hybrid perovskite solar cells,” Nat. Mater. 13 (9) 897, 2014.

[10] Z. Xiao, Y. Yuan, Q. Wang, Y. Shao, Y. Bai, Y. Deng, Q. Dong, M. Hu, C. Bi, and J. Huang, “Thin-film semiconductor perspective of organometal trihalide

perovskite materials for high-efficiency solar cells," Mater. Sci. Eng. R Rep. 1-38, 2016

[11] Z. Xiao, Q. Dong, C. Bi, Y. Shao, Y. Yuan, and J. Huang, "Solvent annealing of perovskite-induced crystal growth for photovoltaic-device efficiency enhancement," Adv. Mater. 26 (37) 6503-6509, 2014.

[12] H. Zhou, Q. Chen, G. Li, S. Luo, T. Song, H.-S. Duan, Z. Hong, J. You, Y. Liu,Y. Yang, "Interface Engineering of Highly Efficient Perovskite Solar Cells," Science 345, 542, 2014.

[13] M. Lee, J. Teuscher, T. Miyasaka, T. Murakami, and H. Snaith, "Efficient Hybrid Solar Cells Based on Meso-Superstructured Organometal Halide Perovskites." Science, 338, 643, 2012.

[14] B. Valeur, "Molecular Fluorescence: Principles and Applications," Wiley-VCH Verlag GmbH, 2001.

[15] R. Tilley, "Crystals and crystal structures," Chapter 6 "Diffraction and crystal structures," John Wiley & Sons Ltd., 2006.

[16] M. M. Lee, J. Teuscher, T. Miyasaka, T. N. Murakami and H. J. Snaith, "Efficient hybrid solar cells based on meso-superstructured organometal halide perovskites," Science 338 (6170) 643-647, 2012.

[17] A. Poglitsch and D. Weber, "Dynamic disorder in methylammoniumtrihalogeno27 plumbates (II) observed by millimeter- wave spectroscopy," J. Chem. Phys. 28 (87) 6373, 1987.

[18] N. G. Park, "Organometal perovskite light absorbers. Toward 20% efficiency low-cost solid-state mesoscopic solar cell," J. Phys. Chem. Lett. 4 (2) 2423, 2013.

[19] G. Horowitz, X. Peng, D. Fichou, and F. Garnier, "The oligothiophene based field effect transistor: How it works and how to improve it," J. Appl. Phys. 67 (1) 528-532, 1990.

[20] S. M. Sze, and K. K. Ng, "Physics and properties of semiconductors—A review," John Wiley & Sons Ltd., 2006.

[21] J. Zaumseil and H. Sirringhaus, "Electron and ambipolar transport in organic field-effect transistors," Chem. Rev. 107 (4) 1296-1323, 2007.

[22] L. Haichao, D. Cong, B. Li, L. Ye, Y. Ge, X. Tang, Y. Shen, Y. Wen, J. Wang, C. Zhou, and B. Yang, " Discrete dimeric anthracene stackings in solids with enhanced excimer fluorescence," Cryst. Growth Des. 17 (6) 2945 - 2949, 2017.

[23] M. J. Kim, S. Choi, M. Lee, H. Heo, Y. Lee, J. H. Cho, and B. Kim, “Photoresponsive transistors based on a dual acceptor-containing low-bandgap polymer,” ACS Appl. Mater. Interfaces 9 (22) 19011-19020, 2017.

[24] Y. Wang, Q. Liao, G. Wang, H. Guo, X. Zhang, M. A. Uddin, S. Shi, H. Su, J. Dai, X. Cheng, A. Facchetti, T. J. Marks, and X. Guo, “Alkynyl-functionalized head-to-head linkage containing bithiophene as a weak donor unit for high-performance polymer semiconductors,” Chem. Mater. 29 (9) 4109 - 4121, 2017.

[25] J. R. Haynes and W. Shockley, “The mobility and life of injected holes and electrons in germanium,” Phys. Rev. 81 (5) 835, 1951.

[26] R. Lawrance and A. F. Gibson, “The measurement of drift mobility in semiconductors,” Proceedings of the Physical Society. Section B 65 (12) 994, 1952.

[27] M. Redecker, D. D. Bradley, M. Inbasekaran, W. W. Wu, and E. P. Woo, “High mobility hole transport fluorene-triarylamine copolymers,” Adv. Mater. 11 (3) 241-246, 1999.

[28] J. Haladyj, J. Michalski, and A. Szymański, “On the anomalous field dependence of drift mobility in thin organic films,” Phys. Status Solidi. A. Applied Research 80 (2) K137-K139, 1983.

[29] M. Redecker, D. D. C. Bradley, M. Inbasekaran, and E. P. Woo, “Nondispersive hole transport in an electroluminescent polyfluorene,” Appl. Phys. Lett. 73 (11) 1565-1567, 1998.

[30] “Organic electronics research group-research interests and projects” available: http://oe.phys.hkbu.edu.hk/index.php/research/

[31] P. M. Borsenberger and D. S. Weiss, “Organic photoreceptors for imaging systems”, Marcel Dekker, Inc. 280-281, 1993.

[32] G. Horowitz, X. Peng, D. Fichou, and F. Garnier, “The oligothiophene based field effect transistor: How it works and how to improve it,” J. Appl. Phys. 67 (1) 528-532, 1990.

[33] M. Weis, T. Manaka, and M. Iwamoto, “Origin of electric field distribution in organic field-effect transistor: Experiment and analysis,” J. Appl. Phys. 105 (2), 024505, 2009.

[34] A. Kohler, and H. Bassler, “Electronic processes in organic semiconductors,” Markono Print Media Pte Ltd., Singapore, 2015.

[35] R. W. Boyd, “Nonlinear optics” 3rd ed., Amsterdam ;Boston: Academic Press, 2008.

[36] G. Lupke, “Characterization of semiconductor interfaces by second-harmonic generation,” Surf. Sci. Rep. 35 75-161, 1999.

Chapter 3

Carrier behavior in hybrid organic inorganic perovskite materials for electrical measurement (FET characteristics and TOF)

3.1 Introduction

As described in chapter 1, perovskite photovoltaic cells have seen an exceptional ascend in power conversion efficiencies over a short period [1-3]. However, many aspects of the fundamental charge transport such as carrier injection and carrier transport properties in these organic inorganic hybrid perovskites remained unexplored [4-7]. Here, we studied the electrical carrier transport behavior of perovskites thin film ($MAPbI_3$) by using field-effect-transistor (FET) characteristics measurement and the lateral time of flight (TOF) method; based on direct time resolved measurement of current, arising from the drift of free charge carriers in electric field.

FET characteristics provide a versatile platform to study the charge transport phenomena of semiconductor for a controlled manner. In addition to the mobility evaluation, FET measurements enable us to discuss a variety of electrical properties and to provide valuable insight into the physics of organic and inorganic semiconductors [8]. The time of flight method is also a powerful technique for investigating many of the electrical properties of semiconductors such as drift mobility, saturation velocity, charge collection and trapping lifetimes [9].

In order to observe the fundamental carrier transport properties of perovskite thin film, I fabricated top contact bottom gate FET structure by using simple deposition spin coating method for both one-step and two-step method. For the detail sample preparation, see in subsection 2.6.2.2. Before, discussion for relevant measurements, I would like to describe the characterization of fabricated film.

3.2 Characterization of fabricated film

I fabricated bottom contact top gate FET structure with gold (source-drain contacts) and SiO_2 gate dielectric using one-step and two-step solution process as described in subsection 2.2.3 and 2.2.4. Figure 3.1 (a) and (b) show microscopic images of the one-step and the two-step perovskite films and insets are the SEM image for detail observation of surface morphology, respectively.

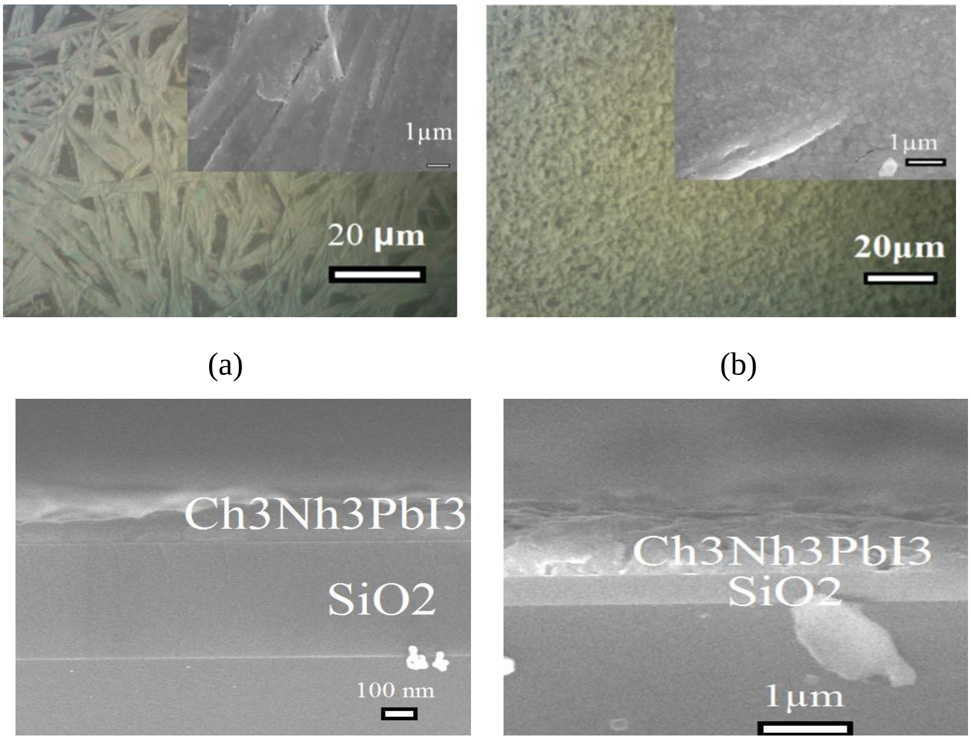

(a) (b)

(b) (d)

Figure 3.1: Optical microscope images for (a) one-step (b) two-step perovskite film: inset is the SEM top view. Cross sectional view of SEM of (c) one-step and (d) two-step fabricated perovskite film.

The one-step solution process easily causes uncontrollable precipitation of perovskites and leads to large morphological variations that strongly depend on the fabrication conditions [10]. As shown in Fig. 3.1 (a), the one-step fabricated thin film showed irregularly distributed large needle-like structures and large pinholes. This was probably due to fast crystallization of the perovskite during spin coating [11, 12], which made it difficult to estimate the mobility of FET at room temperature. As shown in Fig. 3.1 (b) two-step spin coated perovskite thin film was better coverage than one-step spin coated film and it exhibited much better transport characteristics. Figure 3.1 (c) and (d) shows the SEM cross sectional view of one-step and two–step fabricated perovskite thin film, respectively. The average thickness of one-step and two-step fabricated thin films were 300 nm and 500 nm, respectively. Moreover, one-step spin coated perovskite solar cells with needle like structure had been reported with low PCE and large hysteresis [11-14]. Although our fabricated thin film morphology was still capable of improvement, both films were worth to discuss the validity of the novel methods for visualization of carrier motion in perovskite film in our studies.

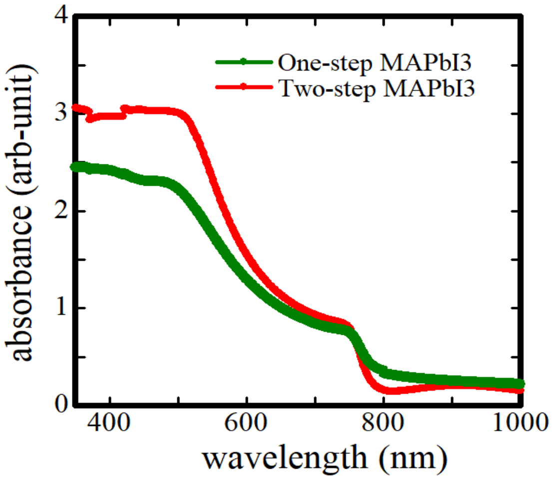

Figure 3.2: The absorbance spectrum for one-step and two-step $MAPBI_3$ film on the glass substrates.

Figure 3.2 shows the absorbance spectrum of one-step and two-step fabricated films on the glass substrates. The absorption edge of both films were same. However, the strong and broad absorption in the ultraviolet and visible light range of two-step fabricated film revealed that this kind of perovskite layer was a good light absorber than one-step fabricated film. The absorption spectrum of both fabricated films indicated that the absorption edge was 780 nm. Therefore, we estimated that the optical band gap of our fabricated $CH_3NH_3PbI_3$ films were 1.59 eV which was consistent with the other groups results [15]. Then, XRD analysis was performed to characterize the crystalline properties of the both fabricated film.

The crystal phase of fabricated PbI_2, one step $MAPbI_3$ and two-step $MAPbI_3$ were characterized by X-ray diffraction measurement; using a Rigaku RINT X-ray diffractometer CuKα source (λ= 1.5418 °A). For the XRD measurement, silicon substrates without electrodes were used. The XRD patterns of the spin-coated PbI_2, the one-step and the two-step fabricated perovskite films on silicon substrate are shown in Fig. 3.3.

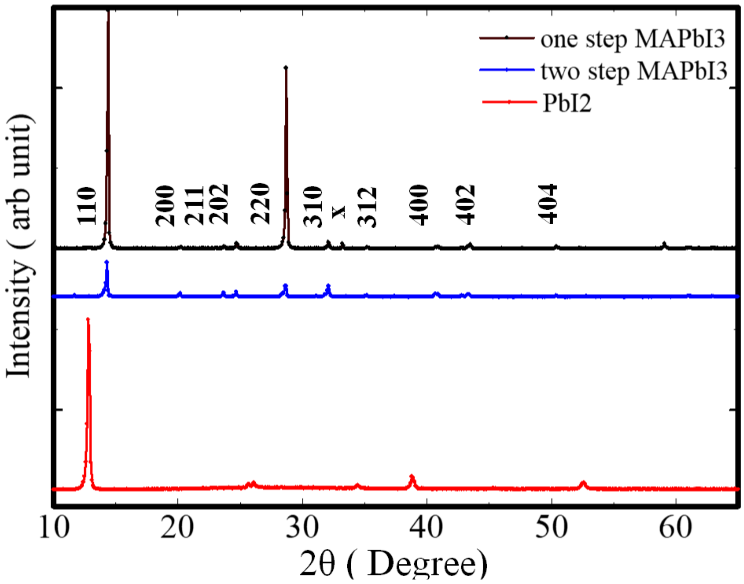

Figure 3.3: XRD patterns of the one-step $MAPbI_3$, the two-step $MAPbI_3$and PbI_2 on silicon substrate.

As shown in Fig. 3.3, the one-step and two-step fabricated films show the diffraction peaks at 2θ of 14.3°, 20.3°, 23.7°, 24.7°, 28.7°, 32.1°, 35.2°, 40.9°, 43.5° and 50.4° those are assigned to the crystal plane of (110), (200), (211), (202), (220), (310), (312), (400), (402) and (404) of the tetragonal $CH_3NH_3PbI_3$ phase, respectively and high crystallinity [16]. Even though we observed the morphological difference between the one-step and the two-step fabricated thin films, the crystal structures of both films were not significantly different. An evident from XRD pattern, absence of the diffraction peak of PbI_2 implies that the PbI_2 impurity phase is negligible in spite of that needle-like structure. In this sense, our perovskite films sufficiently served the purpose of this study and for visualizing carrier motion in the perovskite film. Nevertheless, the morphology of the film will be improved as further studies.

3.3 FET measurement

Firstly, we carried out FET measurement for one-step spin coated FET at room temperature for transfer characteristics.

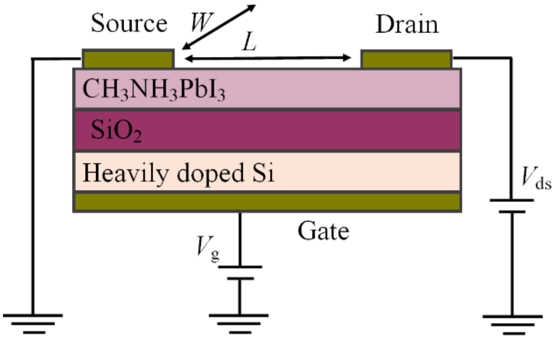

Figure 3.4: Electrical connection of perovskite FET.

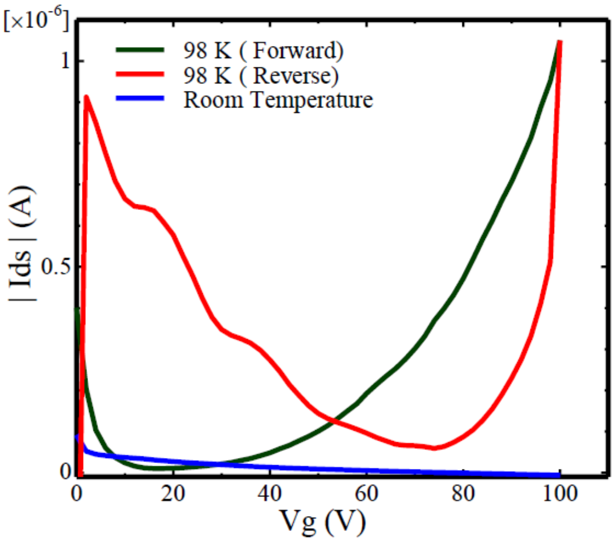

Figure 3.5: Transfer characteristics of the hybrid perovskite FET measured at room temperature and 98 K under positive gate voltage application for forward and reverse sweep while V_d = 100 V.

Figure 3.5 shows the transfer characteristics of the perovskite FET measured at room temperature and 98 K. As shown in Fig. 3.5, no induced transport could be observed at room temperature for these transistors. Then, we tried to observe the transfer characteristics at low temperature. For low temperature FET measurement, FET devices were mounted into liquid nitrogen cold stage that could reduce the operating temperature of the device from 300 K to 77 K. We could observe the current modulation from 198 K to 93 K when the temperature was reduced. This could be explained by the screening of the gate field due to the accumulation of migrated ions at the gate dielectric/perovskite interface at room temperature [17]. We confirmed these facts by reducing the temperature less than 150 K enabled to observe the modulated drain current probably due to the freezing of the ion migration.

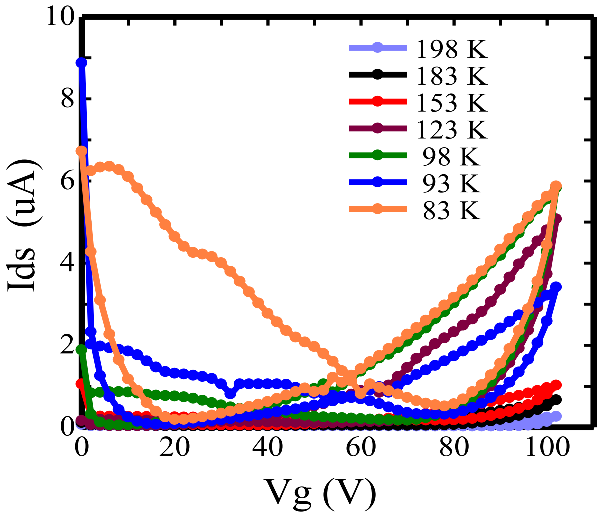

Figure 3.6: Temperature dependent transfer characteristics.

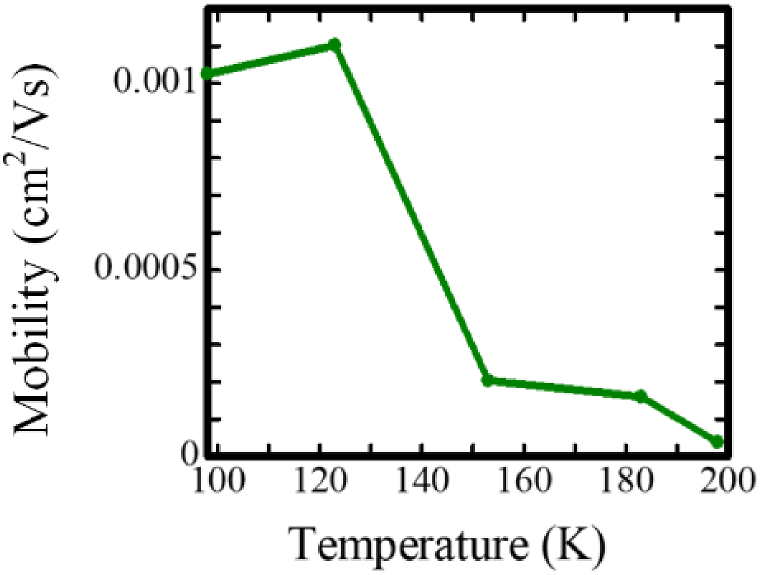

Figure 3.7: Graph of temperature versus mobility.

Figure 3.6 indicates that when temperature reduced under 198 K, the modulated current prominent and increased with temperature decreased. Under 98 K, the transfer characteristics exhibited dominant ambipolar behavior and the maximum on/off ratio is nearly about 5 orders of magnitude.

Moreover, regarding to the structural phase transition, we also noted that at 160 K the tetragonal phase changed to the orthorhombic phase [18]. This structural phase transition would induce the change of effective mass and dielectric constant [17, 19-20]. Both of which could affect the field-effect mobility [17, 21]. In addition, Boltzman transport theory stated that the mobility of tetragonal phase should be smaller than that of orthorhombic phase [17]. And also the phase transition temperature depends on the thickness of the fabricated film. For the thicker film, the phase transition temperature shifts higher [22]. For our fabricated film, we can assume that the phase transition occurs near 153 K. Thus we observed the smallest field effect mobility at 153 K as shown in Fig. 3.6 that probability due to the phase transition as pointed above reference.

The field effect mobility (μ) and threshold voltage (V_{th}) can be extracted from transfer characteristics Eq. (3.1) as already explained in subsection 2.4.2.

$$I_{ds} = \frac{W}{2L} C_i \mu (V_g - V_{th})^2 \,. \tag{3.1}$$

where W, L and C_i are the channel width, the channel length and the gate capacitance, respectively. Despite significant hysteresis characteristics, the electron and hole mobility were extracted from the forward sweep of the transfer characteristics as $1.3 \times 10^{-3}\ \mathrm{cm^2V^{-1}s^{-1}}$ and $1 \times 10^{-3}\ \mathrm{cm^2V^{-1}s^{-1}}$ at 98 K, respectively.

Significant hysteresis was commonly explored in perovskite thin film transistors, which hinder fully understanding the charge transport properties and exact determination of carrier mobility in such perovskite materials. The origin of this hysteresis has been attributed to ferroelectricity, screening effect arising from field induced drift of ions and trapping /detapping of charge carriers at the interface [23]. In addition, charge traps and surface dipoles at the untreated semiconductor dielectric interface may be also attributed to the hysteresis effect [24]. However, there is no conclusive explanation yet.

In our FETs, significant hysteresis had been observed for all temperature. Indeed, when the temperature was decreased, the rate of ion migration should be less due to the freezing of ion at low temperature. Therefore, the presence of hysteresis under 98 K proposed that the ion motion just partly contributed to the hysteresis.

Moreover, the origin of the hysteresis was possibly due to the morphological irregularity of the one-step film, and the untreated semiconductor-dielectric interfaces which were also reported for light-emitting FETs with hybrid perovskites [17]. This hysteresis effect could be effectively suppressed by improving the quality of perovskite thin films. To optimize the device performance, we fabricated two-step perovskite thin film. Then we continued the measurement of I-V characteristics at room temperature and low temperature. Following are the results and discussion for two-step perovskite film.

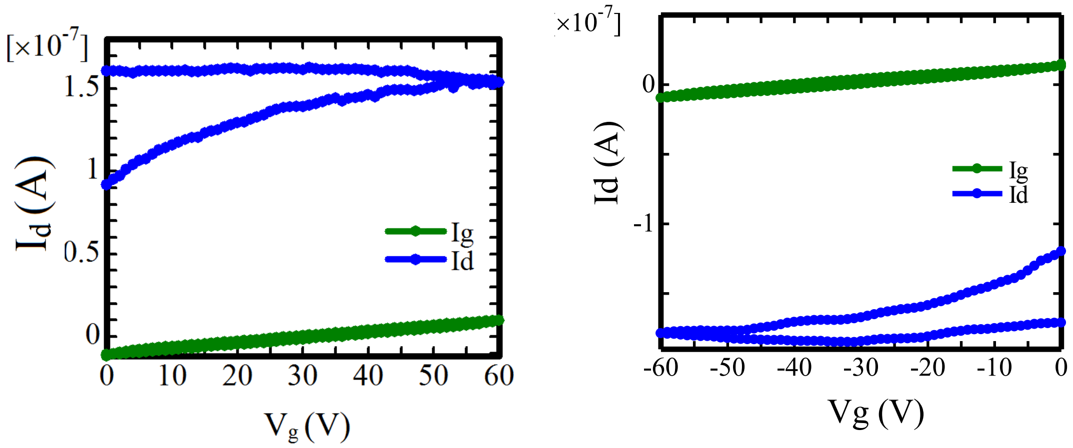

Figure 3.8: Transfer characteristics for (left) n-type transistor (right) p-type transistor at room temperature when V_d = 60 V for n-type and V_d = - 60 V for p-type.

At room temperature, small modulated current could be seen for two-step fabricated film. Even though, the film morphology of the two-step fabricated thin film is better than those of one-step film, the behavior of I-V characteristics was still complex and non-ideal behavior with large hysteresis due to the signature of ion screening effect at room temperature.

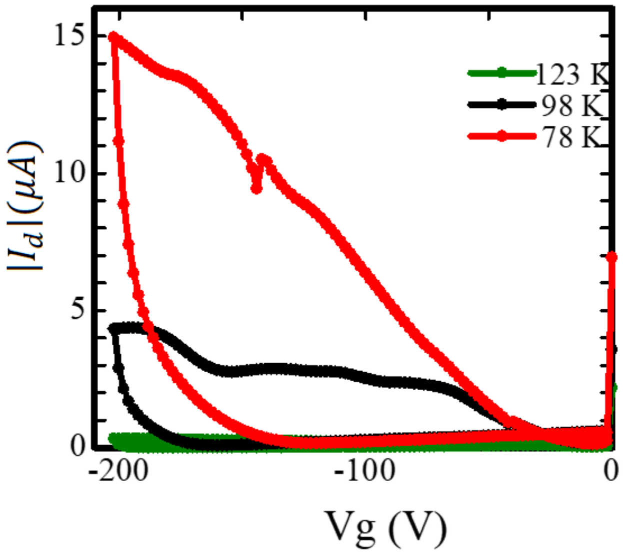

Figure 3.9: Transfer characteristics of two step fabricated film.

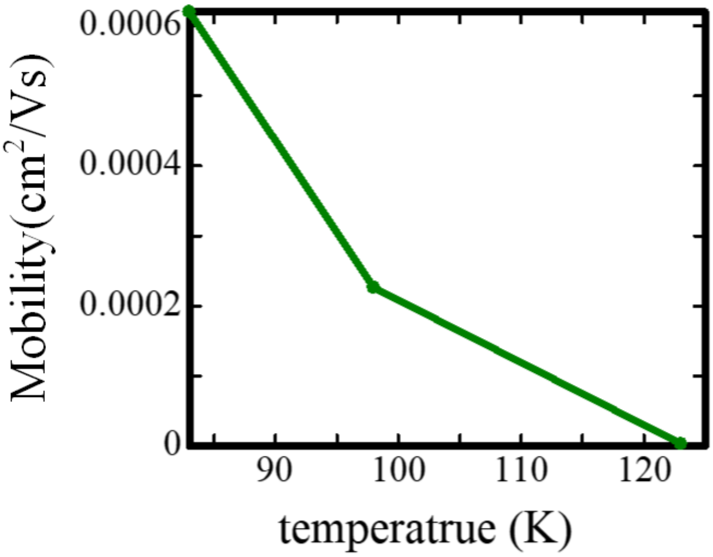

Figure 3.10: Graph of temperature versus mobility for two-step fabricated film.

Furthermore, it should be noted that the transfer curves exhibits weak but notable hysteresis effects same with the previous experimental results. But p-type behavior is more influenced than n-type behavior under 123 K. We noticed that the mobility of two-step was slightly lower than one-step fabricated film. It probably due to the low film quality of the fabricated thin film. For the thicker the film, there will be higher roughness and it affects to increase charge carrier scattering, which suffers in lower mobility.

Regards for the hysteresis, we found significant hysteresis effect for both fabricated film. Therefore, we had to find the origin of hysteresis at low temperature. On the other hand, the typical activation energies (E_A) of iodide (I^+), methylammonium (MA^-) and lead (Pb^{2-}) have been calculated as 0.58, 0.84, and 2.31 eV [25]. That pointed out the iodine vacancies can move more easily as the majority mobile ions, and its diffusion coefficient was estimated to be 10^{-12} cm^2s^{-1} at 320 K. Moreover by typical Bolzmann probability, the diffusion coefficient of the easiest mobile iodine vacancies in $MAPbI_3$ perovskite film would be expected to decrease by a factor of 10^5 between room temperature and 100 K[26]. This point well explained the other origin of hysteresis at low temperature. However, further investigator is needed to fully understand the charge carrier transport in perovskites. From the measurement we sured that the origin of this complex behavior at room temperature and low temperature not only ion movement but also other effects such as charged traps.

3.4 Time of flight method

In the previous section, we investigated the charge charier transport from current voltage characteristics of FET structure at room temperature and low temperature.

However, for investigating the carrier transport properties of the perovskite materials, FET mobility measurement is not sufficient because it strongly depends on electrodes and the gate insulator and extrinsic effect such as temperature. On the other hand, for investigation of the intrinsic charge properties and drift mobility in organic materials, time of flight (TOF) method is more suitable [27-30].

3.4.1 Conventional time of flight method

For a conventional TOF method, the measured mobility corresponds to the mobility of the carrier transporting perpendicular to the substrate. This method is applicable to the vertical carrier transport properties. However, sometimes it is necessary to directly investigate the carrier transport for a lateral carrier transport support for transistor structure.

3.4.2 Lateral time of flight method

By lateral time of flight method, the lateral charge carrier transport and drift mobility in perovskite thin film has been investigated by transient photocurrent measured for various electric field strengths [31]. The experimental setup are briefly explained in section 2.5.2.1.

The sample structure for photocurrent measurement consisted of a glass substrate, with gold electrode. The glass substrates were first cleaned sequentially in, acetone, ethanol and water. Then treated by ozone. The film fabrication and characterization of the film of one step and two step were same as the FET structures, described in the previous section.

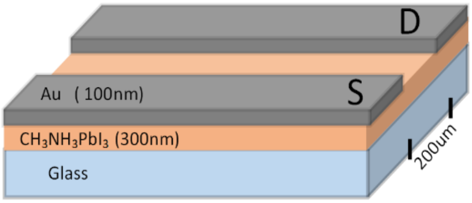

(a)

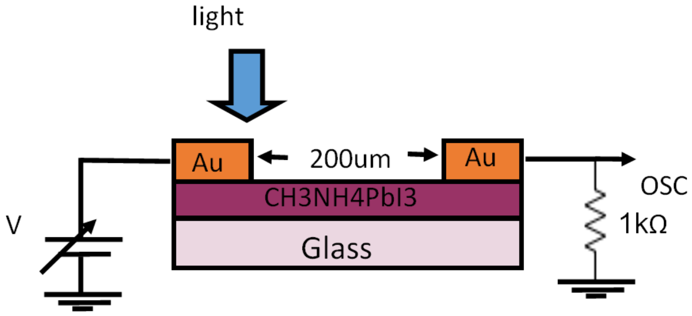

(b)

Figure 3.11: (a) Structure of perovskite thin film device for TOF measurement (b) electrical connection of the fabricate film for lateral TOF measurement.

The perovskite layer was exposed to the laser light through the glass substrate. The gold electrodes were connected in a circuit with a voltage source and the resistance. The transient current was measured by the voltage drop across the load resistance using the oscilloscope. The load resistance (R_{load}) 10 kΩ was much smaller than the channel resistance. All measurements were performed in a laboratory ambient atmosphere.

For this TOF measurement the center of the laser spot was adjusted at the edge of the one of the electrode because the photocurrent intensity depends on the excitation position and drastically decreased with the distance between the excitation position and the edge. The modulated laser light spot was focused on the samples through an objective lens with the diameter of about 50 µm. The irradiation pattern and position in the samples are shown in Fig. 3.12.

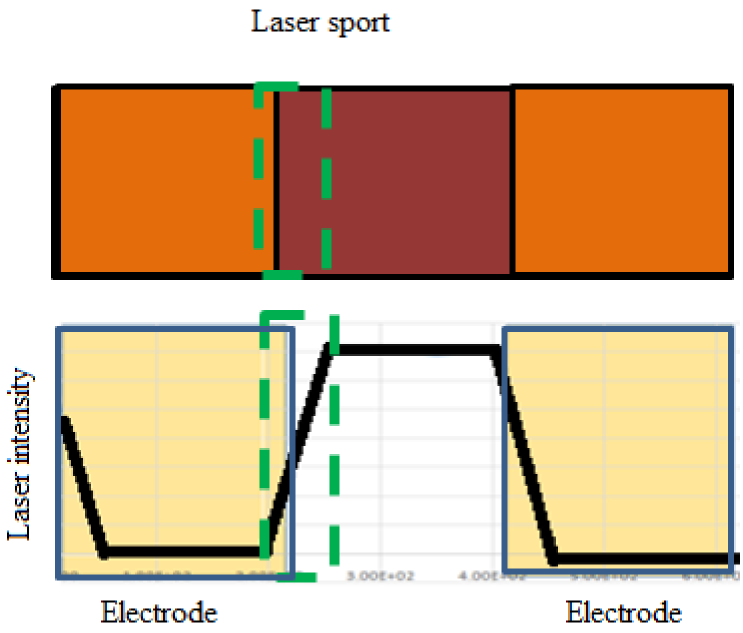

Figure 3.12: The light intensity Vs position of electrode.

Measurement of the transient photocurrent *i*(t) displayed anomalous transport properties. The long tail of *i*(t) indicates a dispersion of carrier transit times and shape invariance of *i(t)* to electric field and sample thickness [32]. On the basis of the above-mentioned discussion, the lateral charge carrier transport and drift mobility in perovskite thin film with 200 µm electrode distance has been analyzed by transient photocurrent measured for various electric field strengths as shown in Fig. 3.13. We can clearly see the transient curves have a long tail and no plateau region. The origins of no plateau and continuously declining current are seen in the loss of carriers induced by deep trapping, sample inhomogeneities, local field variation due to trapped charges and spreading of the sheet of charges due to multiple hopping or dispersion of distances between neighboring sites [33-34].

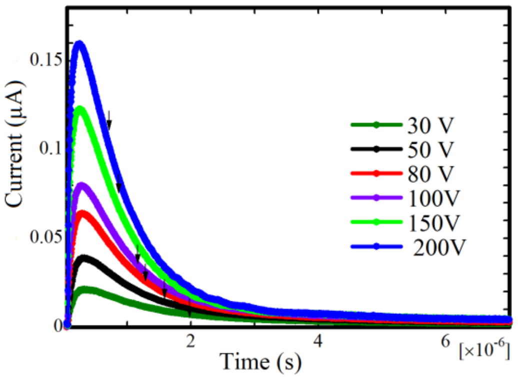

Figure 3.13: Transient photocurrent of a sample with an electrode distance of 200 μm (The arrows are transit time)

The shape of these transient current indicates the lateral carrier transport of perovskite has a highly dispersive transport behavior, which showed that there was multiple trapping in the fabricated film. Because along the channel, some charges can be trapped and these trapped charges suffers the lateral mobility due to local electric field variation. For this dispersive carrier transport, it was difficult to directly determine the transit time. We could determine the transit time from the double logarithmic plot. Figure 3.14 shows the double logarithmic plot of the same sample as in Fig. 3.13.

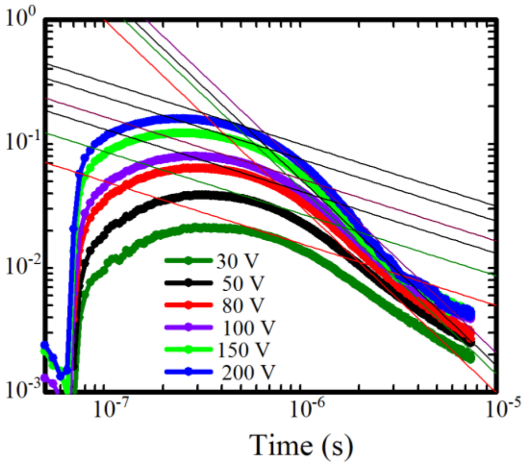

Figure 3.14: log log plot for the same sample in Fig. 3.13.

The transit time t_r can be assumed from the intersection from log-log plot graph as described in [32]. To calculate the carrier mobility, we could determine the transit time t_{tr}, from the intersection of two slope lines described in Ref. 33 based on Scher-Montroll theory. Scher-Montroll theory pointed that if the sum of two slopes was 2 and obeyed power law, the current would be the hoping time distribution function [33]. The transit times were evaluated by the inflection points, whose positions are depicted in the Fig. 3.13 by arrows.

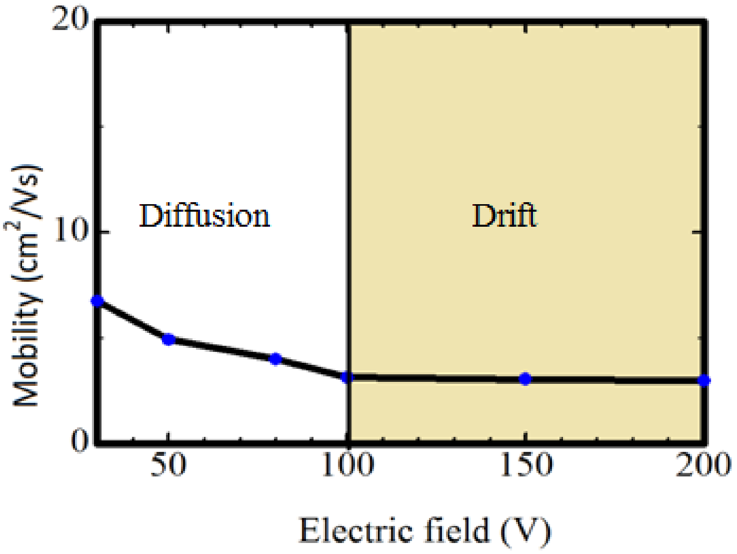

Figure 3.15: Hole motilities for different voltages.

Based on the transit time, the evaluated electron and hole mobility are ranged at $4\ \mathrm{cm^2V^{-1}s^{-1}}$ and $3\ \mathrm{cm^2V^{-1}s^{-1}}$ respectively, at the room temperature. We observed that the drift motilities were dispersive (time dependent) and reasonable. It was also consistent with the reported hole drift mobility for two step $MaPbI_3$ from other group [35]. Fig. 3.15 shows that the hole motilities for different voltages from 20 to 200 V. At the low electric field under 100 V, diffusion current overwhelmed and voltage dependent mobility could be seen. However, drift current could be maintained at the over 100 V.

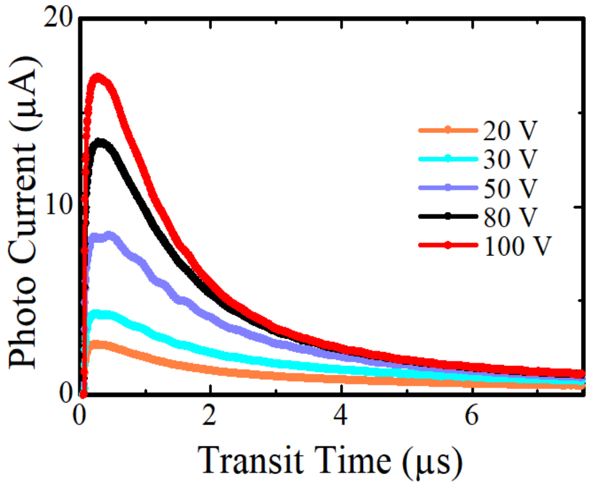

Figure 3.16: Two step voltage dependence TOF measurement.

Figure 3.16 shows the transient photocurrent of the two-step sample with a 200 μm electrode distance measured under different electric field from 20 V to 100 V. The transient curves had also a long tail and sometimes we found plateau region. The result showed that the transport had a highly dispersive behavior, which indicated also that there existed multiple trapping in the deposited film. For two-step deposited film, we could reduce the scattering and reflection of light due to thicker film than one-step fabricated film. And non-uniform electric field inside the materials due to grain and trap. The long tail represented the dribble of slow carriers and migration of ion as shown in Fig. 3.15. Transit time is nearly about 1 μs for 100 V and the hole mobility is 3.7 $cm^2V^{-1}s^{-1}$. Compared with one-step deposited film's mobility, two-step value is smaller due to large grain in thicker films and more traps could be affected. But the value of the mobility was more accurate than one-step film, due to well control for the light scattering and reflection occurred in one-step film. From this experiment, we studied the transport in different layers and the effects of different surface condition on carrier transport. Figure 3.17 shows the comparison of hole and electron mobility for different electric fields.

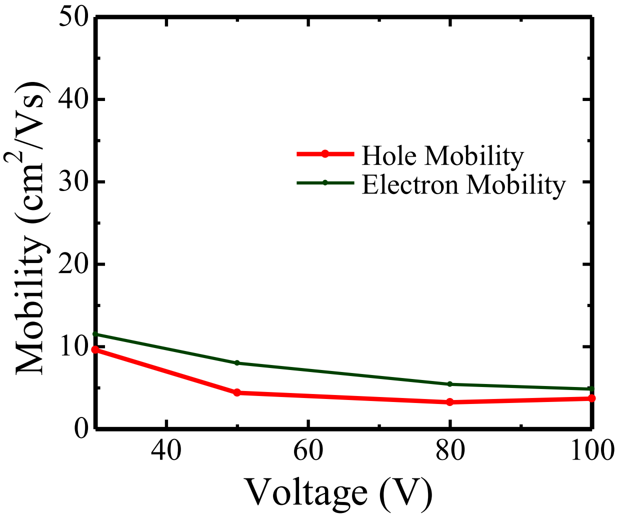

Figure 3.17: Hole and electron motilities for different voltages.

The relatively low mobility for both carriers compared to reported vertical drift velocity measurement for single crystal structure could be attributed to scattering effects at surface [36]. Transport can be expected to be strongly influence by surface scattering and trapping at defects induced by surface treatment.

For the one reason of dispersion for our time of flight measurement, the absorption of photons in perovskite was quite strong so carriers were generated on thin films within a few micrometers from illuminated surface of sample. And the carrier scattering between electrode could be blurring most useful features of its photocurrent transient, mainly depend on the surface interfacial effects.

For both cases, we could see negative correlation of perovskite film. That was the lower voltage, greater the mobility. Even though there were many claims of transport properties reported for the $MAPbI_3$ materials, the origin of this negative correlation is still intriguing.

As principal, the carrier drift velocity in a material $v(E)$ is directly proportional to the electric field E and when we assume the carrier mobility μ is independent of electric field and represented the equations as follows.

$$v(E) = \mu E \tag{3.1}$$

When the electric field increase, the carrier velocity increase towards the maximum possible value. On the other hand, carrier mobility is dependent of the drift velocity and the primary factor is how long the carrier is ballistically accelerated by the electric field until it collides with something that can alters its direction and / or its energy called collision or scattering time. These collisions have two main origins, interactions with the lattice and interaction with impurities.

The carrier mobility depend on the time of different collision occurring during their displacement, because the presence of interaction with phonons, traps and other imperfections in the lattice. The lattice vibration increases with the application of the applied electric field and also scattering time increase. Therefore, the negative correlation of perovskite films due to the probability of collisions or scattering for increasing vibration.

3.5 Conclusions

This chapter has focused on the charge carrier transport. Here we carried out FET measurement to observe charge transport mechanism for organic inorganic hybrid perovskite thin films to understand the basic electrical transport properties. From the FET measurement, we observed intrinsic transport parameters of $CH_3NH_3PbI_3$ such as ambipolar nature of charge transport at low temperature, the understanding of the suppression of screening effects associated to the presence of ionic cations, and the direct determination of electron and hole motilities. The hysteresis at low temperature showed us it was not sufficient to conclude its only the ion migration. And also it can be probably due to the gate insulator effect and traps. The other possible origin is increase of diffusion coefficient of movable ions. However, more works is still requiring for limiting the ionic screening and improving of thin film crystallinity.

Then, a system for lateral TOF measurement has been constructed. In measurement, $CH_3NH_3PbI_3$ perovskites was deposited on a glass substrate by solution spin coating process. A transit time of holes and electrons between two contacts with distance 200 μm was observed and the corresponded hole and electron mobilities were $3\ \mathrm{cm^2V^{-1}s^{-1}}$ and $4\ \mathrm{cm^2V^{-1}s^{-1}}$ respectively. Moreover, the lateral carrier transport and photocurrent effects of perovskite films had been observed.

Here, TOF mobility is higher than field-effect transistor mobility, because TOF provides directly an intrinsic measure of the transport properties on and near the surface of the materials. Regarding for FET transport properties, carriers can be transported on interface layer based on the gate affected field. For the TOF transport properties, carriers can be transmitted on the whole fabricated film on the glass, like bulk transport. This kind of transport has higher mobile because it can avoid charge injection effects and gate composition dependent measurements.

Even though the TOF mobility was higher than mobility from the steady-state measurement (FET measurement), same mobility results are already exists from the reference [34]. This showed the result of lateral TOF experiment was reasonable for the perovskite materials and we could study the transient carrier behavior. We noticed drift motilities in lateral transport of perovskite thin films are dispersive and time dependent and diffusion motilities overwhelmed at the lower electric field. Dispersion was well known effect in low mobility materials but has not been reported in perovskites. But still lateral photocurrent time-of-flight of perovskite suffered from poor signal quality, due to drift carriers travelled across the surface between two electrodes and more influenced by surface properties, scattering and trapping at defects induced by surface treatment.

Here many aspects of the charge transport, such as the mechanism of carrier scattering and trapping, the role of ion screening, and the origin of unusual behaviors (hysteresis) could be explained by steady state FET measurement and lateral TOF measurement. A combination of FET and TOF investigation were performed to prove the different origin of disorder prevalent in the perovskite field effect transport.

And also it is important to probe the different scattering mechanism that govern the temperature dependent transport physics of these materials for achieving further improvements in device performance.

Bibliography

[1] A. Kojima, K. Teshima, Y. Shirai, and T. Miyasaka. “Organometal halide perovskites as visible-light sensitizers for photovoltaic cells,” J. Am. Chem. Soc. 131 (17) 6050-6051, 2009.

[2] W. S. Yang, J. H. Noh, N. J. Jeon, Y. C. Kim, S. Ryu, J. Seo, and S. I. Seok, “High-performance photovoltaic perovskite layers fabricated through intramolecular exchange,” Science 348 (6240) 1234-1237, 2015.

[3] W. S. Yang, B. W. Park, E. H. Jung, N. J. Jeon, Y. C. Kim, D. U. Lee, S. S. Shin et al, “Iodide management in formamidinium-lead-halide–based perovskite layers for efficient solar cells,” Science 356 (6345) 1376-1379, 2017.

[4] J. M. Frost, K. T. Butler, and A. Walsh, “Molecular ferroelectric contributions to anomalous hysteresis in hybrid perovskite solar cells,” Apl. Mater. 2 (8) 081506, 2014.

[5] H. J. Snaith, A. Abate, J. M. Ball, G. E. Eperon, T. Leijtens, N. K. Noel, S. D. Stranks, J. T. W. Wang, K. Wojciechowski, and W. Zhang, “Anomalous hysteresis in perovskite solar cells,” J. Phys. Chem. Lett. 5 (9) 1511-1515, 2014.

[6] Y. Shao, Z. Xiao, C. Bi, Y. Yuan, and J. Huang, “Origin and elimination of photocurrent hysteresis by fullerene passivation in $CH_3NH_3PbI_3$ planar heterojunction solar cells,” Nat. Commun. 5, 5784, 2014.

[7] E. L. Unger, E. T. Hoke, C. D. Bailie, W. H. Nguyen, A. R. Bowring, T. Heumüller, M. G. Christoforo, and M. D. McGehee, “Hysteresis and transient behavior in current–voltage measurements of hybrid-perovskite absorber solar cells,” Energ. Environ. Sci. 7 (11) 3690-3698, 2014.

[8] J. Zaumseil and H. Sirringhaus, “Electron and ambipolar transport in organic field-effect transistors,” Chem. Rev. 107 (4) 1296-1323, 2007.

[9] R. Dost, A. Das, and M. Gruel, “Time of flight mobility measurements in organic field-effect transistors,” J. appl. Phys. 104, 2008.

[10] Z. Xiao, Y. Yuan, Q. Wang, Y. Shao, Y. Bai, Y. Deng, Q. Dong, M. Hu, C. Bi, and J. Huang, “Thin-film semiconductor perspective of organometal trihalide perovskite materials for high-efficiency solar cells,” Mat. Sci. Eng. R. 101, 1-38, 2016.

[11] A. Dualeh, N. Tétreault, T. Moehl, P. Gao, M. K. Nazeeruddin, and M. Grätzel. “Effect of annealing temperature on film morphology of organic–inorganic hybrid pervoskite solid-state solar cells,” Adv. Func. Mater. 24 (21) 3250-3258, 2014.

[12] Z. R. Pratiwi, L. Nuraeni, A. H. Aimon, and F. Iskandar, “Morphology Control of MAPbI3 Perovskite Thin Film as An Active Layer of Solar Cells,” IOP Conf. Ser., Mater. Sci. Eng. 395 (1) 012010, 2018.

[13] D. Wang, Y. Chang, S. Pang, and G. Cui, “The effect of grain orientation on the morphological stability of the organic–inorganic perovskite films under elevated temperature,” J. Semicond. 38 (1) 014002, 2017.

[14] G. E. Eperon, V. M. Burlakov, P. Docampo, A. Goriely, and H. J. Snaith, “Morphological control for high performance, solution-processed planar heterojunction perovskite solar cells,” Adv. Funct. Mater. 24 (1) 151-157, 2014.

[15] M. Lee, J. Teuscher, T. Miyasaka, T. Murakami, and H. Snaith, “Efficient Hybrid Solar Cells Based on Meso-Superstructured Organometal Halide Perovskites,” Science 338, 643, 2012.

[16] T. Baikie, Y. Fang, J. M. Kadro, M. Schreyer, F. Wei, S. G. Mhaisalkar, M. Graetzel, and T. J. White, “Synthesis and crystal chemistry of the hybrid perovskite $(CH_3NH_3)PbI_3$ for solid-state sensitised solar cell applications,” J. Mater. Chem. A 1 (18) 5628-5641, 2013.

[17] X. Y. Chin, D. Cortecchia, J. Yin, A. Bruno, and C. Soci, “Lead iodide perovskite light-emitting field-effect transistor,” Nat. Commun. 6, 7383, 2015.

[18] C. Wehrenfennig, M. Liu, H. J. Snaith, M. B. Johnston, and L. M. Herz, “Charge carrier recombination channels in the low-temperature phase of organic-inorganic lead halide perovskite thin films,” Apl. Mater. 2 (8) 081513, 2014.

[19] J. M. Frost, K. T. Butler, and A. Walsh, “Molecular ferroelectric contributions to anomalous hysteresis in hybrid perovskite solar cells,” Apl. Mater. **2**, 081506, 2014.

[20] N. O. Yamamuro, T. Matsuo, and H. Suga, “Dielectric study of $CH_3NH_3PbX_3$ (X=Cl, Br, I),” J. Phys. Chem. Solids. **53**, 935–939 , 1992.

[21] W. Siemons, M. A. Mcguire, V. R. Cooper, M. D. Biegalski, I. N. Ivanov, G. E. jellison, L. Al Boatner, B. C. Sales and H. M. Christen, “Dielectric-constant-enhanced Hall mobility in complex oxides,” Adv. Mater. **24**, 3965–3969, 2012.

[22] D. Li, G. Wang, H. C. Cheng, C. Y. Chen, H. Wu, Y. Liu, Y. Huang, and X. Duan, “Size-dependent phase transition in methylammonium lead iodide perovskite microplate crystals,” Nat. Commun. 7, 11330, 2016.

[23] F. Li, C. Ma, H. Wang, W. Hu, W. Yu, A. D. Sheikh, and T. Wu, “Ambipolar solution-processed hybrid perovskite phototransistors,” Nat. Commun. 6, 8238, 2015.

[24] J. Zaumseil, and H. Sirringhaus, “Electron and ambipolar transport in organic field-effect transistors,” Chem. Rev. 107 (4), 1296-1323, 2007.

[25] J. M. Azpiroz, E. Mosconi, J. Bisquert, and F. D. Angelis, “Defect migration in methylammonium lead iodide and its role in perovskite solar cell operation,” Energ. Environ. Sci. 8 (7) 2118-2127, 2015.

[26] S. P. Senanayak, B. Yang, T. H. Thomas, N. Giesbrecht, W. Huang, E. Gann, B. Nair, K. Goedel, S. Guha, X. Moya, and C. R. McNeill, “Understanding charge

transport in lead iodide perovskite thin-film field-effect transistors," Sci. Adv. 3 (1) e1601935, 2017.

[27] H. Meyer, D. Haarer, H. Naarmann, and H. H. Hörhold, "Trap distribution for charge carriers in poly (paraphenylene vinylene) (PPV) and its substituted derivative DPOP-PPV," Phys. Rev. B 52 (4) 2587, 1995.

[28] R. G. Kepler, P. M. Beeson, S. J. Jacobs, R. A. Anderson, M. B. Sinclair, V. S. Valencia, and P. A. Cahill, "Electron and hole mobility in tris (8-hydroxyquinolinolato-N1, O8) aluminum," Appl. Phys. Lett. 66 (26) 3618-3620, 1995.

[29] E. Lebedev, T. Dittrich, V. P. Koch, S. Karg, and W. Brütting, "Charge carrier mobility in poly (p-phenylenevinylene) studied by the time-of-flight technique," Appl. Phys. Lett. 71 (18) 2686-2688, 1997.

[30] S. Naka, H. Okada, H. Onnagawa, J. Kido, and T. Tsutsui, "Time-of-flight measurement of hole mobility in aluminum (III) complexes," Jpn. J. Appl. Phys. 38 (11 A), L1252, 1999.

[31] M. Kitamura, T. Imada, S. Kako, S. and Y. Arakawa, "Time-of-flight measurement of lateral carrier mobility in organic thin films," Jpn. J. Appl. Phys. 43 (4S), 2326, 2004.

[32] P. M. Borsenberger and D. S. Weiss, "Organic photoreceptors for imaging systems," New York: Dekker, Inc., 280-281, 1993.

[33] H. Scher and E. W. Montroll, "Anomalous transit-time dispersion in amorphous solids," Phys. Rev. B 12 (6) 2455, 1975.

[34] S. Tiwari and N. C. Greenham, "Charge Mobility Measurement Techniques in Organic Semiconductors," Opt. Quantum Electron. 41, 69–89 (2009).

[35] I. Grill, K. Handloser, F. C. Hanusch, N. Giesbrecht, T. Bein, P. Docampo, M. Handloser, and A. Hartschuh, “Controlling crystal growth by chloride-assisted synthesis: Towards optimized charge transport in hybrid halide perovskites,” Sol. Energy Mat. Sol. Cells 166, 269-275, 2017.

[36] Q Dong, Y. Fang, Y Shao, P. Mulligan, J. Qiu, L. Cao, and J. Huang, “Electron-hole diffusion lengths > 175 μm in solution-grown $CH_3NH_3PbI_3$ single crystals,” Science 347 (6225), 967-970, 2015.

Chapter 4

Direct observation of carrier transport by photoluminescence imaging

4.1 Introduction

To investigate the fundamental optical and electrical properties of the organic-inorganic hybrid perovskites, direct observation of carrier injection from the electrode and its transport would be essential for further understanding of the carrier behavior in the perovskite devices. [1,2] We have already developed a unique technique to probe the electric field based on EFISHG measurement [3,4]. However, the perovskite materials show the multi-photon excited fluorescence, and it may sometimes interfere with the weak SHG signal during the SHG measurement. On the other hand, it is known that PL is quenched under the presence of charges owing to the exciton-polaron annihilation. [5, 6] These motivated us to study the carrier transport in the perovskite materials on the basis of the real-time transient PL imaging.

In this chapter, we conducted the transient PL imaging to discuss carrier behavior in the one-step and two-step solution processed $CH_3NH_3PbI_3$ perovskite thin films and room temperature and low temperature, and it was revealed that PL imaging can provide direct insight into the nature of charge carriers such as the mobility, ion migration and surface defects, etc. For this purpose, we focused our attention on utilizing perovskite materials in transistor structure also because we could clearly observe the carrier behavior from the top of the FET. [1]

4.2. Experimental section

4.2.1. Fabrication of perovskite films

Here, we used a simple deposition method; the one-step and two-step spin-coating, for the deposition of $CH_3NH_3PbI_3$ perovskite thin films. For the detail sample preparation and characterization, see in subsection 2.6.2.2. Here we used top contact bottom gate FET structure for PL imaging measurement. As descried in this section, although the morphology of our fabricated thin film was still need for improvement, one-step and two-step films were worth to discuss the validity for the visualization of carrier motion in perovskite film for our studies. Relevant SEM and XRD characteristics of the fabricated film were the same with the previous FET and TOF experiments. Figure 4.1 is absorbance and luminescence spectrum of fabricated perovskite film.

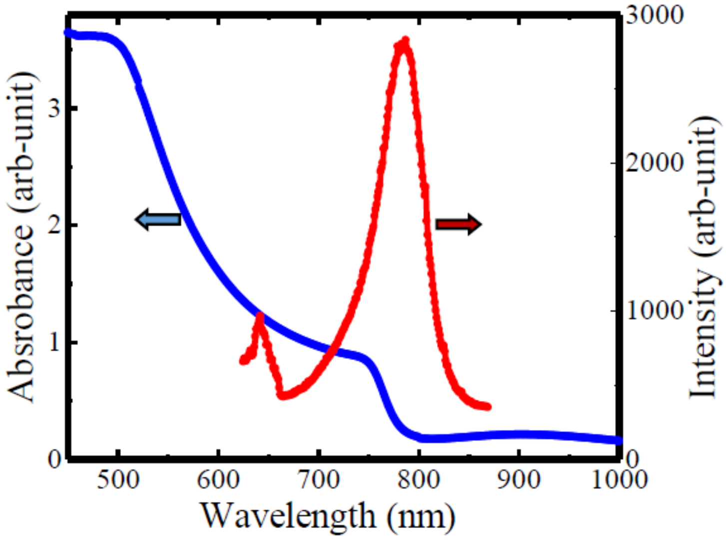

Figure 4.1: Absorbance and luminescence spectrum of perovskite film

Figure 4.1. shows the absorption and PL spectrum of the two-step fabricated perovskite film. PL spectrum was observed under the laser excitation at 532 nm. The spectral overlap at the wavelength around 760 nm may make it difficult to perform the

EFISHG measurement due to the interference of two-photon excited PL and SHG signal. Therefore, we conducted to visualize the carrier behavior by using PL quenching firstly.

4.3 PL phenomena

Transient PL imaging is easy and facile way to investigate the charge transport by utilizing attenuation of light emission intensity. PL takes place when the excited state produced by photo irradiation goes back to the ground state. However, excitons may dissociate under the electric field because of the large dielectric constant of perovskite materials, and the energy of excited molecule may transfer to the charged molecule under the presence of injected charges according to the Forster transition.

How can we extract the electrical parameter from optical measurement? When electric field is applied to the electrode, changing of transient PL image at perovskite layer by charge injection was captured by CCD camera after filter. For that case, there were two phenomena, carrier injection and extraction. PL intensity would be decreased when the carrier density increased whereas PL intensity would be enhanced when the carrier density decreases. Then if we knew the transport distance x, applied voltage V and the time delay for those distance x, t, we could estimate the carrier mobility μ by the Eq. 4.1 as already explained in subsection 2.6.1[7].

$$\mu = \frac{x^2}{2vt} \tag{4.1}$$

4.4 Analysis of origin of PL image in perovskite materials

First of all, we need to consider the mechanism of the origin of PL quenching generated from perovskite materials. For confirmation, we fabricated two types of devices as shown in Fig. 4.2 (a) and (b). For both devices, the perovskite film was prepared on a glass substrate by using same fabrication method described at subsection 2.6.2.2. Then for insulating PMMA layer, 74mg/ml in PMMA/ butyl acetate dehydrated solution was spin coated for 2500rpm in 60s for insulating layer. Finally, for source and drain electrodes, Au was deposited by evaporation through a shadow mask.

4.4.1 I-V characteristics with PMMA and without PMMA

Firstly, we conducted I-V characteristics measurement for fabricated devices to check the conduction current for relevant thickness of PMMA. Figure 4.2 (c) shows the I-V characteristics for the device with and without PMMA.

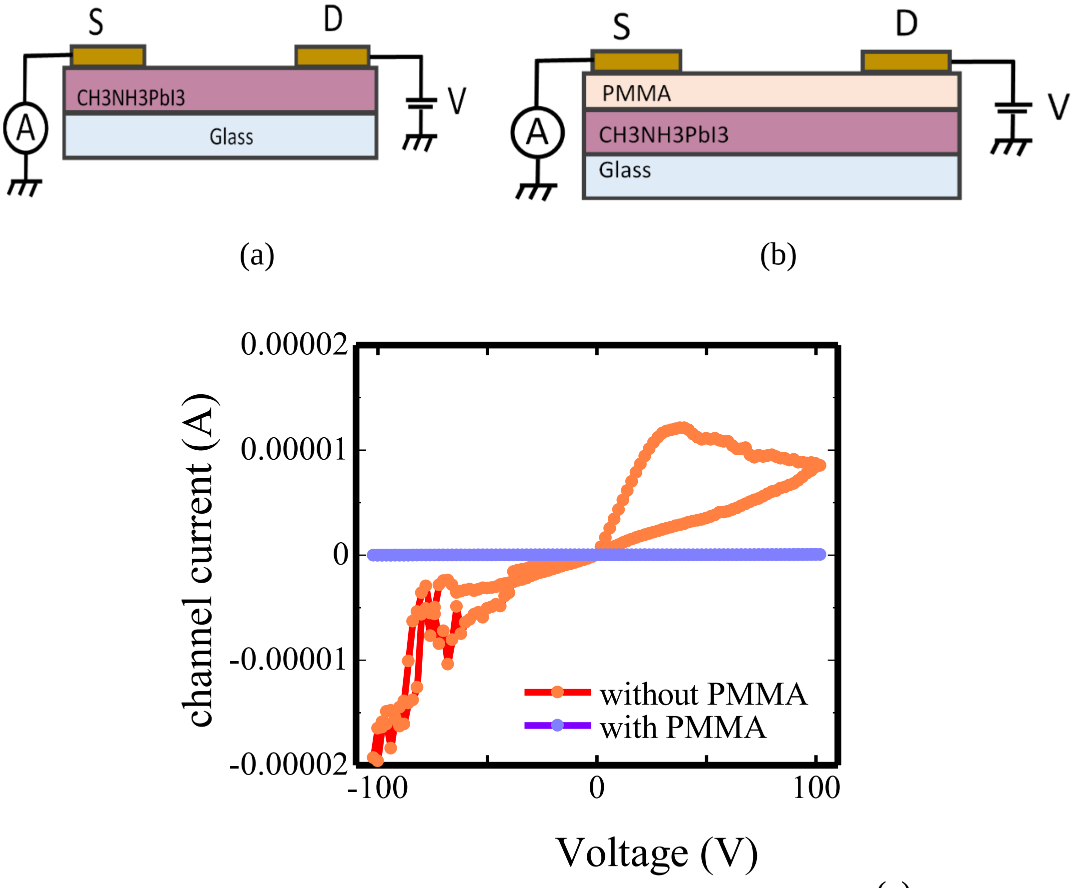

(a) (b)

(c)

Figure 4.2: Side view and electrical connection for I-V characteristics of the device (a) without PMMA (b) with PMMA (c) I-V characteristics for both devices

Base on the IV characteristics, PMMA completely covered for the perovskite film. There was negligible current for with PMMA device as shown in Fig. 4.2 (c).

4.4.2 Observation of PL image for perovskite

As shown in Fig. 4.2 (a) and (b), the difference in these devices was with or without PMMA layer between the perovskite layer and gold electrode. PMMA layer was used to prevent the carrier injection from the gold electrode so that only the electric field was applied to the perovskite layer. Experimantal setup for the observation of PL image for perovskite is shown in Fig. 4.3 (a).

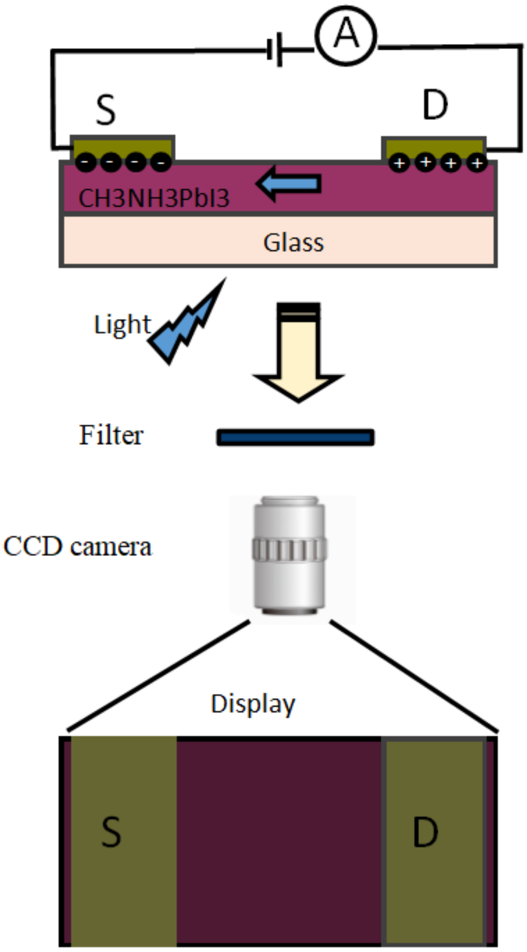

(a)

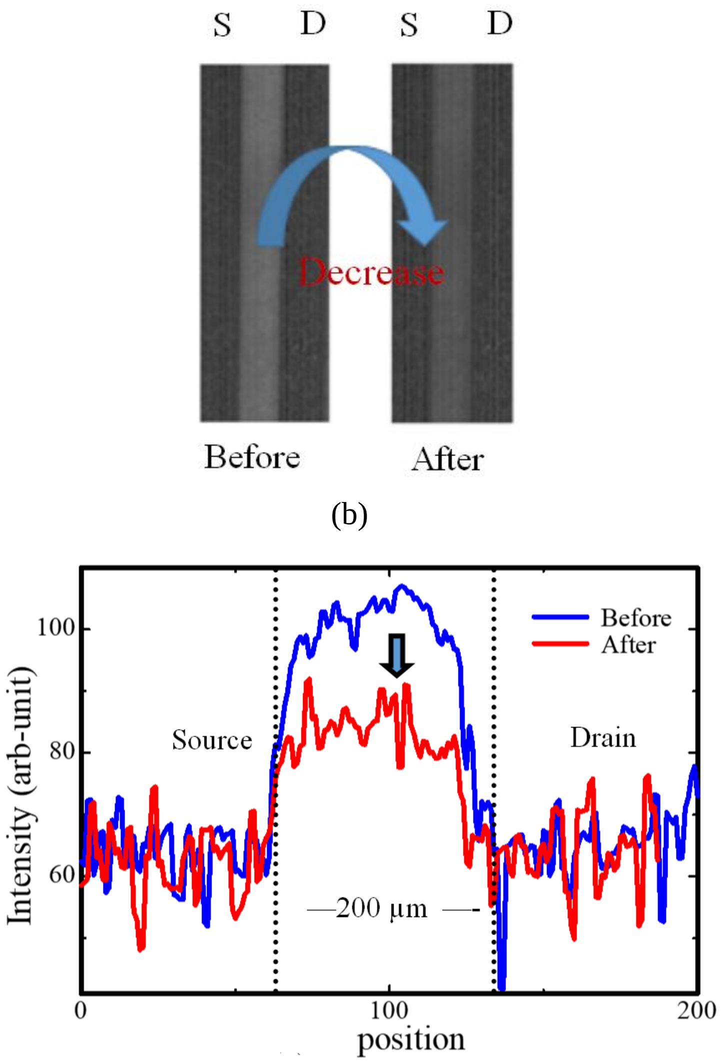

(b)

(c)

Figure 4.3: (a) Experimental setup of observation of mechanism (b) Top view of transient image of the fabricated film without PMMA on the glass substrate from top view (c) PL intensity distribution replotted from (b).

We analyzed the transient PL image during voltage application under illumination. Fig. 4.3 (b) dispicts the raw image of the fabricated film without PMMA on the glass substrated from top view and (c) illustrates PL intensity distribution replotted from the raw image. As shown in Fig. 4.3 (c), PL intensity clearly decreased between the electrodes after the application of voltage. Conductive current was observed for the device without PMMA layer, indicating the injected carriers transported in the perovskite layer between the electrodes. At the same time, the electric field could form between the electrode. This PL decay image could come not only from the injected charges but also from electric field caused by the applied voltage. We could not determine the dominant contribution of the PL quenching from only one experimental result because we would like to confirm the mechanism of perovskite layer for PL quenching ; such as charge distribution or electric field distribuiton. Therefore, we used the sample with PMMA device also as shown in Fig. 4.2. (b) and results are shown in Fig. 4.4. (a) and (b).

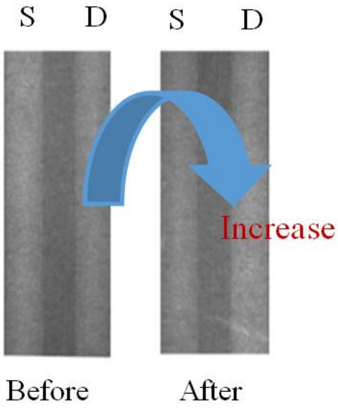

(a)

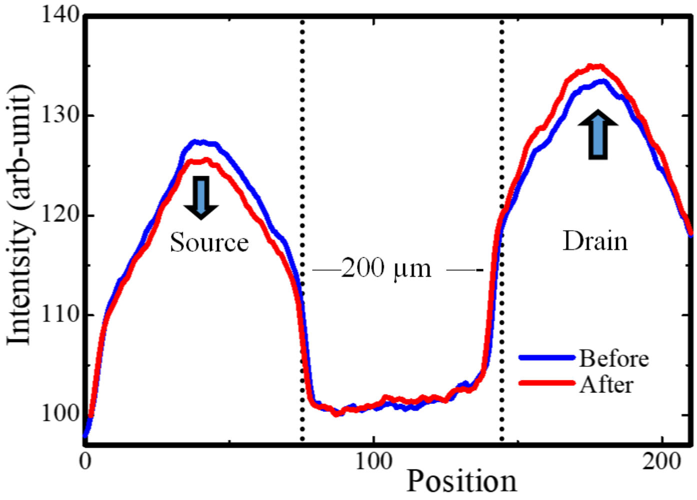

(b)

Figure 4.4: (a) Top view of transient image of the fabricated film without PMMA on the glass substrate from top view (b) PL intensity distribution replotted from (b).

For the device with PMMA, there was no change between electrode under applied voltage. Because, there was negligible injected carrier between the electrode under the application of the voltage for the device with PMMA, whereas the electric field still formed between the electrodes. It should be noted that the PL intensity slightly changed under the electrodes for the device with PMMA layer. This was presumably due to the change in the distribution of intrinsic carrier under the presence of the electric field. This experiment revealed that injected charges were most responsible for the PL quenching of the perovskite layer. Later we will demonstrate he charge transport process in perovskite thin film to be successfully visualized through the PL imaging.

4.5 Experiment of PL decay image

Investigation of the PL quenching is also a useful tool to study charge separation and to get information on interfacial contacts. This section focused the measurement of PL decay imaging. For the detail of the setting of experiment, see the subsection 2.6.1.1. At first, we tried to capture the video image for PL quenching process. Under light illuminaton, we saw very fast response after the application of voltage. Therefore, we considerd to use high speed camera to capture the diescrete images for detail investigations. Then we can analyze the time dependent fluorescence images.

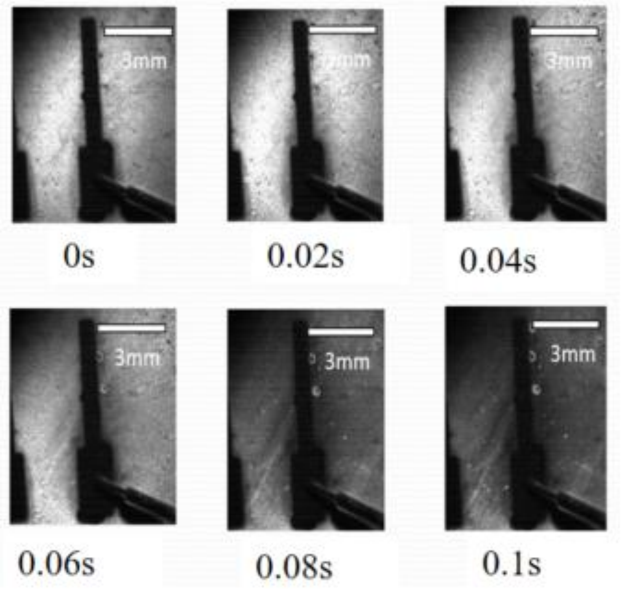

(a)

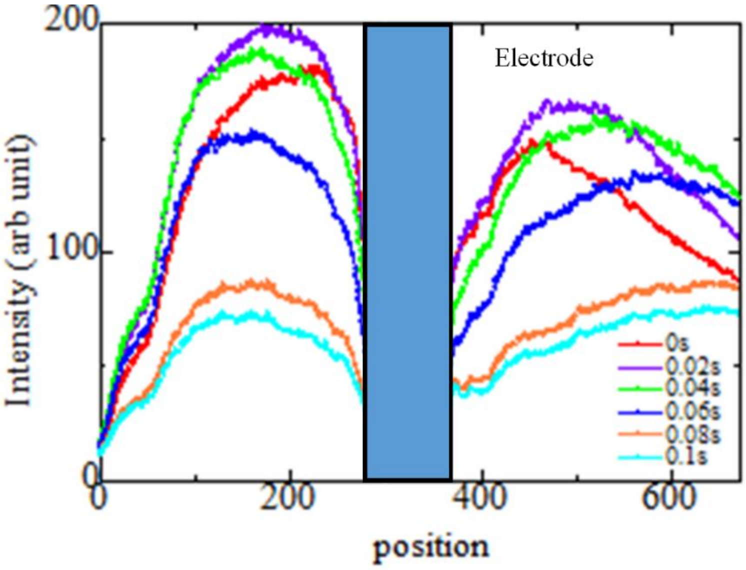

(b)

Figure 4.5: (a) Time dependent fluorescence images (b) replotted light intensity profile of time dependent fluresence images in Fig. (a)

Figure 4.5 (a) and (b) repersent the transient PL images at the elapsed time of 0 s, to 0.1 s and the replotted light intensity profile from Fig. 4.5 (a). These transient images was taken 50 frames per second, thus, the time delay for one image took 0.02

s. Indeed, the transient response of the pervskite film could be less than 0.02 s. However, we could see the transeint fluorescent images from 0.02 s period. At 0 s, we started the applied electric field by giving -100 V to the electrode. Interestingly, we could clearly see , the highest enhancement of PL spreaded from source electrode after 0.02 s as shown in Fig. 4.5 (a) and (b). The light intensity still then decreased gradually. That implied two-step PL quenching phenomena. The first enhancement of PL was probably due to extraction of intrinsic holes (suddenly reduced the charges) from the thin film of perovskite. After that because of the motion of charge ions by electric field, its intensity was slightly decreased. By analyzing the transient images from the PL imaging measurement, two steps changing of PL could be confirmed. The fast PL decay corresponded to the carrier (hole/ electron) transport phenomena .The slow PL decay was possibly due to the migration of intrinsic ions in the perovskite.

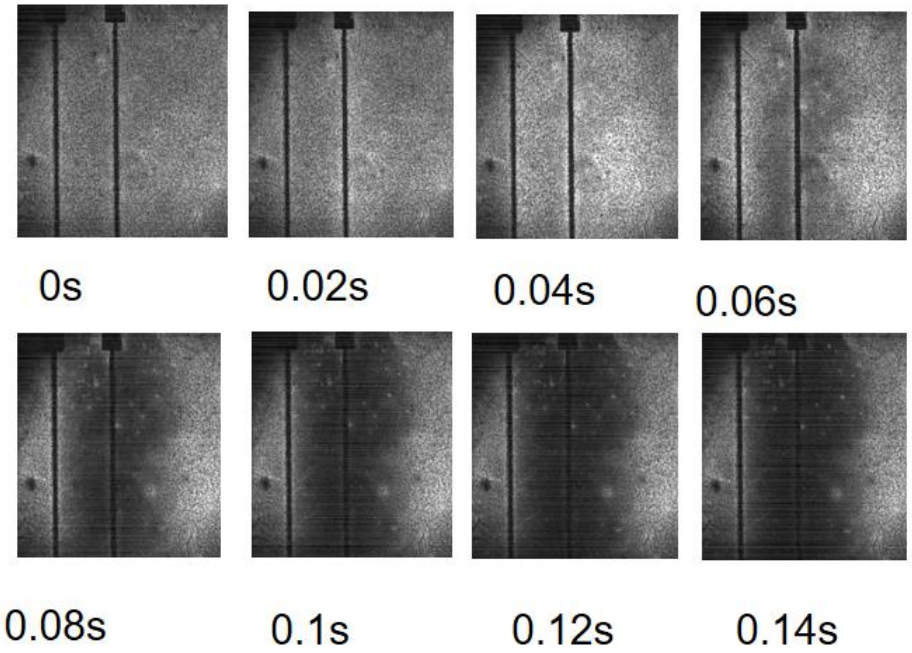

(a)

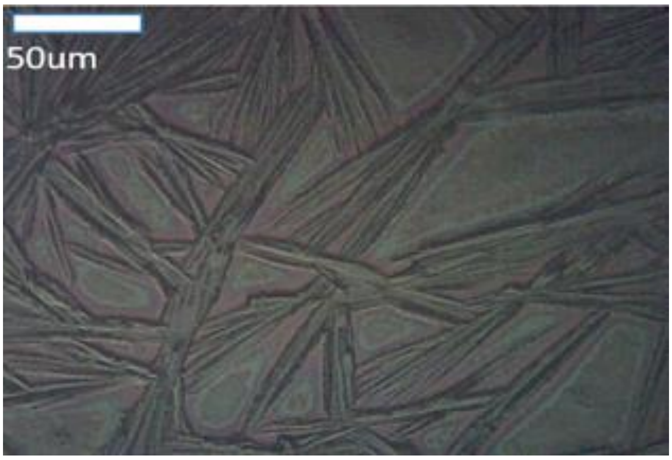

(b)

Figure. 4.6 (a) Time dependent fluorescence images for one step fabricated film with no toulene addition (b) film morphology of device for Fig. (a)

Figure 4.7 (a) and (b) show the time dependent fluourescence images and the film morphology for one setp fabricated film with no toulene addtition. Thus, large pin holes and rough film surfce clearly seen. As shown in Fig. 4.7 (a) we could clearly observe two step changing. This implied that PL quenching measurement was available regardless for morphology. According to the previous expremental results, we saw time dependent fluorescence image clearly with significant two-step PL quenching phenomena but unfortunately we could not calculate exactly the mobility of hole and electrons due to very fast response of charge injection. To confirm the transit time directly we conducted the lateral time of flight measurement as follows.

4.6 Measurement of mobility by using PL imaging

In this section, we combined the PL measurement and the lateral time of flight (e TOF) measurement to confirm that the transient PL images correspond to the carrier motion and the transit time directly. Therefore, we used FET structure based on silicon substrate with long channel length of 6.8 mm as shown in Fig. 4.7. Fig. 4.8 illustrates the experimental setup for PL imaging. Then we conducted the direct visualization experiment for the carrier motion through the transient change in the PL images by using the CCD camera as shown in Fig. 4.8.

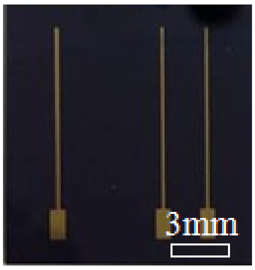

Figure 4.7: Typical photo of top contat electrode on Si substrate

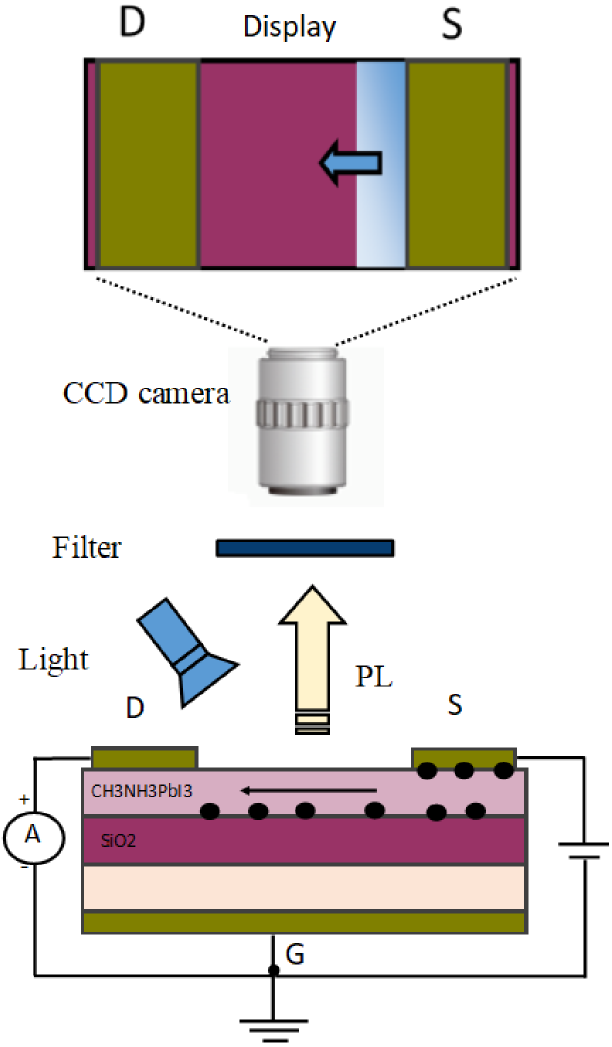

Figure 4.8: Expiremental set up for photoluminescene imaging

Fig. 4. 9 (a) represents the transient PL images at the elapsed times of 0 s, 0.02 s, 0.04 s, and 0.06 s after applying voltage. At the time of 0 s, the voltage application started. At the time of 0.02 s, increase of the PL intensity was observed at the source side. This indicated the decrease of the carrier concentration near the source electrode implying the extraction of intrinsic holes from the perovskite layer.

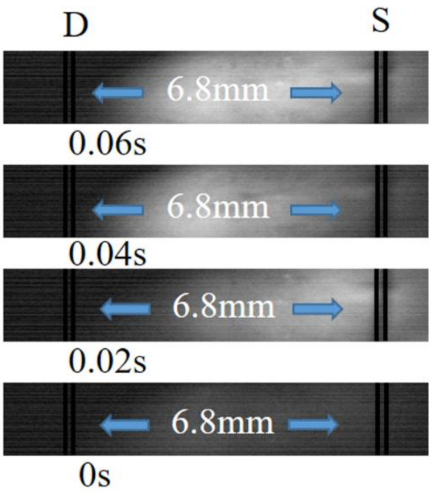

(a)

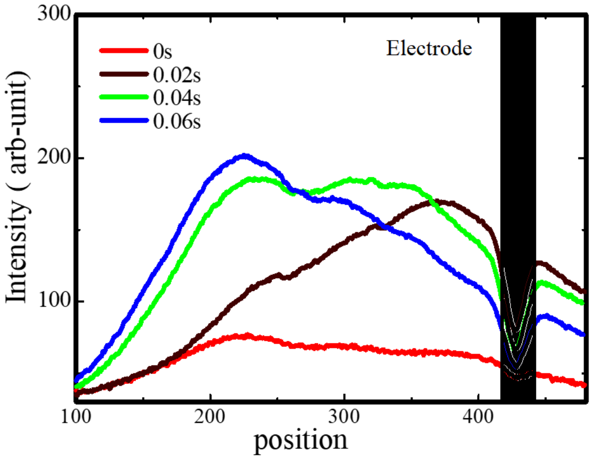

(b)

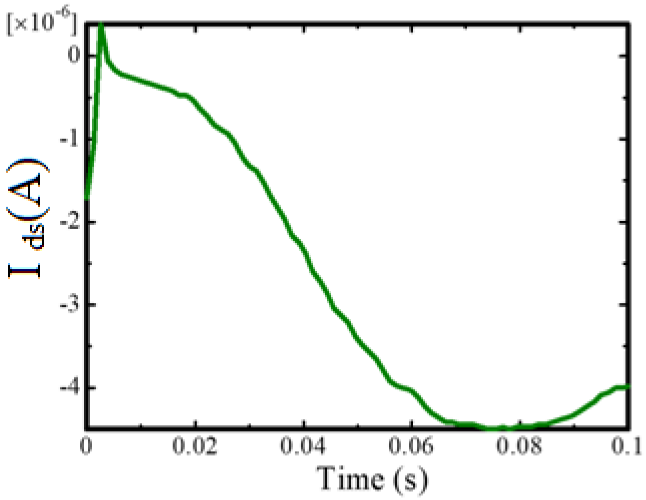

(c)

Figure 4.9: (a) Time dependent PL images (b) time evolution of PL intensity distribution calculated from the transient PL images (c) transient current observed at the drain electrode.

As increasing the time, bright PL area spread in the channel to the drain side. Figure 4.9 (b) represents the time evolution of the PL intensity profile re-plotted from the transient PL images. For the lateral TOF measurement, drain current was recorded while capturing the transient PL images with a time interval of 0.02 s. Figure 4.9 (c) shows the corresponding transient current observed at the drain electrode, and the current gradually increased and reached the maximum value at 0.06 s. Thus, it was reasonable to conclude that the transient PL decay images correspond to the carrier motion. It should be noted that even though the steady state drain current was not observed in the I-V characteristics for FET at room temperature due to the screening effect of the ion [8], the transient current for PL images could be observed at the room temperature because transient current comes from the holes without in screening.

We calculated hole mobility as $2.3 \times 10^{-2}\ \mathrm{cm^2V^{-1}s^{-1}}$ as described in Eq. (4.1) and it was important to keep in mind that this mobility represented the hole mobility because of the extraction of intrinsic holes is the origin of fast PL intensity change even though the applied bias was the negative voltage. This was much lower than the mobility measured for lateral TOF in previous chapter at room temperature. It probably due to the difference in measurement condition such as the electrode system, the excitation source and frequency and so on.

In the lateral TOF configuration using FET structure for PL quenching experiment, carrier transport was strongly influenced by surface morphology and structure of the film. The complexity of the carrier transport properties in perovskite materials was also affected by the defects, grain boundaries, and environmental effects. [9]

The two-step process based on the interdiffusion method produced the dense and uniform perovskite $CH_3NH_3PbI_3$ thin film. [10] For that case, extraction of hole rate was found to be approximately two-times higher than the one-step films. This result implied that the high coverage crystal growth and continuous morphology of the two-step fabricated film increased the device performance. Also PL imaging could provide spatial resolution of non uniform stiuation and localizzed defects as shown in Fig. 4.10.

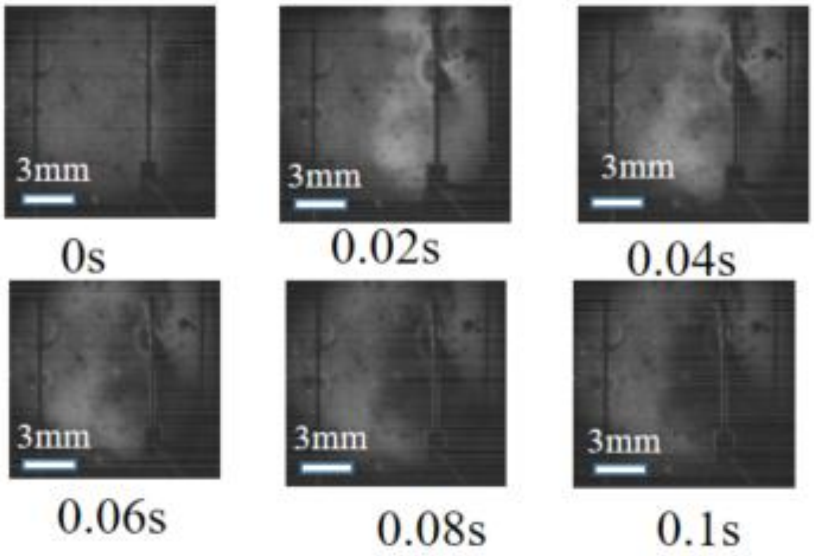

Figure 4.10: Time dependent flouoresence image for two step fabricated film and

4.7 PL image at low temperature (268K)

Here, we conducted PL measurement at low tempeature at 268 K. We observed that the effect of temperatrue also induced for PL quenching imaging and the hole mobility was estimated as 1.2 x10^{-3} cm^2/Vs at low temperature (268 K). It was consistant with the previous low temperature FET transistor mobility and less than ten times compared with PL mobiliy at room temperature.

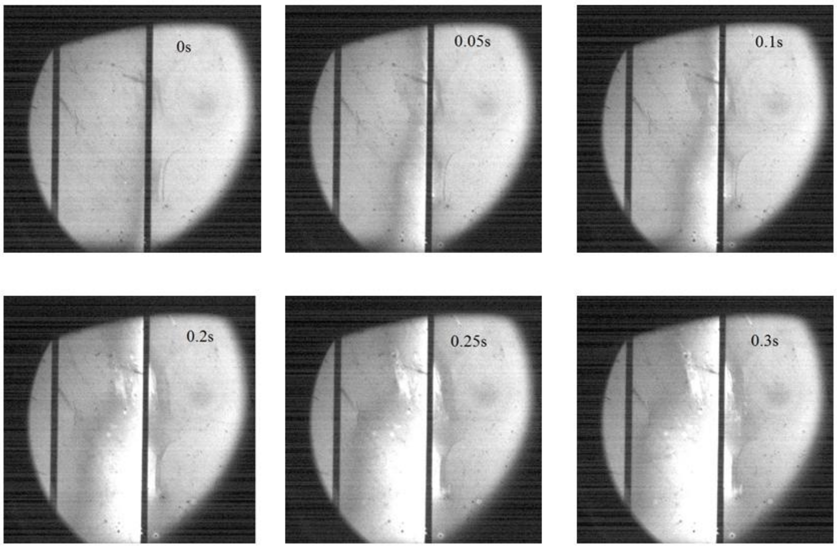

Figure 4.11: Timedependent flourescence image for low temperature.

4.8 Degradation mechanism

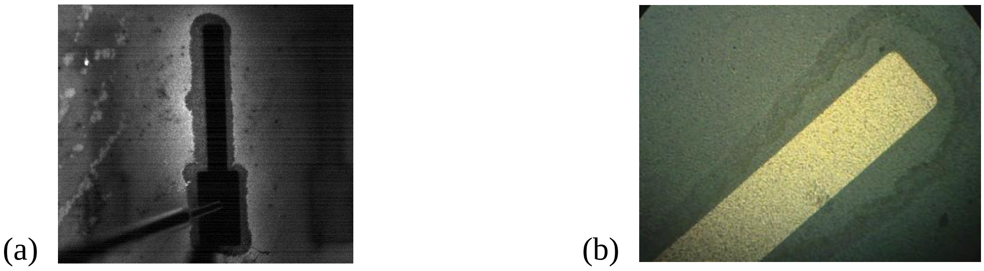

Figure 4.12: The defects after applying voltage (a) under measurement (b) optical image afte measurement

Sometimes, we could see the defects around the electrode after long time measurement and over multple cycles. It probably due to the electreic field applied in the material was non uniform because of defects of deposition. Therefore, under voltage application, this electric field concentrated at the defect made some strains for the film as shown in Fig. 4.12 (a). Moreover, it was reported for the slipping generated grain boundaries could be created by the high speed channel for ion migration under the elelctric field [11]. After the long time opration, we could see these devices under microscopic view as shwon in Fig. 4.12 (b). For investigation of this defect will be further studies.

4.9 Conclusions

Transient PL imaging technique was conducted to study the carrier transport phenomena in the perovskite thin film. Firstly, we studied the origin of PL image in perovskite materials. After that the PL quenching process was examined. PL intensity changed with respect to transient time under applied voltage. PL intensity change indicates that the electrons and holes were injected alternately from the Au electrodes depending on the applied voltage. This implies that the perovskite materials can provide ambipolar electrical properties with high luminescence efficiency.

Firstly, PL distribution in the channel region of the perovskite FET rapidly changed after applying the voltage to the source electrode. These results highlight two important properties of the materials. First, both intrinsic electrons and holes mobility are high. Due to this mobility and long diffusion length, charges quickly diffuse through the perovskite material. Second, mobility for electrons and holes are quite similar. The perovskite material provide easy injection and transport of both electrons and holes, together with very high luminescence efficiency.

Then, we found the two step PL phenomena for perovskite materials. First fluorescent was very fast which means highly efficient charge transfer in the material. After that we could see next step for PL decaying, this observation suggests that there was a large ions to lower energy sites as a function of time delay after excitation.

Finally, we analyzed the carrier mobility by combining two methods of PL and e TOF measurement. By combining with the e-TOF measurement, we could confirm that the transient PL imaging corresponded to the transient carrier motion. The PL enhancement from the source electrode indicated the extraction of intrinsic holes. This implies that the intrinsic holes predominantly exist throughout the spin-coated perovskite film. Hole mobility is evaluated as $2.3 \times 10^{-2}\ \mathrm{cm^2V^{-1}s^{-1}}$ by analyzing the transient PL images. Based on the studies, we concluded the fabricated perovskite film was available for PL quenching measurement and the mobility is consistent with the other Si based no modification substrate. And intrinsic ions are spreading throughout the film.

Discriminate evaluation of the carrier and ion current was quite important to discuss the fundamental electrical transport properties of perovskite materials. Future work on the transport phenomena in field effect devices will be a fruitful complement to optimize the application of perovskite devices.

Bibliography

[1] T. Manaka, E. Lim, R. Tamura, and M. Iwamoto, “Direct imaging of carrier motion in organic transistors by optical second-harmonic generation,” Nat. Photon. 581-584, 2007.

[2] T. Manaka and M. Iwamoto, “Optical second-harmonic generation measurement for probing organic device operation,” Light Sci. Appl. 5 (3) 16040, 2016.

[3] T. Manaka, E. Lim, R. Tamura, and M. Iwamoto, “Modulation in optical second harmonic generation signal from channel of pentacene field effect transistors during device operation,” Appl. Phys. Lett. 87 (22) 222107, 2005.

[4] T. Manaka, E. Lim, R. Tamura, D. Yamada, and M. Iwamoto, “Probing of the electric field distribution in organic field effect transistor channel by microscopic second-harmonic generation,” Appl. Phys. Lett. 89 (7) 072113, 2006.

[5] S. Hayashi, K. Kaneto, and K. Yoshino, “Quenching of photoluminescence in poly (thiophene) films by electrochemical doping,” Solid state commun. 61 (4) 249-251, 1987.

[6] P. Dyreklev, O. Inganäs, J. Paloheimo, and H. Stubb, “Photoluminescence quenching in a polymer thin-film field-effect luministor,” J. Appl. Phys. 71 (6) 2816-2820, 1992.

[7] E. L. Unger, E. T. Hoke, C. D. Bailie, W. H. Nguyen, A. R. Bowring, T. Heumüller, M. G. Christoforo, and M. D. McGehee, “Hysteresis and transient behavior in current–voltage measurements of hybrid-perovskite absorber solar cells,” Energ Environ. Sci. 7 (11) 3690-3698, 2014.

[8] X. Y. Chin, D. Cortecchia, J. Yin, A. Bruno, and C. Soci, “Lead iodide perovskite light-emitting field-effect transistor,” Nat. commun. 6, 7383, 2015.

[9] Q. Dong, Y. Fang, Y. Shao, P. Mulligan, J. Qiu, L. Cao, and J. Huang, “Electron-hole diffusion lengths > 175 μm in solution-grown $CH_3NH_3PbI_3$ single crystals,” Science 347 (6225) 967-970, 2015.

[10] Z. Xiao, Q. Dong, C. Bi, Y. Shao, Y. Yuan, and J. Huang, “Solvent annealing of perovskite-induced crystal growth for photovoltaic-device efficiency enhancement,” Adv. Mater 26 (37) 6503-6509, 2014.

Chapter 5

Carrier visualization of organic-inorganic hybrid perovskite thin films by using time-resolved microscopic second-harmonic generation (TRM-SHG)

5.1 Introduction

Detailed information on carrier dynamics by direct observation of the carrier injection from electrode and its transport would be beneficial for understanding the complex carrier behavior in the perovskite devices [1, 2]. In our laboratory, we successfully developed a unique technique to visualize the electric field based on the time-resolved microscopic optical second-harmonic generation (TRM-SHG) measurement [3, 4]. TRM-SHG can provide direct insight into the nature of carriers and the electric field distribution with its time dependence. This technique is also suitable to study the fundamental properties of the perovskite-based device, through the visualization of the carrier transport and polarization structure in the perovskite layer. However, the perovskite materials show the multi-photon excited fluorescence, and spectral overlap between the two-photon excited PL and the SHG makes challenging to perform SHG measurement [4]. Here, we introduced the application of TRM-SHG technique to visualize the complex carrier behavior in perovskite. We focused on the transient carrier behavior in the channel of FET so that we can clearly observe the carrier behavior from top of the FET structure. The TRM-SHG imaging visualizes the transient electric field migration caused by traveling carriers and thus, the carrier mobility was directly evaluated. Furthermore, TRM-SHG technique was also employed to investigate the behavior of traps on transient carrier transport in the channel of perovskite FET. Time-resolved experiment was performed by synchronizing the laser pulses and the voltage pulses applied to the FET.

TRM-SHG measurement is one of the most versatile techniques for evaluating the fundamental electrical properties of this new class of solar cell materials. Carrier transport and concentration of trap had also been investigated by means of EFISHG technique [5]. The presence of trapping states influences the device performance such as carrier mobility and hysteresis behavior in current-voltage characteristics [6]. In this chapter, TRM-SHG measurements were conducted to visualize the carrier motion and to investigate the concentration of trap in perovskite thin films.

5.2 Experimental section

5.2.1 Fabrication and characterization of perovskite films

Here, we utilized a simple deposition method; the one-step and two-step spin coating for the deposition of $CH_3NH_3PbI_3$ perovskite thin films. For the detail sample preparation and characterization, see in subsection 2.6.2.2. Here we used top contact bottom gate FET structure with Si substrate and glass substrate was used for observing the SHG spectrum. Relevant SEM and XRD characteristics of the fabricated film were the same with the previous experiments.

5.2.2 SHG spectrum from perovskite thin film

EFISHG is a technique that enables us to prove the propagation of the dielectric polarization induced by electrons and holes which are moving in the organic materials, where nonlinear polarization induced by coupling with incident electromagnetic waves, e.g., laser light and the dc electric field generated from moving carriers, can be proved in real time [1, 7]. Figure 5.1 shows the typical set up of SHG spectrum.

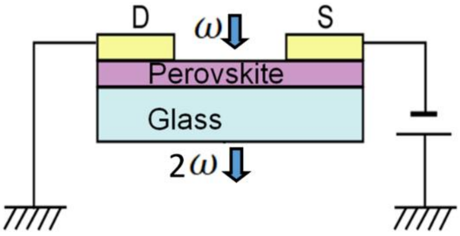

Figure 5.1: Typical set up of SHG spectrum.

First, we had to find out the proper wavelength for the SHG measurement because the SHG intensity is resonantly enhanced at specific wavelength and use of an appropriate wavelength makes it easy to visualize the carrier motion of target materials [8]. According to the simple consideration for the resonant condition of the EFISHG process, the resonant enhancement will occur when the fundamental or the SH wavelength coincides with the bandgap.

Thus, selecting an appropriate wavelength is important to observe the SHG signal from perovskite effectively, because the SHG intensity strongly depends on materials itself and fundamental wavelength used. To find out the appropriate wavelength, SHG spectrum was measured from 1500 to 1600 nm. The SHG peak could be observed near the peak of photoluminescence as shown in Fig. 5.2 (a). Figure 5.2 (a) shows the absorbance, PL and SHG spectrum of the perovskite material with and without applying voltage. On the other hand, perovskite materials also show multi-photon excited fluorescence. In addition, this spectral overlap of photoluminescence (PL) signal and the SHG is serious issue to perform the SHG measurement.

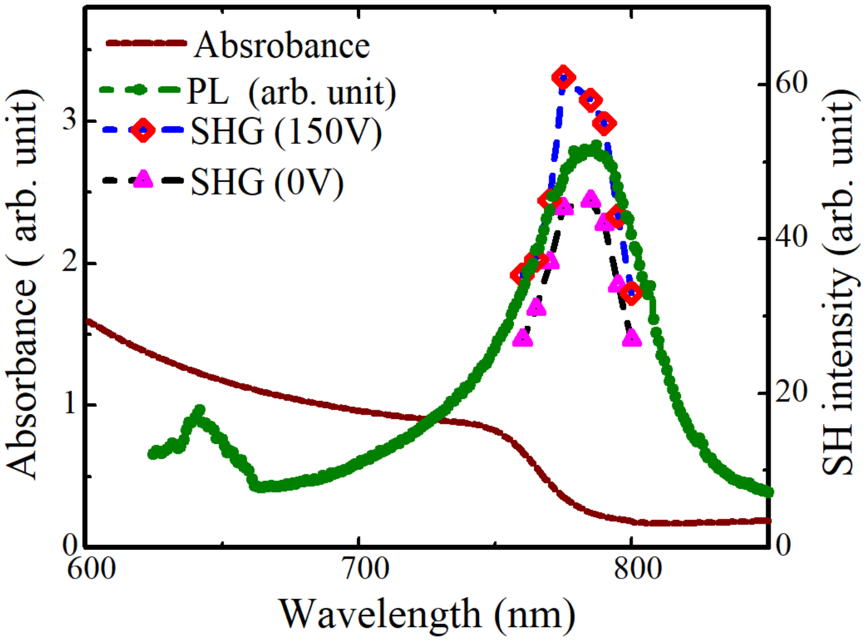

(a)

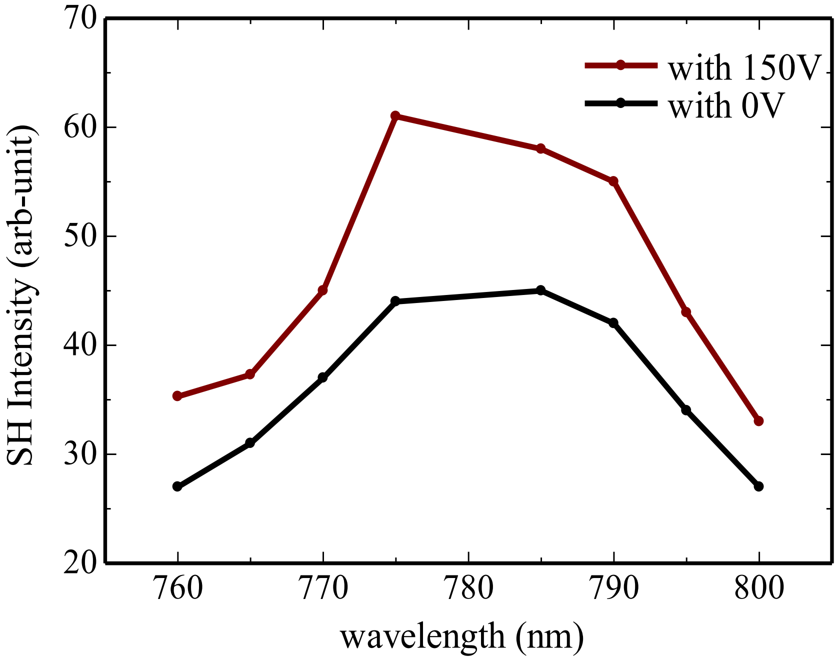

(b)

Figure 5.2 (a): Optical absorption and SHG spectra of perovskite film (b) SHG intensity for different wavelength with applied positive voltage 150 V (red line) and without applying voltage (black line).

Furthermore, the signal was observed even without the voltage application, but the intensity obviously increased under the voltage application. It seemed that the peak position with voltage application was slightly blue shifted compared to that without voltage. This was due to the difference in the peak position of SHG and PL spectrum. Under the voltage application, the observed signal at around 780 nm presumably consisted of the PL and the EFISHG signal. The observed signal without voltage application was assigned to the two-photon-excited PL, and PL peak moved slightly red shift due to strokes shift.

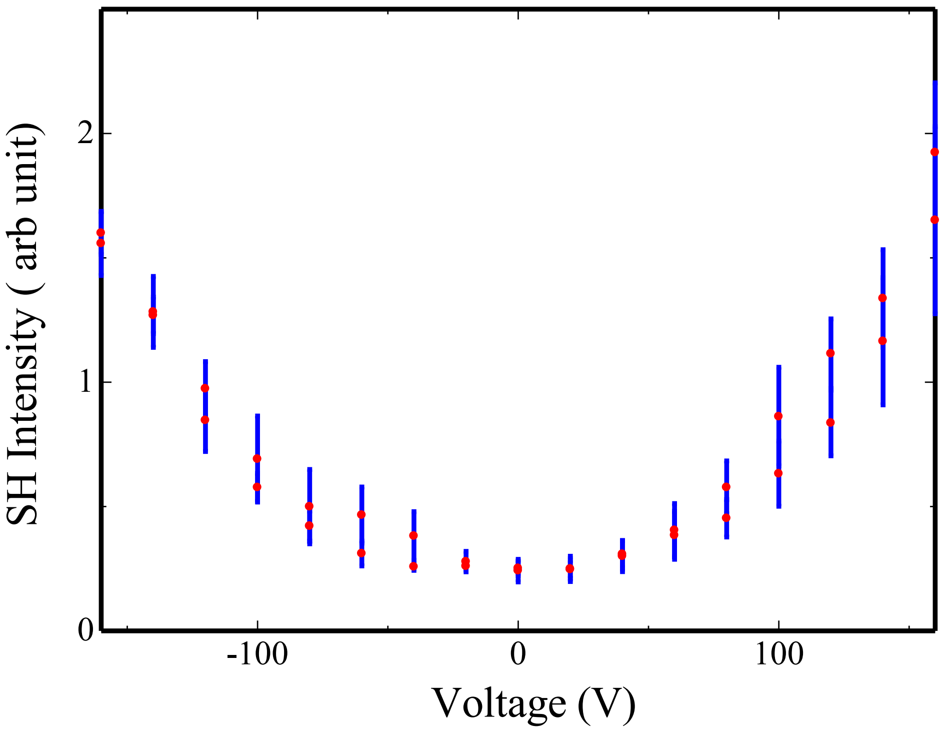

Figure 5.3: SHG intensity dependence on the external electric field strength from -150 V to +150 V at the wavelength of 780 nm. Blue lines are error bars for five repeat time.

To further clarify the origin of the SHG signal at around 780 nm under the voltage application, the voltage dependence measurement was conducted with fixed wavelength at 1560 nm. Figure 5.3 shows the voltage dependence of the SHG intensity at the SH wavelength of 780 nm, and we could observe V^2 dependence of the SHG intensity at this wavelength. Observation of the V^2 dependence clearly indicated the EFISHG process. For SHG measurement of perovskite materials, the proper fundamental wavelength of the SHG measurement was fixed at 1560 nm. It had been revealed that we could directly investigate the electric field in $CH_3NH_3PbI_3$ perovskite materials by using this wavelength; EFISHG measurement was available as a novel technique to study the carrier motion in perovskite materials.

5.2.3 Carrier behavior and visualization of TRM-SHG

Figure 5.4 (a) represents the schematic image of the sample structure and electrical connection used in the TRM-SHG experiment. Fig. 5.4. (b) illustrates the timing chart of the applied pulse voltage and incident laser light in the TRM-SHG measurement, where t_d is a delay time between the rising edge of the voltage and the laser pulse. For more details of experimental set up, see subsection 2.6.2.2.

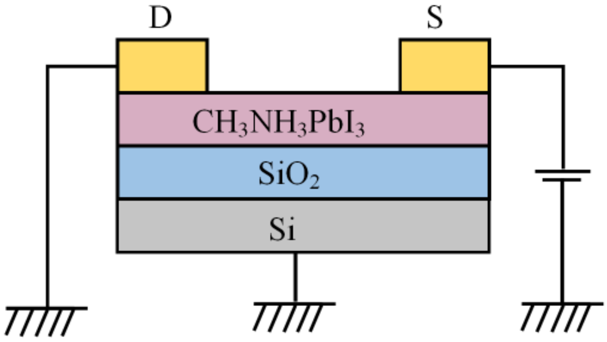

(a)

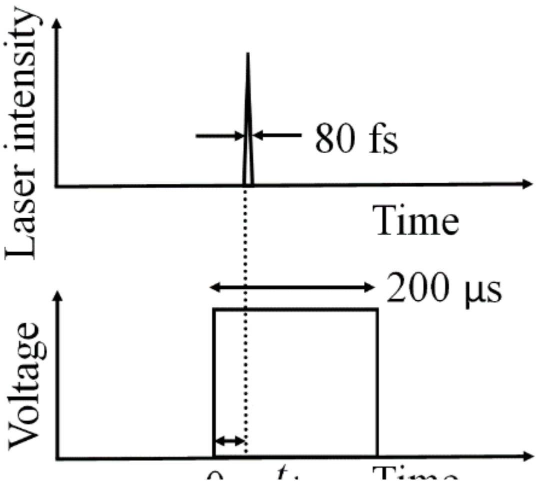

(b)

Figure 5.4: (a) Schematic diagram of the top contact FET device and electrical connection (b) Timing chart of the voltage pulse applied to the FET and the laser pulse.

For time evolution of the electric field distribution in the channel, we had to set the delay time $t_{d.}$ Here we used the time delay from 0 to 5 μs. The pulse voltage was applied to the source electrode, and the gate and drain electrodes were connected to ground as shown in Fig. 5.4 (a). The pulse width, repetition rate, and applied voltage to the FET were 100 μs, 1 kHz and 100 V, respectively. Fundamental light was focused onto the channel region of the FET with normal incidence and the spot size was approximately 150 μm and the fundamental light almost uniformly irradiated across the channel. Finally, SH light was detected by a CCD camera. All measurements were performed in ambient laboratory atmosphere.

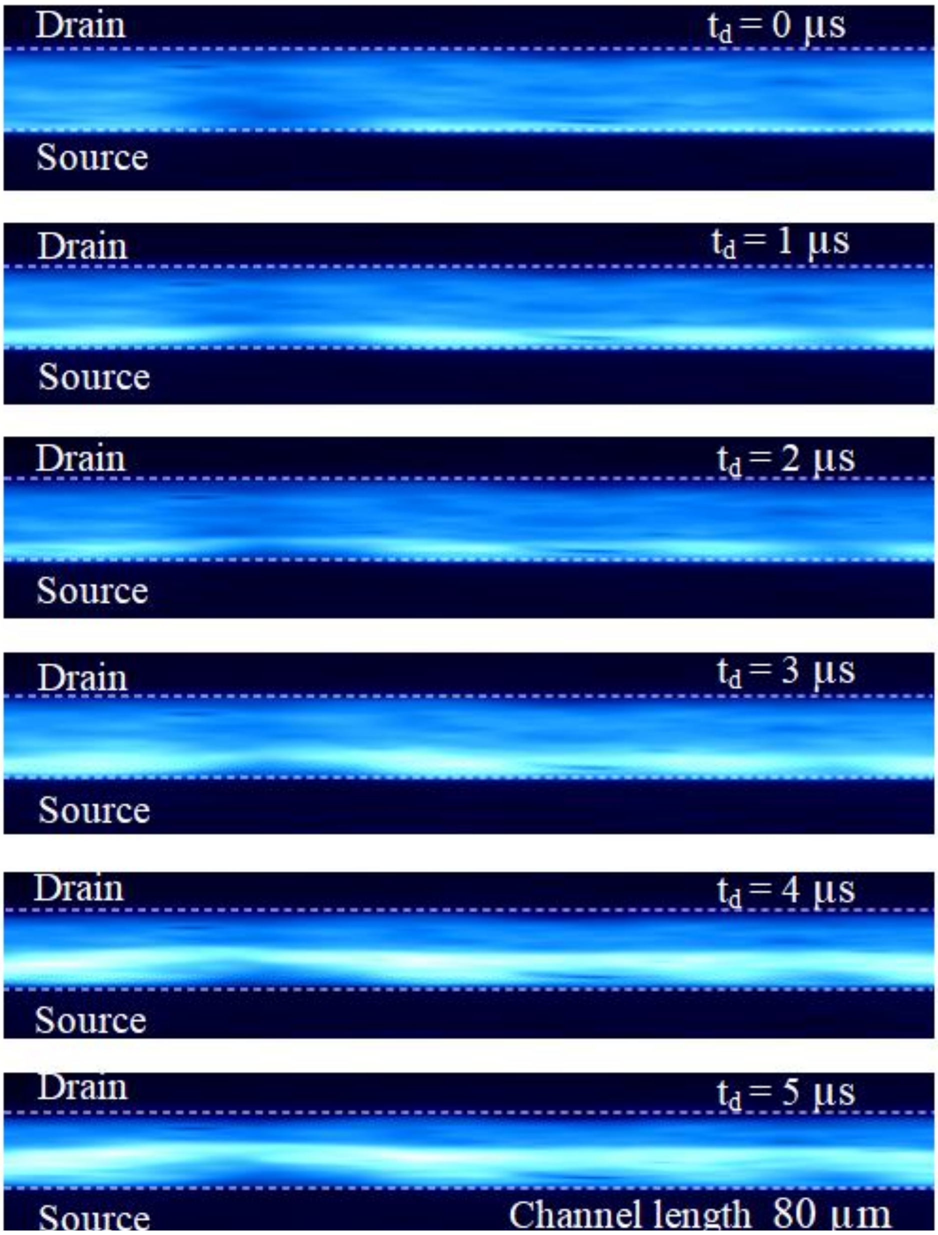
Drain
t_d = 0 µs
Source
Drain
t_d = 1 µs
Source
Drain
t_d = 2 µs
Source
Drain
t_d = 3 µs
Source
Drain
t_d = 4 µs
Source
Drain
t_d = 5 µs
Source
Channel length 80 µm

(a)

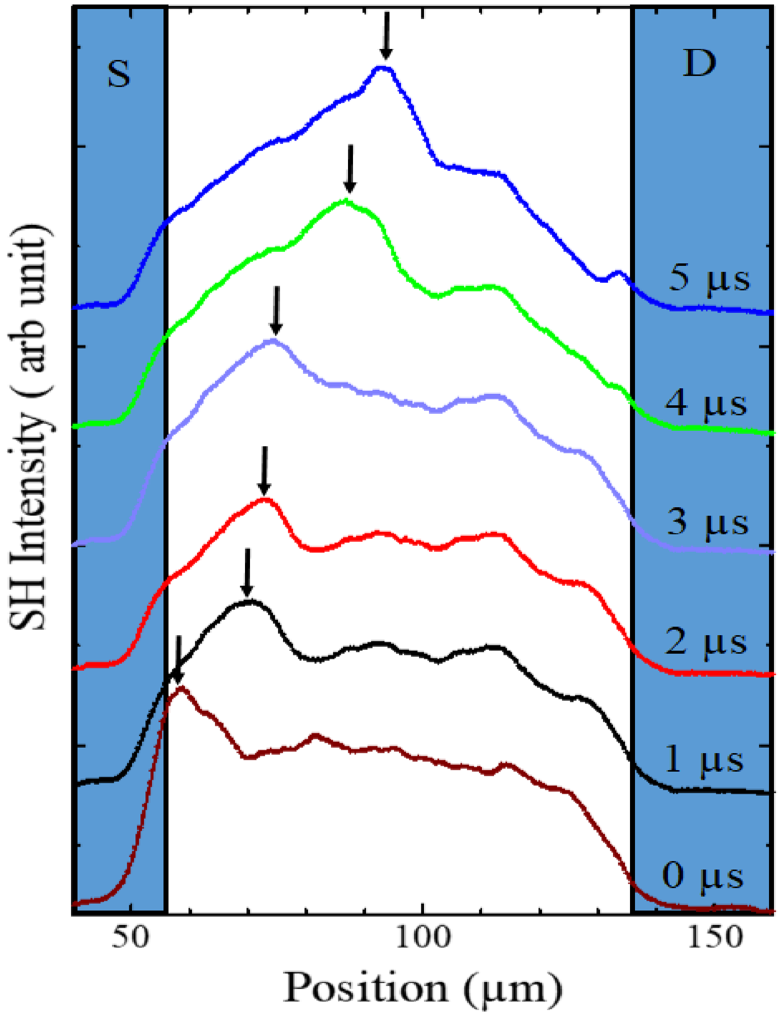

(b)

Figure 5.5: (a) Time-resolved SHG images from the channel of perovskite FET under the application of positive pulse to the source electrode. (b) SH intensity profile calculated from Fig. 5.5 (a) and arrows indicate the peak position.

Figure 5.5 (a) shows the time evolution of the TRM-SHG images in the channel region of perovskite FET at the delay times from 0 to 5 µs. For TRM-SHG measurement, FET transistor device with a channel length of 80 µm was used under positive pulse voltage application and the measurement was taken at room temperature. We could see the signal from whole area of the channel, due to strong fluorescence of perovskite as described before. However, the bright band of SHG signal moved from the source to the drain electrode under positive voltage application to the source electrode as shown in Fig. 5.5 (a). Fig. 5.5 (b) shows the transient SHG intensity distribution that was obtained from the SHG images by taking a line scan of the SHG image of Fig. 5.5 (a). At time 0 μs, the laser pulse coincided with the rising edge of the voltage pulse, and the SHG signals were found near the edge of the source electrode, indicating the electric field was formed around the source electrode. Interestingly, as clearly shown in the images, the emission band of SHG signal gradually moved in the channel from the source to the drain electrode. Motion of the emission band during applying positive voltage, which started from the source electrode, evidently indicated hole-injection from the Au source electrode. As we could directly visualize the hole transport in the channel, we analyzed the detail of carrier transport phenomena.

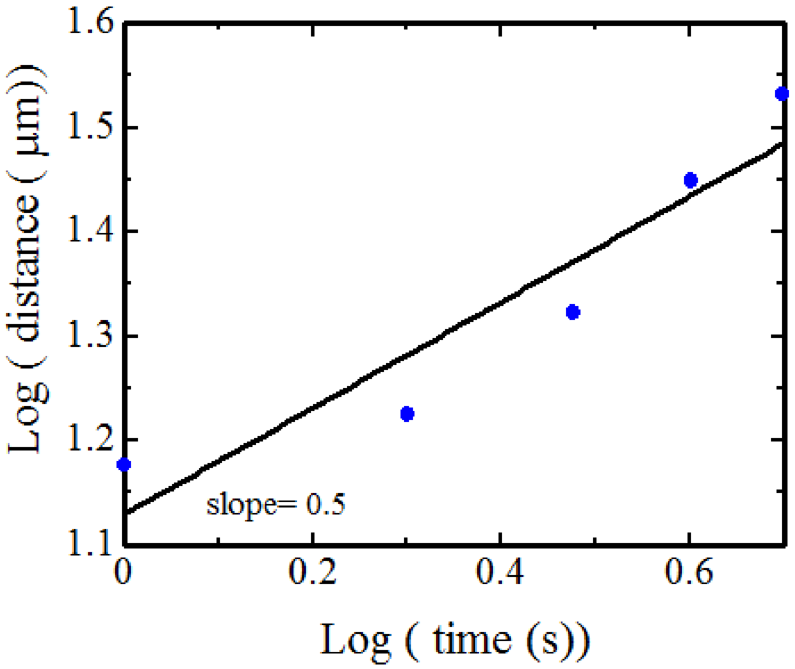

Figure 5.5: Log-Log plot for SHG peak position with respect to delay time t_d.

Figure 5.5 shows log-log plot of SHG peak position with respect to delay time t_d, and we could clearly see the square root dependence of the motion from the carrier transit time. This transient motion of SHG peaks well followed interface charge propagation model that was employed for analyzing transient carrier behaviors along the organic FET channel [7, 8].

5.2.4 Mobility calculation

Carrier mobility could be evaluated by analyzing the peak position of the SHG profile. Transient carrier mobility is expressed as,

$$\mu = \frac{x^2}{2Vt} \tag{5.1}$$

where V is the voltage applied to the source electrode with respect to the gate electrode and t is the time we observed the SHG peak at the position of x [9] as already explained in subsection 2.5.2.3. Eq. (5.1) suggests that the carrier migrates in the channel region on satisfying the square root time. The peak motion from the source to the drain electrode was due to migration of the electric field that originates from injected holes that were traveling along the channel in a diffusion-like manner [10, 11] as shown in Fig. 5.5 (a). This result indicated that the driving force of the carrier motion was the space charge field caused by the carriers injected from the source electrode themselves. By analyzing these images, the hole mobility could be calculated as 0.02 cm^2 / Vs, which was consistent with the hole mobility from PL quenching experiment even though which appeared to be lower as compared to other reports for this materials [12]. One of the reasons might be due to measuring in ambient temperature. It was known that the electric field screening due to ion migration in perovskite is dominant at room temperature [13, 14]. Such ion migration played a significant role to show low mobility in our devices. Even though, the mobility of TRM-SHG measurement is transient mobility and ion screening effect can be negligible, the insulator surface effect should be considered. Although the carrier mobility was still needed to capable of improvement to the photovoltaic applications, it was worth to discuss the validity of the novel method for visualization of carrier motion in perovskite film.

5.2.5 Evaluation of trapped charge density

It should be noted that the SHG intensity was concentrated in the front region of the propagating SHG profile as shown in Fig. 5.5 (b), and these SHG profiles helped us to make it more clear the presence of trap site in the channel region that strongly affected the transient carrier transport. By analyzing the EFISHG intensity, we could evaluate the electric field from Eq. (2.28), because it stated already that the intensity of SHG is directly proportional to the electric field and then based on the electric field the trap charge density could be estimated as follows.

At first, we subtracted fluorescent background by calculating the difference between two-photon-excited PL intensity ($V_g = 0$ V) from TRM-SHG images ($V_g \neq 0$ V). While injected holes were traveling along the channel, some of the holes were being trapped and these trapped holes also contributed to the formation of the space charge field along the channel [15]. Even though, the mobile charge and trapped charges were the same from electromagnetic viewpoint, we could carefully distinguish at the front peak of EFISHG profile.

If we considered firstly the gradual change of the mobile charge density (i.e., gradual channel approximation), almost homogeneous electric field in the direction from source to drain electrode was formed along the channel. For the case of trapped charges, it was reasonable to consider that the trapped charge distributes at the interface homogeneously, and these trapped charges induced a sharp peak at the edge of the carriers as shown in Fig. 5.6 (a). Meanwhile, according to the theoretical simulation of multiple-trapping and releasing (MTR) process, profiles of mobile charge field and trapped charge field were distinct at the front peak of SHG. If there were trapped charges, the profiles had obviously sharp peak at the front edge, whereas if there was no trapped charges, the homogeneous profile would be observed [15]. This implied that we could observe the superposition of two electric fields in the TRM-SHG measurement as shown in Fig. 5.6. (a).

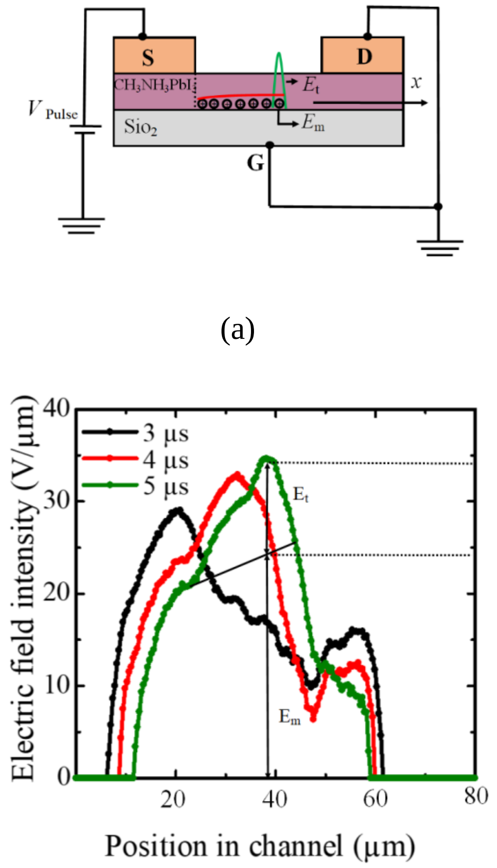

(a)

(b)

Figure 5.6: (a) Schematic diagram of the electric field formed by trapped charge and mobile charge in the device. (b) The electric field profile measured by TRM-SHG experiment from Fig. 5.5 (b). The solid line is the base line of the electric field contributed from the mobile and trapped charge at time 5 µs.

Fig. 5.6 (b) shows the electric field distribution at three different delay times calculated from TRM-SHG profiles shown in Fig. 5.5 (b). Based on theoretical and practical approach, we considered the SHG profile as a superposition of linearly increasing electric field E_m from mobile charge and peak-like electric field E_t from trapped charge. The linear fitting was extrapolated to the SHG peak position, and we determined E_m and E_t at the SHG peak position as shown in Fig. 5.6. (b). A linear slope was fitted to the SHG profile in the electric field position from 20 V/μm to 25 V/μm. And we discussed the density of trap charges by analyzing the electric field distribution around the sharp peak of TRM-SHG results as follows.

For the evaluation of trapped charge density, assuming the trapped charges at the interface between perovskite and insulator with two-dimensional densities N_trapped per unit area. Based on the base line of electric field of trapped charges and mobile charges, we directly estimated the ratio of trapped field and mobile field from the total electric field profile measured by TRM-SHG measurement by using the simple equation as follows.

$$N_\mathrm{trapped} = \frac{E_\mathrm{t}}{E_\mathrm{t}+E_\mathrm{m}} \varepsilon_0 \varepsilon_\mathrm{r} E_\mathrm{total} / q \tag{5.2}$$

where ε_0 and ε_r are permittivities of free space and the dielectric constant of perovskite materials respectively, and E_total is the electric field measured by the TRM-SHG. The density of trap charges could be estimated as 1.2×10^{13} /cm^2, and this value was reasonable value compared with the trap density of perovskite materials conducted in ambient laboratory atmosphere. [16] It was noteworthy that we assumed that electric field E_total was a sum of the two electric fields E_m and E_t.

5.2.6 Investigation of the behavior of trapped charge

We also focused on the discharge process to investigate the behavior of trapped charge directly. Here, SHG images were captured after turning off the voltage pulse with delay times from 30 to 70 μs. We found that the peak of the SHG profile could be still seen 70 μs after the applied voltage was removed and $V_g = 0$ V. The peak gradually decayed and moving towards slightly to opposite electrode after pulse voltage from 30 to 70 μs as shown in Fig. 5.7 (top). These EFISHG signals originated from the trapped charge, and then we can directly estimate the electric field intensity originating from the trapped charge.

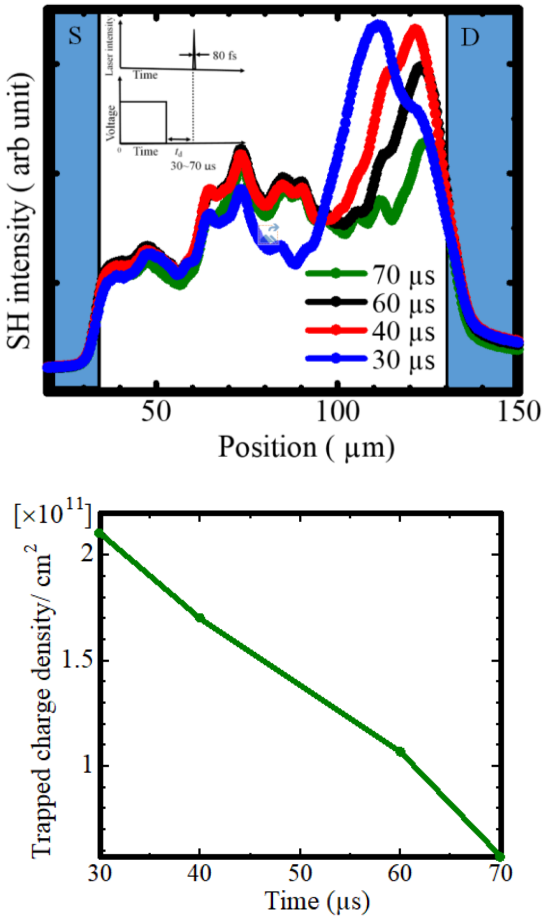

Figure 5.7: (top) SHG intensity profile for trapped charge after turning off the voltage pulse with delay times from 30 to 70 μs and inset is the timing chart for discharge process (bottom) The trapped charge density versus time.

As shown in Fig. 5.7 (top), we found that the trapped charge density gradually decreased after pulse voltage. In contrast to the charging process under voltage application from Fig. 5.7 (bottom), time constant for charge decay was very slow. This experimental result indicated that the peak-like structure in SHG image of the discharge process was originating from trapped charge, and we already confirmed the trapped charge field took over 70 μs to vanish. From this measurement, during discharge process, we could observe trapped charges for long time. Therefore, we concluded these long-lived trapped charged accumulated due to poor transport and low mobility. In addition, they could the possible source of hysteresis. Thus, we believed that TRM-SHG measurement would help to understand the optical and electrical properties of perovskite materials in more detail by visualizing the charge transport directly.

5.2.7 Carrier transport from counter electrode by applying negative pulse voltage

We conducted the TRM-SHG measurement under negative apply voltage also. Interestingly we could clearly see the SHG enhancement at negative pulse voltage. However, this enhancement was not from the source electrode as usual. Figure 5.8 (a) and (b) shows time-resolved SHG images from the channel of perovskite FET under the application of negative pulse to the source electrode. Thus, we had to find the origins of these SHG enhancements. Our assumption was as follows.

When the negative voltage was applied, the conductive layer from the source electrode was rapidly formed along the interface of channel by quick extraction of holes from negative electrode as in Fig. 5.9 (a). After that, due to potential difference between drain and interface layer, we saw additional holes could be injected from counter electrode as shown in Fig. 5.9 (b).

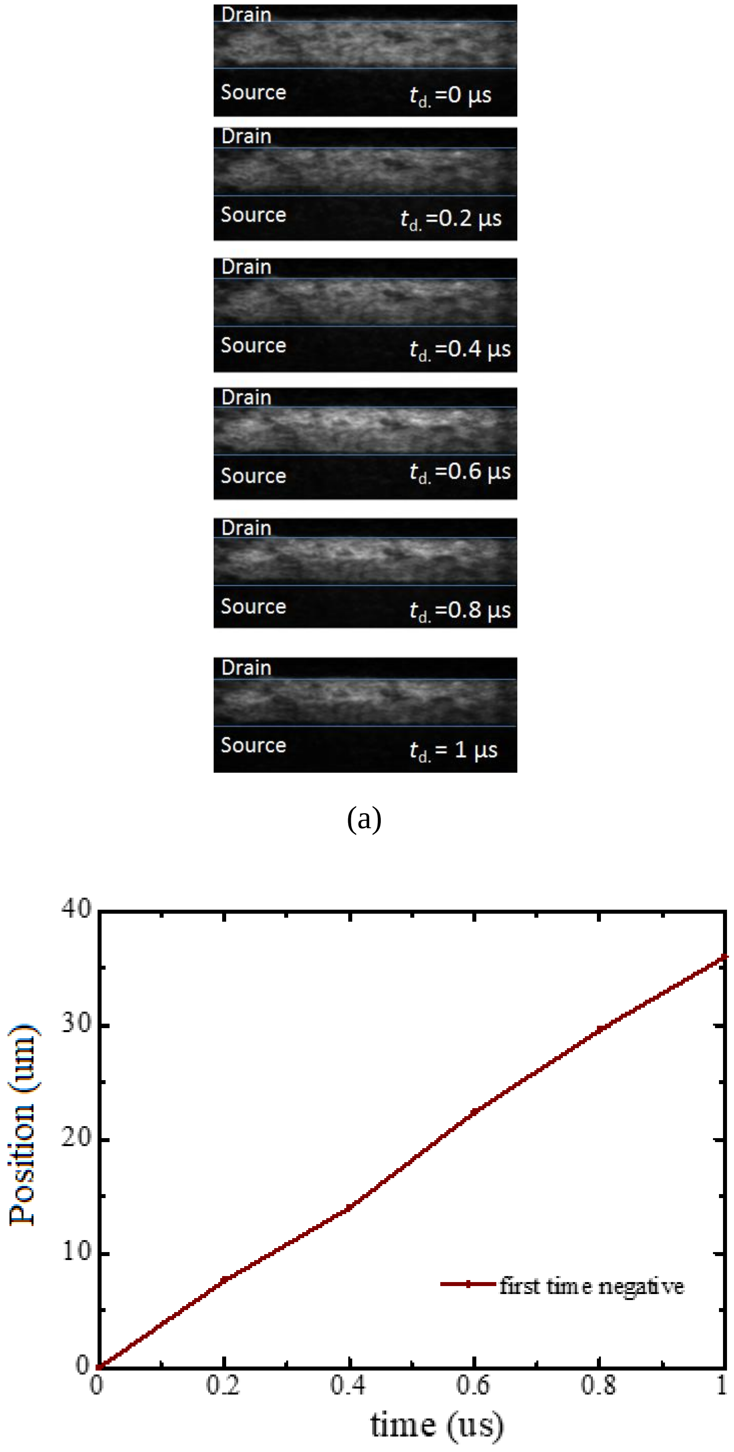

(a)

(b)

Figure 5.8: (a) Time-resolved SHG images from the channel of perovskite FET under the application of negative pulse to the source electrode. (b) The SHG peak position from counter electrode.

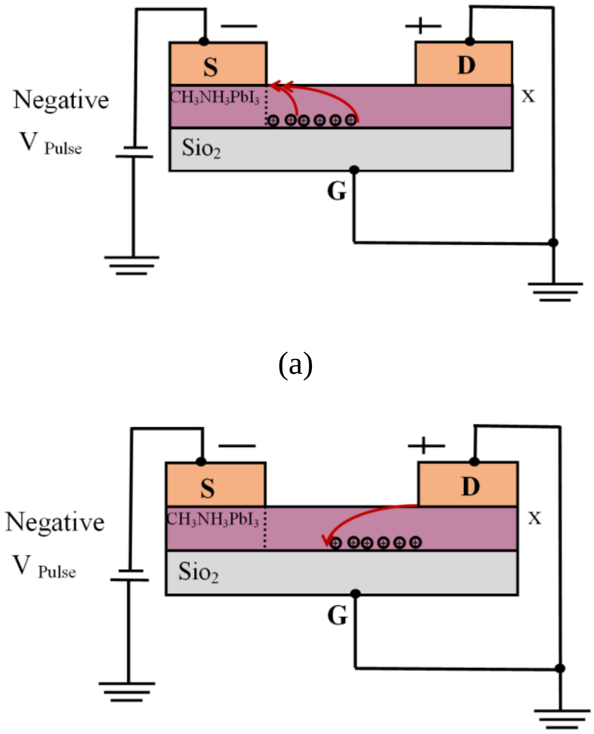

(a)

(b)

Figure 5.9: (a, b) Illustration of counter current under application of negative voltage.

For confirm the counter current under application of negative voltage, we measured the current from the counter electrode directly by using oscilloscope as shown in Fig. 5.10. Figure 5.10 shows the experimental setup and electrical connection for counter current measurement. For this measurement, negative voltage was applied from the source electrode and the drain current was recorded from oscilloscope simultaneously.

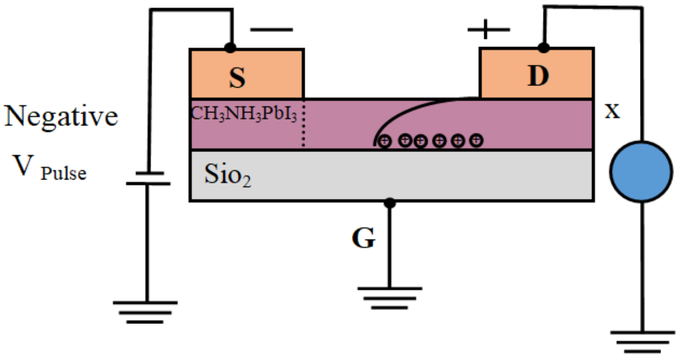

Figure 5.10: Measurement of counter current under application of negative current.

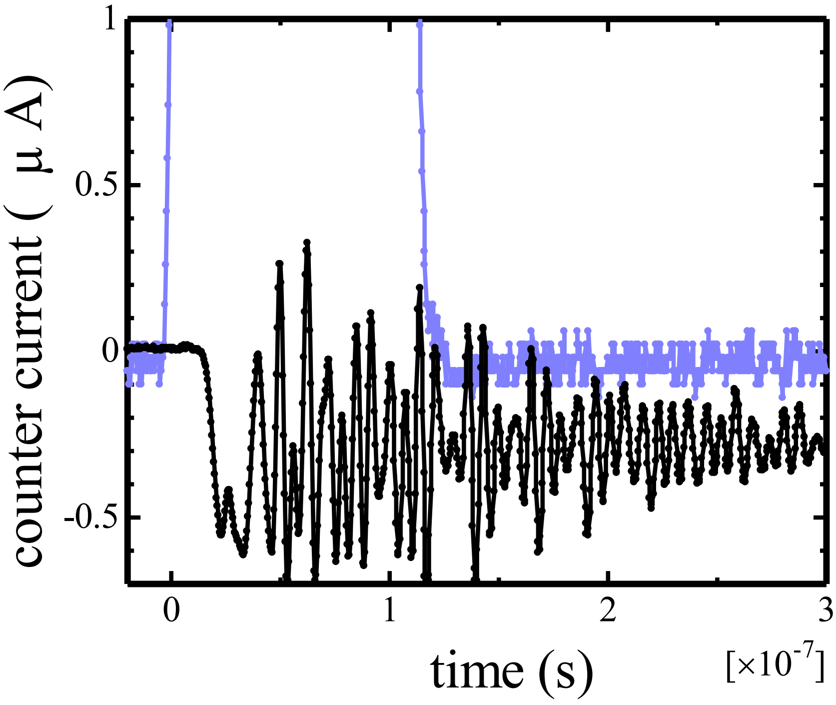

Figure 5.11: Counter current (violet line) and negative pulse voltage (black line).

Figure 5.11 shows counter current and negative pulse voltage recorded from the oscilloscope. According to the oscilloscope data, we could examine that as soon as the application of negative pulse from source, the current could flow from the counter electrode due to the rapidly formed along the interface of channel by quick extraction of holes from negative electrode. Thus, we confirmed our assumption described above could be utilized for the above measurement perovskite material.

Indeed, intensity of EFISHG signal is directly proportional to the square of the local electric field as expressed in Eq. (2.28) it can be used to analyze both of charges (holes and electrons) inside the materials. But here, we emphasized the visualization of holes based on TRM-SHG method and we successfully visualized the hole injection from the electrode to the channel region. If electron can inject from the electrode and transport through the channel of the perovskite, it is also possible to estimate the electron mobility by TRM-SHG. However, until now electron transport in perovskite materials was still not clear. Another notice was that the devices often proned to degradation during operation over multiple cycles. We still needed to understand more for the instabilities in the device characteristics.

5.3 Conclusions

The visualization of the carrier behavior of organic inorganic hybrid perovskites, which demonstrate excellent photovoltaic performance in solar cells helps to understand their fundamental transport properties. In this chapter, we investigated the complex carrier behavior of $CH_3NH_3PbI_3$ by using unique technique EFISHG.

Based on the transient electric field migration directly probed by the time-resolved microscopic optical second-harmonic generation (TRM-SHG) technique, we successfully detected the transient hole transport in the perovskite for the first time. From the spectroscopic point of view, SHG signal resonantly enhanced at the fundamental wavelength of around 1560 nm through the band-transition under the voltage application. Square dependence of the SH intensity on the applied voltage at the wavelength of 1560 nm clearly indicated the electric field induced process of the

SHG. We could visualize the carrier motion in the channel of perovskite (FET) with this fundamental wavelength. Carrier mobility was estimated as 0.02 cm^2/Vs by analyzing the transient carrier motion. TRM-SHG technique was also employed to investigate the effect of traps on the transient carrier motion. Based on the peak of the transient electric field distribution, trap density, and dynamic carrier mobility were separately estimated. TRM-SHG would be also useful in exploring trap affecting on the carrier dynamics in perovskite materials. The trapped charge density could be estimated as 1.2×10^{13} /cm^2 and we confirmed the trapped charge density gradually decreases in discharging process. This directly visualization of carrier behavior for organic inorganic hybrid perovskites which demonstrate excellent photovoltaic performance helps to understand their fundamental transport properties.

Bibliography

[1] T. Manaka, E. Lim, R. Tamura, and M. Iwamoto, "Direct imaging of carrier motion in organic transistors by optical second-harmonic generation," Nat. Photon. 1, 581-584, 2007.

[2] T. Manaka and M. Iwamoto, "Optical second-harmonic generation measurement for probing organic device operation," Light Sci. Appl. 5 (3) 16040, 2016.

[3] T. Manaka, E. Lim, R. Tamura, and M. Iwamoto, "Modulation in optical second harmonic generation signal from channel of pentacene field effect transistors during device operation," Appl. Phys. Lett. 87 (22) 222107, 2005.

[4] T. Manaka, E. Lim, R. Tamura, D. Yamada, M. Iwamoto, "Probing of the electric field distribution in organic field effect transistor channel by microscopic second-harmonic generation," Appl. Phys. Lett. 89 (7) 072113, 2006.

[5] G. Horowitz, M. E. Hajlaoui, and R. Hajlaoui, "Temperature and gate voltage dependence of hole mobility in polycrystalline oligothiophene thin film transistors," J. Appl. Phys. 87 (9) 4456-4463, 2000.

[6] G. Gu, M. G. Kane, J. E. Doty, and A. H. Firester, "Electron traps and hysteresis in pentacene-based organic thin-film transistors," Appl. Phys. Lett. 87 (24) 243512, 2005.

[7] M. Weis, J. Lin, D. Taguchi, T. Manaka, and M. Iwamoto, "The charge transport in organic field-effect transistor as an interface charge propagation: The Maxwell–Wagner effect model and transmission line approximation," Jpn. J. Appl. Phys. 49 071603, 2010.

[8] Y. Ohshima, E. Lim, T. Manaka, M. Iwamoto, and H. Sirringhaus, “Observation of electron behavior in ambipolar polymer-based light-emitting transistor by optical second harmonic generation,” J. Appl. Phys. 110 (1) 013715, 2011.

[9] E. L. Unger, E. T. Hoke, C. D. Bailie, W. H. Nguyen, A. R. Bowring, T. Heumüller, M. G. Christoforo, and M. D. McGehee, “Hysteresis and transient behavior in current–voltage measurements of hybrid-perovskite absorber solar cells,” Energy Environ. Sci. 7 3690-3698, 2014.

[10] T. Manaka, F. Liu, M. Weis, and M. Iwamoto, “Diffusion like electric-field migration in the channel of organic field-effect transistors,” Phys. Rev. B. 78 (12) 121302, 2008.

[11] T. Manaka, F. Liu, M. Weis, and M. Iwamoto, “Mobility measurement based on visualized electric field migration in organic field-effect transistors,” Appl. Phys. Express 2 (6) 06150, 2009.

[12] D. B. Mitzi, C. D. Dimitrakopoulos, J. Rosner, D. R. Medeiros, Z. Xu, C. Noyan, “Hybrid field-effect transistor based on a low-temperature melt-processed channel layer,” Adv. Mater. 14 (23) 1772-1776, 2002.

[13] J. H. Heo , S. H. Im, J. H. Noh, T. N. Mandal, C. S. Lim, J. A. Chang, Y. H. Lee, H. J. Kim, A. Sarkar, M. K. Nazeeruddin, M. Gratzel, S. II. Seok, “Efficient inorganic–organic hybrid heterojunction solar cells containing perovskite compound and polymeric hole conductors,” Nat. Photon. 7 (6) 486, 2013.

[14] X.Y. Chin, D. Cortecchia, J. Yin, A. Bruno, and C. Soci, “Lead iodide perovskite light-emitting field- effect transistor,” Nat. commun. 6 7383, 2015.

[15] T. Manaka, F. Liu, M. Weis, and M. Iwamoto, “Influence of traps on transient electric field and mobility evaluation in organic field-effect transistors,” J. Appl. Phys. 107, 043712. 2010.

[16] D. Prochowicz, P. Yadav, M. Saliba, S. M. Zakeeruddin, J. Lewiński, and M. Grätzel, “Reduction in the interfacial trap density of mechanochemically synthesized MAPbI3,” ACS Appl. Mater. Interfaces 9, 34, 28418-28425, 2017.

Chapter 6

Conclusions and Future Prospects

6.1 Conclusions

The visualization for the carrier behavior of organic-inorganic hybrid perovskites, which demonstrate excellent photovoltaic performance in solar cells helps to understand their fundamental transport properties. The aim of study concerns about the study of the carrier behavior such as charge injection and transport properties of organic-inorganic hybrid perovskite materials by using spectroscopic methods. The main proposed methods are electrical and optical measurements such as PL and EFISHG to directly visualize the carrier transport properties which make it possible to probe the carrier behaviors in materials. In the followings, firstly I will summarize each chapter and then proceed to the general conclusions and future prospects.

In chapter 1, I summarized not only the backgrounds and literature reviews but also challenges of perovskite materials based on the photovoltaic world to clarify the purpose of the study. For perovskite materials, despite the rapid development in power conversion efficiency of the photovoltaic cells, there is a big gap to understand the unclear behavior such as carrier injection and transport process. Based on these facts, our motivations and structure of the dissertations were presented.

In chapter 2, the experimental methods and background theory used in the present study were briefly explained. Firstly, the simple electrical FET measurement was used to observe the steady-state electrical characteristics. Consequently, lateral

TOF method was conducted to evaluate the transient characteristics and lateral transport mechanism. For charge carrier transport properties, charge propagation model and interface charge propagation model were briefly described. Then PL imaging and TRM-SHG techniques were proposed to direct visualization of carrier behavior of the perovskite materials.

As described above, we focused on the electrical characteristics and behaviors of perovskites for steady-state and transient state in chapter 3. Firstly, we couldn't see the modulated drain current at room temperature for SiO_2 based perovskite FETs, due to overwhelm of screening of gate field for the accumulation of migrated ion. When the temperature was decreased from 198 K to 77 K, we could see ambipolar characteristics with significant hysteresis due to the freezing the ion migration. Then we calculated the electron and hole mobility from the transfer characteristics curve. Moreover, the hysteresis at low temperatures revealed that there was some unclear behavior rather than ion migration. The possible origin was probably due to gate insulator effects and traps.

From TOF measurement, the lateral transport current was dispersive and no plateau region that probably due to multiple trapping in the fabricated film. For dispersive carrier transport, the transit time couldn't determine directly. We estimated the hole and electron transit time and carrier mobility based on Scher-Montroll theory. And also for the diffusion behavior could be seen at low electric field region under 100 V and drift behavior could be confirmed at higher electric field region. Therefore, many aspects of the charge transport, such as the mechanism of carrier scattering and trapping, the role of ion screening, and the origin of unusual behaviors (hysteresis) could be explained by steady state FET measurement and lateral TOF measurement.

In chapter 4 we conducted the transient PL imaging to discuss the transient carrier behavior. PL imagining technique provides direct insight into the nature of charge carriers such as mobility, ion migration, and surface defects. Before PL measurement, we confirmed the charge is a source of PL mechanism and after that, we observed the fast response of PL quenching process. Under detail analyses of the time-dependent fluorescent images, we could clearly notice the two-step changing of PL; firstly PL enhancement might due to the high carrier transport phenomena then gradually decreasing of PL intensity showed the migration of intrinsic ions in the perovskite thin film. By combining the lateral TOF method, we confirmed that this transient PL enhancement corresponds to the carrier motion and transit time could be directly evaluated. After that we successfully observe the carrier mobility by direct visualization of PL experiment. The results of visualization of PL highlighted the valuable carrier information such as charge quickly diffuse through the film due to the high mobility, long diffusion length, ambipolar carrier behavior. Finally, important facts were intrinsic ions were spreading throughout the film.

In chapter 5, we had successfully probed the carrier distribution in perovskite thin film based on the TRM-SHG technique for the first time. Firstly we confirmed the electric field induced SHG signal by voltage dependence SHG signal. Because perovskite is fluorescence materials itself, and spectral overlap of PL and SHG is a serious issue for detecting of SHG signal for those type of materials. Then we could directly visualization the transient hole transport in the FET channel of the $CH_3NH_3PbI_3$ film based on the transient electric field migration by TRM-SHG technique. By analyzing the electric field distribution based on SHG profile, TRM-SHG mobility reflected the local environment during the carrier transport and was evaluated as 0.02 cm^2 / Vs. The carrier mobility of PL and EFISHG were matching each other. Besides, the condition of trapped charges could be investigated from the transient carrier motion of TRM-SHG signal. We have also confirmed these trapped charges were long-lived and gradually decreased after applying voltage. Thus, they could be the possible source of poor transport, low mobility, and source of hysteresis for perovskite materials.

As summarized above, based on conventional FET measurement the steady state carrier mobility was the lowest compared with other techniques due to screening effect at room temperature. Moreover, from the TOF measurement, trapping and scattering caused dispersive transient current and some unclear behaviors. However, two step changing PL direct visualization revealed that there was intrinsic ion spreading throughout the film and such intrinsic ions affects the IV hysteresis and low mobility. On the other hand, TRM-SHG measurements provided more direct evidence for the trapped charged condition. These traps and ions caused a significant impact on the unclear behavior of the perovskite film. Therefore, the new points of the study are the direct visualization technique of carrier behaviors such as PL and TRM-SHG were applied to perovskite materials for the first time. Accordingly, the analysis of carrier behaviors by TRMSHG and PL measurements would unambiguously clarify the nature of charge transport in this class of materials and will promote the development of complementary optoelectronic applications.

6.2 Future works

6.2.1 Concerning ion migration

In here we proposed the carrier and ion motion by PL visualization. Indeed, discriminate evaluation of the carrier and ion current was quite important to discuss the fundamental electrical transport properties of perovskite materials and which must be further discussed in future works.

6.2.2 Concerning trapping

Further identification of the prevalence and impact of trap states during operation will be essential for improving the device performance. Here for the time limit, we left the temperature dependence experiments for trapped charge. The trap effecting can be further investigated by changing the temperature. For a deep understanding of the carrier behavior, the temperature dependence is crucial, which can be done in future work.

6.2.3 Concerning the carrier mobility

We have noticed that mobilities obtained from electrical methods and optical methods have some discrepancies. This is likely due to the experiment and measurement condition. Improvement of experiments and more data analysis for modeling of the transport charges to be addressed for the future work.

6.2.4 Concerning the degradation

During operation over multiple cycles, the devices could be degradation that would confuse the operation mechanism and we still needed to understand more for these instabilities in device characteristics.

6.3 Prospects

Our findings offered significant fundamental insight on optical and charge transport properties of perovskite materials. Here, the carrier behavior of electrical and optical characteristics was carefully studied and explained for each technique. Even though this work only used FET structure as an experimental tool to investigate the fundamental transport phenomena, the ideas can also be extended to all perovskite optoelectronics devices such as photovoltaic solar cells, LEDs, Laser, and so on.

In addition, we adopted TRMSHG and PL to directly prove the carrier behaviors for perovskite materials, which can offer clear evidence for the carrier behavior. Although the present studies could not give yet the accurate answers for unclear behaviors such as traps or ions, the visualization of carrier behavior can be readily extended for the areas concerning the characterization of carrier behaviors of other perovskite materials. Therefore, our future prospect is to approach for the developments of the perovskite world based on the EFISHG and PL techniques.

Acknowledgements

First of all, I would like to express my deepest gratitude to my supervisor, Prof. Takaaki Manaka, for his excellent guidance, encouragement, and invaluable discussions during this doctoral course.

Special appreciation is extended to Prof. Mitsumasa Iwamoto for giving me the initial chance to get this scholarship and encouragement throughout my study.

I would like to acknowledge Prof. Takaaki Manaka, Prof. Shigeki Nakagawa, Prof. Akira Yamada, Prof. Shinsuke Miyajima, Prof. Hiroaki Iino, and Prof. Shyam Sudhir Pandey for their invaluable comments and advices in thesis presentation as board of examiners.

I would like to express my gratitude to Dr. Dai Taguchi for supporting me from experiments to writing research manuscripts and sharing experience. It is helpful to progress smoothly for my study.

I would also like to extend my thanks to all former and current members of Manaka laboratory, for their help, kind assistance and teaching me how to use lab equipments. It is a pleasure also to share many events with them.

A special thanks to Ms. Kazuko Ishimaru for her help in many administrative issues. I would like to express my appreciation to each respective person from Ministry of Education and principal of Technological University (Hinthada) for giving permission to study for three years and three months and all of my colleagues for their understanding and encouragement.

Especially, I would like to express my acknowledgement to AUN / SEED Net program, JICA for their financial supports.

In addition, many thanks to my beloved parents and brothers for their understanding and encouragement to attain my attention throughout my study.

Finally, I would like to thank to each everyone who helped me directly or indirectly towards the successful completion of this research.

List of Publications and conference presentations

Lists of publication

1) Lei Lei Yin Win, Dai Taguchi, Takaaki Manaka, “Direct Observation of Carrier Transport in Organic- Inorganic Hybrid Perovskite Thin Film by Transient Photoluminescence Imaging Measurement”, Japanese Journal of Applied Physics, 58, SBBG18, 2019.
2) Lei Lei Yin Win, Dai Taguchi, Takaaki Manaka, “Transient Carrier Visualizations of Organic-Inorganic Hybrid Perovskite Thin Film by using Time-Resolved Microscopic Second- Harmonic Generation (TRM-SHG)”, Organic Electronics 75, 105416, 2019.

Conference Papers

1) Lei Lei Yin Win, Takaaki Manaka, “Study of Carrier Behavior in Organic–Inorganic Hybrid Perovskite Materials”, 9th Multidisciplinary International Student Workshop (MISW 2017), Oral, Tokyo (Japan), August 2017.
2) Lei Lei Yin Win, Takaaki Manaka, Mitsumasa Iwamoto, “Study of Carrier Behavior in Organic–Inorganic Hybrid Perovskite Materials”, 17th International Discussion & Conference on Nano Interface Controlld electronic Devices (IDC-NICE 2017), Poster, Niigata (Japan), October 2017.
3) Lei Lei Yin Win, Takaaki Manaka, Mitsumasa Iwamoto, “Study of Carrier Behavior in Organic–Inorganic Hybrid Perovskite Materials by using Optical

Spectroscopic Method", The Interdisciplinary Research and Global Outlook Conference (IRAGO 2017), Oral, Tokyo (Japan), November 2017.

4) Lei Lei Yin Win, Dai Taguchi, Takaaki Manaka, Mitsumasa Iwamoto, "Visualization of Carrier Transport in Organic-Inorganic Hybrid Perovskite Thin Film by Photoluminescence Decay Method", 2018 International Conference on Solid State Devices and Materials (SSDM 2018), Oral, Tokyo (Japan), September 2018.

5) Lei Lei Yin Win, Dai Taguchi, Takaaki Manaka, "Visualization of Carrier Transport in Organic-Inorganic Perovskite Field-Effect Transistor by Electric-Field-Induced Optical Second-Harmonic Generation (EFISHG)", Compound Semiconductor Week 2019 (CSW 2019), Oral, Nara (Japan), May 2019.